NUCLEAR STRUCTURE AND ASTROPHYSICS OF ^{23}Mg WITH THE NEW DSL2 SETUP

By

Lexanne Weghorn

A DISSERTATION

Submitted to
Michigan State University
in partial fulfillment of the requirements
for the degree of

Physics—Doctor of Philosophy

2026

ABSTRACT

The beta decay of radionuclide ^{22}Na is characterized by a half-life of 2.6 years and the subsequent emission of a 1275 keV gamma ray. ^{22}Na is thought to be produced in ONe classical novae, and the characteristic 1275 keV gamma ray is a long-sought target for detection by observational astronomy missions probing the sites of active nucleosynthesis, including the COSI mission set to launch in 2027. Accurate models of the production and destruction of ^{22}Na in novae are sought to estimate the sensitivity required by future space-based missions in order to detect the 1275 keV gamma ray, and to compare models to observation should future missions detect this gamma ray.

The reaction and decay rates governing the production of ^{22}Na during the thermonuclear runaway of a nova are well known, and it is also known that the destruction of ^{22}Na in these conditions is driven by proton capture to ^{23}Mg. The thermonuclear rate of this proton capture reaction is dominated by a single narrow resonance corresponding to a proton energy of 213 keV and the excited state in ^{23}Mg around 7784 keV. Direct measurements of the strength of this resonance are discrepant, and indirect measurements using the spin and lifetime of the key excited state in ^{23}Mg and the proton branching ratio are further discrepant from the direct measurements. There are standing questions about the spin, lifetime, and excitation energy of the state of astrophysical interest that affect resonance strength calculations.

In the present work, the Doppler Shift Lifetimes (DSL) setup at the TRIUMF-ISAC II facility was upgraded to DSL2 in a collaboration between FRIB and TRIUMF and successfully commissioned in an experiment measuring the lifetimes of excited states in ^{23}Mg. DSL utilizes a ΔE-E Si detector telescope. In the upgrade from DSL1 to DSL2, the active area of the Si detectors was increased from 150 mm^2 to 2450 mm^2, and the ΔE detector was upgraded from a single channel detector to a Si strip detector with 16×16 overlapping strips. This results in around an order of magnitude improvement in the sensitivity of the setup due to greater angular acceptance and ability to account for kinematic broadening.

Recently developed Markov chain Monte Carlo-based Bayesian analytical techniques were applied to the Doppler shift attenuation method lineshape analysis to determine lifetimes. Two

spin and parity cases were investigated for the state of astrophysical interest, and despite low beam intensities during–and an early end to–the experiment, upper limits were set on the lifetime of the state for both cases. These upper limits are presented here, as well as a resolution to an asymmetry in the literature half-lives of the 2nd and 6th excited states of ^{23}Mg and its mirror nucleus ^{23}Na. It would be worth re-running this experiment with a sufficiently intense ^{24}Mg beam to increase statistics by at least an order of magnitude. A future experiment using the DSL2 setup to measure the lifetime in ^{31}S that constrains the ^{30}P$(p,\gamma)^{31}$S reaction rate has been approved to run at TRIUMF. The analytical tools developed and refined for this analysis will be applied to that experiment.

ACKNOWLEDGEMENTS

TABLE OF CONTENTS

LIST OF TABLES

LIST OF FIGURES

CHAPTER 1

INTRODUCTION

1.1 Nuclear Astrophysics

Everything we know has its origins somewhere in outer space. At the very beginning, in the first seconds after the Big Bang—some 13.8 billion years ago—the first protons and neutrons were born. The first minutes of our universe saw the formation of atomic nuclei, in a process known as Big Bang nucleosynthesis, where the majority of the early neutrons were bundled up into tightly-bound ^{4}He nuclei, also known as alpha particles. In addition to alpha particles, hydrogen in the form of ^{2}H and ^{3}H; ^{3}He; ^{7}Li; and ^{7}Be were formed. The vast majority of nuclei produced are either hydrogen or helium, with only trace amounts of lithium and beryllium produced [1].

It wasn't until around 380,000 years later that the young universe cooled to a point that the atomic nuclei produced during Big Bang nucleosynthesis were able to capture electrons and form neutral atoms [2]. After the formation of this primordial cosmic sea consisting mainly of hydrogen and helium atoms, the universe spent several million years in the dark.

Finally, around 100-200 million years after the Big Bang, the first stars began to light up the space around them. Denser regions of hydrogen and helium gas, initially drawn together in denser regions of dark matter, grew even more dense as gravity pulled in more material. These clouds of gas eventually became dense enough that they collapsed in on themselves, forming hot cores at their centers. Eventually, the contraction allowed hydrogen fusion to begin, and the new stars began converting hydrogen to helium through a series of nuclear reactions known as proton-proton chains, or pp chains.

The first stars by and large only had hydrogen and helium to burn. This resulted in stars that were most likely much larger and shorter-lived than our sun [3], though we have yet to observe stars as metal-poor as these first stars would have been [4]. Once much of the hydrogen in the cores of these stars had been consumed, they would begin helium burning, finally starting to produce heavier elements like carbon and oxygen. The death of these early stars scattered metals into the interstellar medium and allowed for a second generation of stars to be born, though these stars were

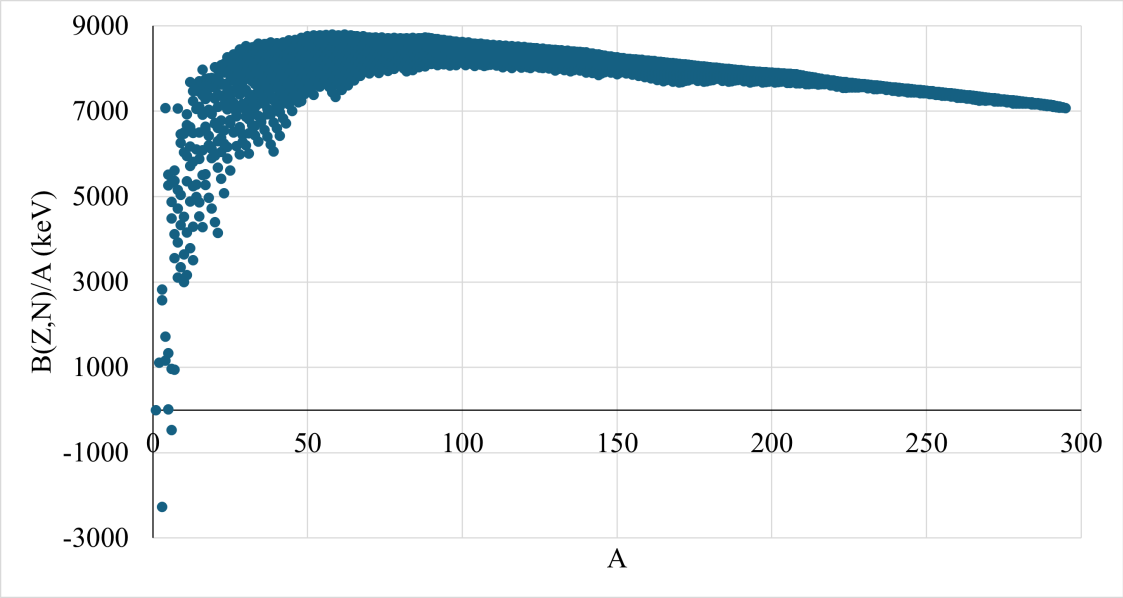

Figure 1.1 Binding energy per nucleon plotted against total number of nucleons (A) [5].

still relatively metal-poor as compared to the youngest generation of stars like our sun.

Stars are able to synthesize elements up to the iron region, given that the star is massive enough. The highest binding energies per nucleon are seen in ^{56}Fe, ^{58}Fe, and ^{62}Ni. Figure 1.1 shows the binding energies per nucleon, where the maximum in the A = 56 region is clear. Of these three isotopes with the highest binding energies, the reactions that produce ^{56}Fe are favored in stellar nucleosynthesis. ^{58}Fe and ^{62}Ni are instead produced through other processes. Anything heavier is energetically unfavorable to produce, and requires extreme conditions to form.

Although charged particle fusion is impeded by the high Coulomb barrier, heavier nuclei can be formed through several processes, including a series of neutron captures and β^- decays to form neutron-rich isotopes, or a mechanism known as the p-process to produce proton-rich isotopes. The neutron capture processes are dominated by the rapid neutron capture process, or the r-process; and the slow neutron capture process, which is also referred to as the s-process. The s-process proceeds through isotopes much closer to stability than the r-process due to the speed of the neutron capture being slow compared to the rates of the β^- decays.

There are several sites of nucleosynthesis beyond the cores of stars, including stellar novae, and extremely energetic events such as supernovae and neutron star mergers. Each produces a

unique distribution of isotopes, depending on the energy of the event and the composition of the objects involved. As observations of energetic astrophysical events provide more astronomical data including isotopic signatures from different types of events, models of nucleosynthesis can be improved. Laboratory experiments probing nuclear reactions that dominate different nucleosynthesis chains or determine which isotopes are more likely to be produced given certain conditions can also be done. The information gained through these experiments can inform observational missions and be compared to observational data as it becomes available. Theoretical nuclear physics and computational physics are important for astrophysical modeling, and information determined in laboratory experiments can be used to refine these models.

1.2 Classical Novae

Novae are sites of interest in the field of nuclear astrophysics. Novae are among the most frequent stellar explosions, estimated to occur in out galaxy with a frequency of approximately 20-70 per year [6]. This far exceeds the estimated galactic supernova rate of approximately 3 per century [7]. The energy and composition of a nova lend themselves to nucleosynthesis, and the higher rate of nova occurrence provides more opportunities for them to be observed. Observational data on novae is abundant, and observations have been made in all major wavelength bands of the electromagnetic spectrum.

Novae are the end of the life cycle for mid-sized stars in a close binary system with a surviving companion star. The dying star has burned all of the elemental fuel it is able to and now exists as a white dwarf. It and its extant companion star orbit around a common center of mass. The companion star still has a hydrogen-rich outer shell that the white dwarf is able to siphon material from. White dwarfs are incredibly dense, fitting masses similar to that of the Sun into radii on par with that of the earth, or about 10^6 grams of material per cubic centimeter [8]. They are comprised of electron-degenerate matter, and the size of the white dwarf's progenitor determines its elemental composition. Less massive stars like our Sun, with masses in the approximate range of 0.4-9 $M_\odot$, will end their life cycles as white dwarfs comprised mostly of carbon and oxygen known as CO white dwarfs. Heavier stars in the mass range of approximately 9-11 $M_\odot$ will result in oxygen-neon,

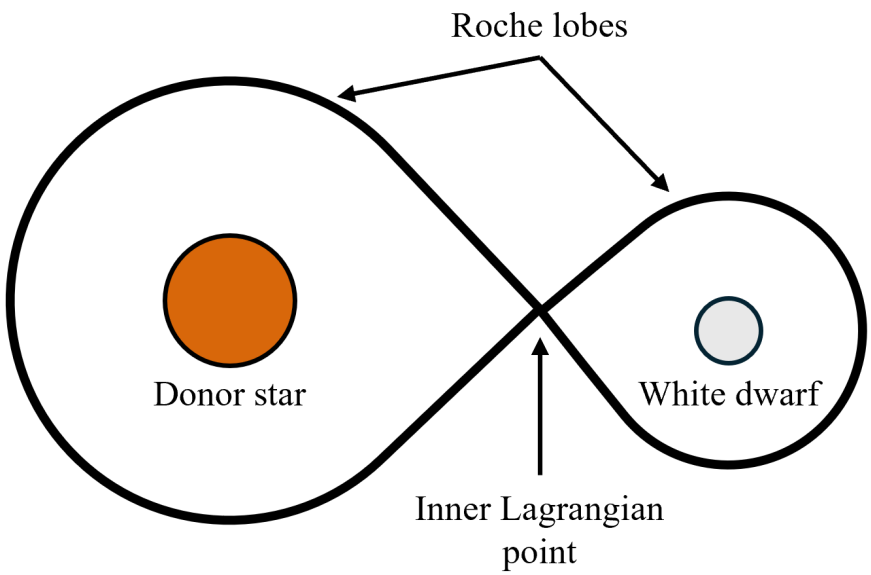

Figure 1.2 Schematic of the Roche lobes and inner Lagrangian point of a white dwarf and its companion star (not to scale).

or ONe white dwarfs [1].

Each star in the binary has its own region in which material is considered gravitationally bound to it, which is known as a Roche lobe. The point where the two Roche lobes of the stellar binary touch is known as the inner Lagrangian point. This is where the gravitational potential of the two stars is equal. When the hydrogen-rich envelope of the larger star is large enough to overflow from its Roche lobe, material transfers to an accretion disk around the surface of the white dwarf through the inner Lagrangian point. Figure 1.2 shows a basic diagram of a binary system consisting of a white dwarf and its companion star. Some of the material does fall to the surface of the white dwarf, where the gravity of the white dwarf heats and compresses the material. Eventually, the innermost layer of accreted material becomes electron degenerate, and the heat allows the pp chains to begin fusing hydrogen to helium.

Gradually, the temperature increases, and the degeneracy prevents the shell from expanding and cooling. Eventually the temperature becomes high enough to cause a thermonuclear runaway near the surface of the white dwarf. This thermonuclear runaway is a cycle of nuclear reactions heating the material, leading to faster reactions, leading to further heating of the material. This occurs until

the degeneracy is lifted, re-coupling temperature and pressure, causing a nova explosion [1].

Classical novae occur over the course of a few hours, but are thought to only recur on the order of every 10,000 to 100,000 years. The temperature of a nova peaks around 0.1-0.4 GK [9]. They eject around 10^{-5}-$10^{-4} M_{\odot}$ of material, and studying the abundances of different elements in the material ejected provides information about the thermonuclear runaway and the composition of the white dwarf [10].

1.3 Nova Production of ^{22}Na

ONe white dwarfs are made mostly of ^{16}O and ^{20}Ne. Therefore, these isotopes are key participants in various channels of nova nucleosynthesis in an ONe type nova.

Large amounts of ^{22}Na are thought to be produced over the course of an ONe nova. Reactions proceeding off of ^{20}Ne in nova conditions tend to pass through ^{22}Na, though the amount of ^{22}Na ejected from a nova depends on factors such as the temperature and composition of the nova, as well as the rates of the reactions involved. The nova hydrogen burning proceeds through a series of reactions involving Ne and Na isotopes known as the NeNa cycle. Figure 1.3 illustrates the key isotopes and reactions involved in the NeNa cycle.

During accretion, the production of ^{22}Na proceeds through the chain of reactions starting with a proton capture on ^{20}Ne, notated as $^{20}\mathrm{Ne}(p,\gamma)^{21}\mathrm{Na}(\beta^{+})^{21}\mathrm{Ne}(p,\gamma)^{22}\mathrm{Na}$. Temperatures have not increased very much by this point, so this is referred to as the cold mode of the NeNa cycle. The production of ^{22}Na can also proceed through proton capture on ^{21}Na instead of β^{+} decay, in the chain of reactions $^{20}\mathrm{Ne}(p,\gamma)^{21}\mathrm{Na}(p,\gamma)^{22}\mathrm{Mg}(\beta^{+})^{22}\mathrm{Na}$. The ^{22}Na mainly decays via β^{+} decay to ^{22}Ne, which then proton captures to ^{23}Na [14].

As the temperature increases, the $^{21}\mathrm{Ne}(p,\gamma)^{22}\mathrm{Na}$ reaction outpaces the β^{+} decay of ^{21}Na, depleting the amount of ^{21}Ne available. This in turn limits the amount of ^{22}Na produced. When the nova has reached peak temperatures, the main channel through which ^{22}Na is destroyed is $^{22}\mathrm{Na}(p,\gamma)^{23}\mathrm{Mg}$.

After the nova, the remaining ^{22}Na, which has a half-live of about 2.6 years, will β^{+} decay to the short-lived first excited state in ^{22}Ne. When the ^{22}Ne de-excites to the ground state it releases a

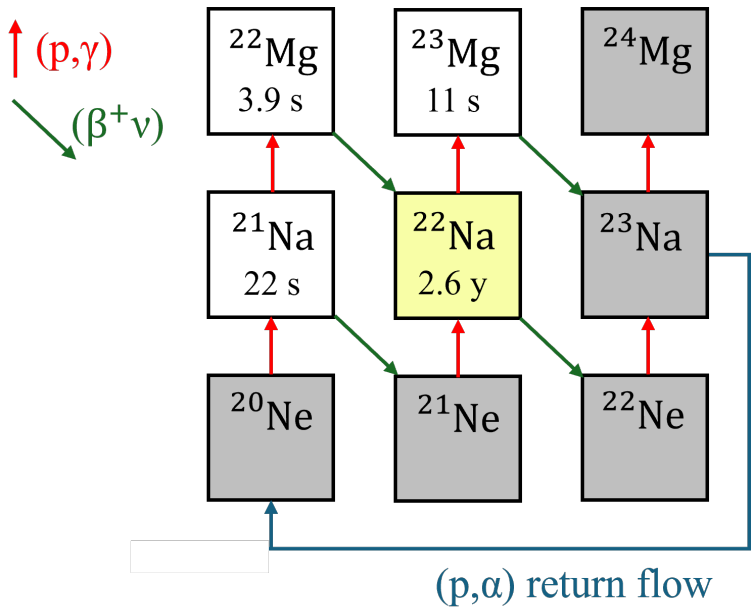

Figure 1.3 Isotopes and reactions involved in the NeNa cycle of hydrogen burning. ^{22}Na is highlighted in yellow for visual clarity. Gray shading indicates stable nuclei. Half-lives from [11, 12, 13].

characteristic 1275 keV gamma ray, as shown in Figure 1.4.

1.4 CCSN Production of ^{22}Na

A core-collapse supernova (CCSN) occurs when the iron core of a massive star (> 11 $M_{\odot}$) grows to a point that electron degeneracy pressure can no longer stabilize it, leading to collapse. The core will collapse until repulsion from the short-range nuclear force stops it. The infalling material will then rebound and generate a shockwave propagating outward [15]. Explosive nucleosynthesis occurs as the shockwave passes through the outer shells of the star [1, 16].

At CCSN shock peak temperatures of about 1.1 GK, ^{19}Ne(α, p)^{22}Na contributes to the production of ^{22}Na, as well as ^{20}Ne(p,γ)^{21}Na(p,γ)^{22}Mg(β^+)^{22}Na. However, in this case ^{22}Mg(α, p)^{25}Al also contributes to the destruction of ^{22}Mg. The rate of the ^{22}Na(p,γ)^{23}Mg reaction is also still uncertain in the temperature regions relevant for supernovae (0.6-1.1 GK) [17].

1.5 Ne-E Meteorites

Some meteorites date back to the birth of the solar system around 4.6 billion years ago, and contain records of times before. These primitive meteorites have undergone very little thermal

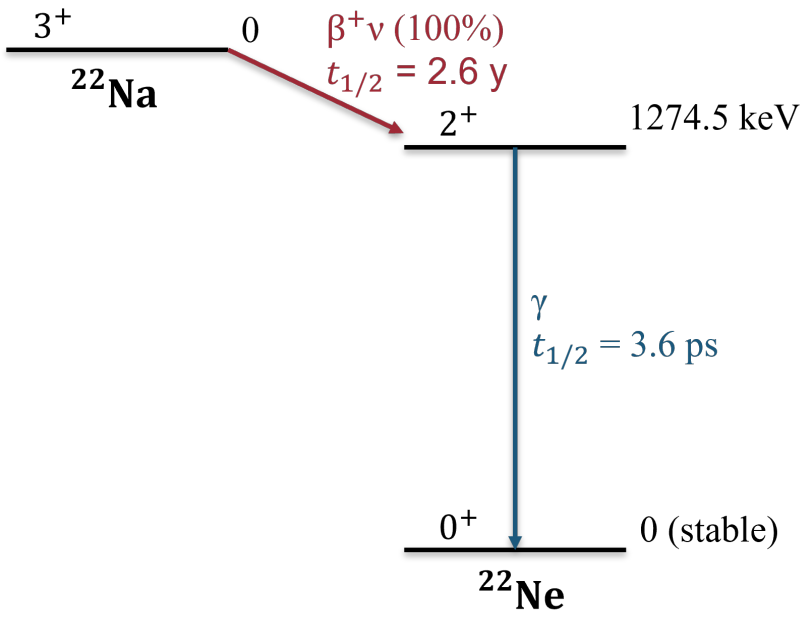

Figure 1.4 Decay scheme of ^{22}Na [12].

alteration since their formation, which means they can be used to glean information about the time before the existence of our solar system. Isotopic ratios of elements such as noble gases that are different from those seen in our solar system are found in presolar grains, which were formed in stellar ejecta before the time of our solar system and later incorporated into these ancient meteorites. Noble gases in meteorites can be produced in situ through radioactive decay, remaining embedded and trapped within the crystalline lattice of the minerals.

The neon content of graphite in certain meteorites, including the Murchison meteorite shown in Figure 1.5, has been analyzed and found to have abnormally high amounts of ^{22}Ne. These meteorites gained the name Ne-E meteorites. The component Ne-E can be further divided into Ne-E(L) and Ne-E(H). Ne-E(L) is released when samples are heated to relatively low temperatures (500°C-700°C) and is generally found in lower density materials than Ne-E(H). Ne-E(H) is released when samples are heated to higher temperatures (1200°C-1400°C) and are found in higher density materials. The ^{22}Ne in Ne-E(H) is thought to be produced in asymptotic giant branch (AGB) stars through the reactions ^{14}N(α,γ)^{18}F(e$^+$ ν)^{18}O(α,γ)^{22}Ne, while the ^{22}Ne in Ne-E(L) is thought to mostly be from the decay of ^{22}Na, though some is thought to come from AGB stars as well

Figure 1.5 Photo of a Murchison meteorite fragment, from [20].

[18]. AGB stars are the last evolutionary stage of stars in the approximate mass range of 0.4-11 $M_{\odot}$ [1]. They feature hydrogen and helium burning shells around an electron-degenerate carbon-oxygen or oxygen-neon-magnesium core, depending on the mass. Only the most massive AGB stars (approximately 9-11 $M_{\odot}$) will have an oxygen-neon-magnesium core [19, 1].

The ratio of ^{20}Ne/^{22}Ne in the solar system is typically determined to be around 13-14. This has been determined through measuring the ^{20}Ne/^{22}Ne ratios in solar wind [21] and the Earth's mantle [22, 23], for example. However, the ratio of ^{20}Ne/^{22}Ne in Ne-E meteorites has been measured to be as low as $\leq$0.15 [24].

Isotopic ratios analyzed in presolar grains on the lowest end of the low density material classification suggest supernovae as the source of the ^{22}Na which decayed into ^{22}Ne. However, the ^{22}Ne in the presolar grains on the denser end of the low density material classification could come from

the decay of ^{22}Na produced in novae [18].

1.6 Observational astronomy

Using space-based telescopes to detect gamma and other radiation in the universe can provide extensive information about the history of the universe, including about ancient and ongoing nucleosynthesis. The products of nucleosynthesis emit identifying signatures such as characteristic gamma rays which can be detected and then analyzed to infer information about the sites and processes that produced them.

1.6.1 ^{26}Al

In the fall of 1979 and the spring of 1980, two separate two-week observation periods were completed by the third High Energy Astronomy Observatory (HEAO-3) satellite. This satellite included a gamma ray spectrometer consisting of four high purity germanium (HPGe) detectors detectors, and was launched with the purpose of detecting gamma rays from nuclear processes [25]. In 1982, a paper was published claiming that the 1.8 MeV gamma ray associated with the decay of ^{26}Al had possibly been detected during these observations [26], and the detection was confirmed in 1984 [27].

^{26}Al decays from its ground state to the first excited state in ^{26}Mg. This β^+ decay has a half-life of 7.17×10^5 years, and the first excited state in ^{26}Mg will decay to its ground state, emitting a 1.8 MeV gamma ray. Since the half-life of this deexcitation is only 476 fs [28], the gamma ray would be absorbed at the site of its nucleosynthesis were it produced directly instead of populated by the decay of ^{26}Al. Thus, the detection of this 1.8 MeV gamma ray indicates the presence of ^{26}Al. Though the half-life of ^{26}Al is longer, it is still short enough that detection of its presence indicates active nucleosynthesis in the universe, and its detection in the 1980's was the first detected evidence of active nucleosynthesis.

Although the half-life of ^{26}Al is short enough that it confirms the existence of active nucleosynthesis sites in the universe, it is long enough that the ^{26}Al cannot be associated with the specific stellar site that produced it. In 1991, NASA launched the Compton Gamma-Ray Observatory (CGRO) with the COMPTEL Compton imaging telescope aboard. A 1992 all-sky survey narrowed

down the source of ^{26}Al to galactic sources [29].

Models and understanding of the astrophysical environments that regulate the production and destruction of ^{26}Al point to a handful of candidates as sites of its nucleosynthesis, including Wolf-Rayet stars, red giants in the AGB phase, novae, and supernovae, but the actual site or sites and their relative contributions are still unknown.

1.6.2 ^{22}Na

Observation of a nearby nova in other wavelengths can be used to prompt observation by gamma ray telescopes. Novae exhibit a fast increase in luminosity in the optical light curve, to a maximum luminosity of $10^{4-5} L_{\odot}$. As the optical luminosity declines, ultraviolet emission increases. Infrared emission corresponding to dust formation can sometimes be detected after optical and ultraviolet emission. Then the nova envelope will expand and become transparent enough that soft x-rays can be observed [30].

The 2.6 year half-life of ^{22}Na makes it a prominent candidate for detection by observational missions. It is long enough to survive the opaque phase of a nova, but still short enough that detection of the characteristic 1275 keV gamma ray from its decay could be associated with the specific nova that produced it.

Given the efficiency of a space-based detector, the distance to a nova it observes, the background detected, and the number of counts of the 1275 keV gamma ray detected, an amount of ^{22}Na ejected from that nova can be determined. If that gamma ray is not detected, an upper limit on the amount of ^{22}Na that could be ejected by the nova can be similarly determined.

The CGRO mission in the 1990's that constrained the production of ^{26}Al to galactic sources also used COMPTEL to search for this 1275 keV gamma ray. An investigation of observed novae with established over-abundances of neon resulted in a limit of ejected ^{22}Na of $\leq 2.1 \times 10^{-8}\,\mathrm{M}_{\odot}$ due to lack of positive detection of the 1275 keV gamma ray [31]. Soon after, however, a potential detection of the 1275 keV gamma ray from a CO nova was published, though the publication itself admits that the reported detections are marginal and somewhat questionable due to small significance of the reported detection, and the fact that fits to the observed light curve that do not

follow ^{22}Na decay are just as acceptable as those that do [32]. A later paper by one of the authors from the paper claiming possible detection claimed that the 1275 keV gamma ray was detected from this CO nova, at the 4σ confidence level. This detection would correspond to $10^{-7} M_{\odot}$ of ^{22}Na ejected by the nova, though the distance to the nova and mass of the ejected envelope used to determine this are not very constrained [33].

In 2002, the SPI spectrometer consisting of an array of 19 high-purity germanium detectors aboard the INTEGRAL mission was launched by the European Space Agency, with searching for the 1275 keV gamma ray associated with the decay of ^{22}Na among its objectives [34]. INTEGRAL concluded its scientific mission in March, 2025, with data yet to be analyzed. At the time of this writing, no positive detection of the 1275 keV gamma ray has been announced. The most recent upper bound yet set on the amount of ^{22}Na ejected by a nova based on data taken using SPI is $< 2.0 \times 10^{-7}\,\mathrm{M}_{\odot}$ [35].

The Compton Spectrometer and Imager (COSI) is a NASA mission currently planned to launch in 2027 which plans to search for the 1275 keV gamma ray from ^{22}Na decay with improved sensitivity from the CGRO and INTEGRAL missions of around an order of magnitude at 1.2 MeV expected [36]. The proposed enhanced ASTROGAM (e-ASTROGAM) mission expects a factor of 29 increase in sensitivity from SPI for the 1275 keV gamma ray [37].

The most recent models estimate between $4 \times 10^{-9}\,\mathrm{M}_{\odot}$ and $8 \times 10^{-9}\,\mathrm{M}_{\odot}$ of ^{22}Na will be ejected from an ONe nova [38]. This makes detection by the next generation of higher sensitivity space-based missions very promising.

In the case of CCSN, the yield of ^{22}Na is typically considered to be on the order of $10^{-6} M_{\odot}$. There has yet to be any detection of CCSN ^{22}Na decay, and the predicted detection limits of COSI and e-ASTROGAM will likely not be able to detect ^{22}Na decay from known supernova remnants. However, current models suggest that they should be able to detect ^{22}Na decay should there be a new galactic supernova while they are active [17].

Further improved and more precise models of ^{22}Na ejected by novae are desired to determine the sensitivity required by observational missions to detect the 1275 keV gamma ray from various

distances, as well as to compare with observed results in the case of future detection.

1.7 ^{22}Na(p,γ)^{23}Mg Resonances: Direct Measurements

In order to model the amount of ^{22}Na ejected by a nova, constraints must be set on the rate at which ^{22}Na proton captures to ^{23}Mg during the nova. The other relevant reaction and decay rates governing the production and destruction of ^{22}Na are known [14]. The rate at which ^{22}Na is consumed in nova conditions is paired with the rate at which it is produced to determine the final amount ejected that can then be detected.

The reaction rate of a particle induced-reaction such a proton capture can be calculated using

$$N_A\langle\sigma\nu\rangle = \left(\frac{8}{\pi m_{01}}\right)^{1/2} \frac{N_A}{(kT)^{3/2}} \int_0^\infty E\sigma(E)e^{-E/kT}dE \tag{1.1}$$

where m_{01} is the reduced mass of the incident particles, N_A is Avogadro's number, k is the Boltzmann constant, T is the temperature, E is the center of mass energy in MeV, and $\sigma(E)$ is the cross section of the nuclear reaction.

In the case of some reactions, the cross section varies dramatically in the region of specific energies. These energies are known as resonances [1]. Near the proton threshold of this specific reaction, where the reaction rate is likely to be dominated by a single or small number of resonances, statistical models of reaction rates tend to fail, so the reaction rate must be determined by other means [39].

The presence and locations of resonances in the ^{22}Na(p,γ)^{23}Mg reaction were predicted and calculated for proton energies up to 614 keV and published in a 1986 paper [40]. Experimental values to compare with these values were sought.

The results of an experiment that was carried out at the California Institute of Technology's Kellogg Radiation Laboratory searching for resonances in this reaction were published in 1989. Proton energies in the range of 0.400-1.275 MeV were investigated by impinging a proton beam upon a ^{22}Na target. The targets were produced by drying drops of ^{22}NaCl solution in a depression on a Ni-coated Ta backing. No resonances were observed in this experiment [41].

Several resonances in the ^{22}Na(p,γ)^{23}Mg reaction were observed for the first time in an experiment at the Ruhr-Universität Bochum which also utilized an accelerated proton beam impinged

upon ^{22}Na implanted target. A D_2O detector consisting of a tank of heavy water surrounded by proportional counters filled with ^{3}He, and a NaI(Tl) scintillator were used to identify resonances. Once resonances were determined, a Ge detector was used to more precisely measure γ-ray energies and branching ratios for some of the identified resonances.

As the energy of the proton beam impinging upon the target was varied, plots of the yield in the form of gamma ray counts versus proton energy, referred to as excitation functions, were produced. Sharp peaks in the yield indicate the presence of a resonance, and six resonances were attributed to the ^{22}Na$(p,\gamma)^{23}$Mg reaction at E_p = 290, 457, 503, 613, 740 and 796 keV.

The strengths of these resonances were determined by determining the correspondence between the strength and the gamma ray intensity, written as

$$I_\gamma(E_p) = N_p \varepsilon_\gamma(E_\gamma) f_\gamma(E_\gamma) B_\gamma(E_\gamma) W(\theta_\gamma, E_\gamma) Y_\infty(E_p) \tag{1.2}$$

where N_p is the number of incident projectiles, $\varepsilon_\gamma(E_\gamma)$ is the absolute detector gamma ray efficiency at E_γ, $f_\gamma(E_\gamma)$ is the spectrum fraction at E_γ, $B_\gamma(E_\gamma)$ is the branching ratio, and $W(\theta_\gamma, E_\gamma)$ is the gamma ray angular distribution. In this case, the thick-target yield per incident particle $Y_\infty(E_p)$ can be expressed as

$$Y_\infty(E_p) = 0.5\lambda^2 \omega\gamma / \varepsilon_{eff} \tag{1.3}$$

where λ is the DeBroglie wavelength, $\omega\gamma$ is the resonance strength, and ε_{eff} is the stopping power.

The reaction rate specifically of a single narrow resonance can be calculated using

$$N_A\langle\sigma v\rangle = N_A \left(\frac{2\pi}{m_{01}kT}\right)^{3/2} \hbar^2 e^{-E_r/kT} \omega\gamma \tag{1.4}$$

where $\hbar$ is the reduced Planck constant, and E_r is the energy of the resonance. Upper and lower limits for the ^{22}Na$(p,\gamma)^{23}$Mg reaction rate at a range of temperatures were determined using the resonance strengths determined for the 6 measured resonances, as well as some estimated resonance strengths for expected resonances not observed by this experiment. These results were published in 1990 [39].

In 1996, a paper detailing a different experiment at the Ruhr-Universität Bochum investigating the ^{22}Na$(p,\gamma)^{23}$Mg reaction was published. A proton beam impinged upon a ^{22}Na implanted target,

and the energy of the protons was varied between 0.20 and 0.63 MeV. A HPGe detector was used to detect gamma rays, and a 50 mm thick Pb shield was used to reduce the flux from the radioactive ^{22}Na target.

A resonance at E_p = 213 keV was observed for the first time, and resonances at E_p = 290 and 613 keV were also observed. Significant results for the strength of the resonance around E_p = 227 keV were unable to be produced due to loss of most of the target during the investigation of the resonance at E_p = 213 keV. The strength of the new resonance at E_p = 213 keV was determined relative to the resonances at E_p = 290 and 613 keV, rather than absolutely. The resonance strength for this resonance was reported as 1.8 ± 0.7 meV. The state in ^{23}Mg associated with this resonance was reported to be at an excitation energy of 7785 ± 3 keV. Calculations of the ^{22}Na$(p,\gamma)^{23}$Mg reaction rate using the new values from this experiment indicate that the resonance at E_p = 213 keV dominates the rate at nova temperatures [42].

The results of a final direct measurement to date of the resonances in the ^{22}Na$(p,\gamma)^{23}$Mg reaction were published in 2010 [43] and 2011 [44]. The experiment took place at the Center for Experimental Nuclear Physics and Astrophysics of the University of Washington. ^{22}Na implanted targets were bombarded by a proton beam, and HPGe detectors were used for gamma ray detection in tandem with Pb shielding and scintillators for cosmic ray rejection. The proton beam energy was varied over a range of around 25 keV for known resonances at E_p = 213, 288, 454, and 610 keV, as well as for proposed resonances at E_p = 198, 209, and 232 keV.

The resonance strengths were determined absolutely using

$$\int Y dE = 2\pi^2 \lambda\!\!\!^{-2}_{lab} \frac{m+M}{M} N_T \rho_b \omega\gamma \tag{1.5}$$

where Y is the gamma ray yield, $\int Y dE$ is the integral of the excitation function, $\lambda\!\!\!^{-}_{lab}$ is the proton reduced de Broglie wavelength, m is the mass of the proton, M is the mass of the target, N_T is the number of target atoms, and ρ_b is the beam density normalized to the number of incident particles. The normalized beam density can be calculated as

$$\rho_b = \frac{dN_b}{dA} / (Q/e) \tag{1.6}$$

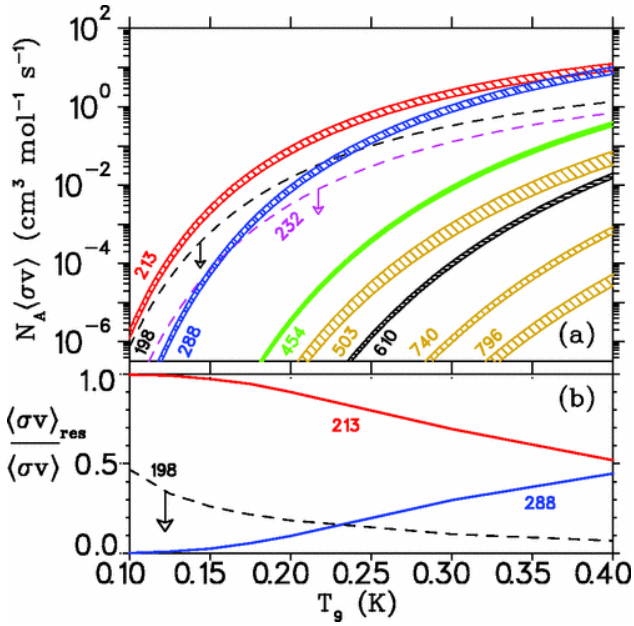

Figure 1.6 Contributions to the ^{22}Na$(p,\gamma)^{23}$Mg reaction rate by individual resonances. Figure from [44].

where $\frac{dN_b}{dA}$ is the areal density of the beam.

The strength of the resonance at E_p = 213 keV was measured to be $5.7^{+1.6}_{-0.9}$ meV, and the associated state in ^{23}Mg was reported at E_x = 7784.6 ± 1.2 keV. All of the resonance strengths determined in this experiment were systematically higher than the results of the previous experiment that observed the resonance at E_p = 213 keV. This work confirmed that the resonance at 213 keV dominates the rate of the ^{22}Na$(p,\gamma)^{23}$Mg reaction at nova temperatures, though the resonance at 288 keV does begin to contribute substantially at the highest end of nova temperatures, as shown in Figure 1.6.

The reaction rate calculated using the results of this experiment is higher than the previously determined rate by around a factor of 3. This leads to a reduction in ^{22}Na ejected by a nova of a factor of 2 or 3, depending on the nova model used.

1.8 Indirect measurements

The radioactive ^{22}Na targets make direct measurements of the resonance strength difficult. However, the strength of the resonance can also be determined indirectly.

1.8.1 Surrogate Proton Transfer

A paper published in 1995 outlined an experiment that took place at the Beschleunigerlaboratorium der Universität und der Technischen Universität München investigating the ^{22}Na(^{3}He,d)^{23}Mg reaction. Angular distribution data for states in ^{23}Mg populated by this reaction were used to calculate the strengths of ^{22}Na(p,γ)^{23}Mg resonances up to a proton energy of 288 keV, though with large model-dependent uncertainties. The excitation energy of the state in ^{23}Mg associated with the E_p = 212 keV resonance was measured to be 7780 ± 6 keV, and the resonance strength was constrained between 0.29 and 20 meV [45].

1.8.2 Spin, Proton Branching Ratio, and Lifetime

Resonance strengths can also be determined using

$$\omega\gamma = \frac{2J+1}{(2J_p+1)(2J_{\mathrm{Na}}+1)}\frac{\hbar}{\tau}B_p(1-B_p) \tag{1.7}$$

where J is the spin of the resonance, J_p = 1/2 is the spin of the incident proton, J_{Na} = 3 is the spin of the ^{22}Na, τ is the lifetime of the state in ^{23}Mg corresponding to the resonance, and B_p is the proton decay branching ratio. Thus, in order to determine the resonance strength indirectly, the spin of the resonance, the proton branching ratio, and the lifetime of the state must also be determined.

1.8.2.1 Spin

There is some uncertainty in the spin of the resonance. An experiment at Argonne National Laboratory probing the radiative decay branches in ^{23}Mg via the fusion reaction ^{12}C(^{12}C,n)^{23}Mg determined a spin and parity of $7/2^{(+)}$ for the state of interest [46, 47]. A study of β-delayed proton decay of ^{23}Al determined the spin and parity of the state to be $(7/2)^+$ [48]. A comparison of a measurement of the β-decay strength of the state of interest to that predicted by a shell model calculation led to the proposal of a spin and parity of $5/2^+$, interestingly as a split isobaric analog state (IAS) to the ground state in ^{23}Al where both the 7787 keV state and the state at 7803 keV share a spin and parity of $5/2^+$ [49]. An additional study of β-delayed proton decay of ^{23}Al determined a spin and parity of the state of interest of $(7/2)^+$[50], though a doctoral thesis based on the same work expanded the options to be $(5/2, 7/2)^+$ [51]. Yet another experiment, which observed the

deuteron angular distribution in a ^{24}Mg(p,d)^{23}Mg transfer reaction and compared the results to distorted wave born approximation (DWBA) calculations to constrain the spin and parity of the state of interest to $(3/2^+, 5/2^+)$. Due to the previous observation of β-delayed proton emission for the level, $5/2^+$ is favored [52].

In general, $3/2^+$ is not a favored value for the spin, because the beta-delayed proton emission of ^{23}Al, whose ground state has a spin of $5/2^+$, does populate this state. The ground state of ^{22}Na has a spin of 3^+, and the proton emission from $3/2^+$ to 3^+ is suppressed by the relatively large centrifugal barrier. Strong isospin mixing with the IAS at 7803 keV is not observed, which leads a spin of $7/2^+$ to generally be favored over a spin of $5/2^+$ [53, 38]

However, due to the overall uncertainty, and standing discrepancies in experimental determinations of the resonance strength, $3/2^+$, $5/2^+$, and $7/2^+$ should all be considered appropriately in an indirect calculation of the resonance strength. $11/2^+$ is also worth investigating to check for potential population of an additional state at 7780 keV that was assigned a spin and parity of $11/2^+$ in [47].

1.8.2.2 Proton Branching Ratio

A measurement of the proton branching ratio used the ^{24}Mg(p,$2n$) reaction to produce ^{23}Al. The ^{23}Al β-decays to high-lying excited states in ^{23}Mg, which will then undergo proton decay to ^{22}Na. This experiment, which took place at Lawrence Berkeley Laboratory, observed proton peaks at four locations. The relative yields between peaks were used to calculate a proton branching ratio of 0.035 ± 0.019 for the state of astrophysical interest. This result was published in 1995 [54]. Later papers have claimed that the peak used to obtain this result was likely misinterpreted background, and thus this result can be disregarded [48, 55].

A second measurement of the proton branching ratio was published in 2000. The β-delayed proton decay of ^{23}Al was observed at the University of Jyväskylä via the ^{24}Mg(p,$2n$), and proton and gamma emission were both observed. Analysis of both the proton and gamma emissions from the state of interest gave a proton branching ratio of $10(8)\times10^{-3}$ [56]. It was originally thought that this was an observation of the IAS of the ground state in ^{23}Al, but a later experiment determined

that it was likely the 7787 keV state being populated [48].

A third measurement of the proton branching ratio took place at the Cyclotron Institute of Texas A&M University, using the ^{24}Mg(p,$2n$) reaction in inverse kinematics to produce ^{23}Al. A proton branching ratio for the state of interest of $3.7(9)\times10^{-2}$ was determined and published in 2011 [48].

An experiment at the National Superconducting Cyclotron Laboratory (NSCL) used a gaseous detector to detect charged particles emitted in the decay of a ^{23}Al beam. A germanium array was used to detect coincident gamma rays. A proton branching ratio for the state of interest of $6.5(8)\times10^{-3}$ was reported in 2020 [55].

The most recent measurement of the proton branching ratio was published in 2023. A ^{24}Mg beam was produced at GANIL and was used to populate excited states in ^{23}Mg via ^{3}He(^{24}Mg,α). Protons were detected using an annular silicon detector downstream of the target. A branching ratio of $6.8(17)\times10^{-3}$ was determined [38].

1.8.2.3 Lifetime

The first measurement of the lifetime of the key excited state in ^{23}Mg was published in 2004. The fusion reaction ^{12}C(^{12}C,n)^{23}Mg populated excited states in ^{23}Mg, from which lifetime data was extracted. The fractional Doppler shift technique, wherein the Doppler shifts of the centroids of gamma ray peaks are determined at various detector angles, was used to determine the lifetime of the state. A lifetime of 10 ± 3 fs was reported. This experiment determined the excitation energy of the state of interest to be 7784.6(11) keV [46], though interestingly it also claims to have found a state at 7780 keV with a spin and parity of $11/2^+$ [47], as mentioned previously in section 1.8.2.1.

The attempt of a second measurement of the key lifetime was published in 2016. States in ^{23}Mg were populated via ^{3}He(^{24}Mg,α) at the ISAC-II facility of TRIUMF. Lifetimes of various states were determined using the Doppler Shift Attenuation Method (DSAM). See section 2.1 for further information about DSAM. An upper limit of < 12 fs was set for the lifetime of the key excited state, which corresponds to a lower limit on the resonance strength that can be determined using this value [57].

The most recent lifetime value reported for the ^{23}Mg state of interest was published in 2023.

This experiment also populated states in ^{23}Mg via the ^{3}He(^{24}Mg,α) reaction. The gamma ray yields were plotted against the difference in the velocity of the ^{23}Mg at the time of the reaction and at the time of the gamma ray emission. The velocity at the time of the reaction was determined using the momentum of the emitted α particles measured by a magnetic spectrometer and the laws of energy and momentum conservation. The velocity at the time of the gamma ray emission was calculated using

$$E_\gamma = E_{\gamma,0}\frac{\sqrt{1-\beta_{ems}^2}}{1-\beta_{ems}\cos(\theta)} \tag{1.8}$$

where E_γ is the measured energy, shifted from the center-of-mass energy $E_{\gamma,0}$, β_{ems} is the velocity of the ^{23}Mg at the time of the gamma ray emission, and θ is the angle between the gamma ray and the ^{23}Mg, which was derived from the measured angles of the emitted gamma rays and α particles. It is unclear if the nuclear recoil of the ^{23}Mg when the gamma ray is emitted, was taken into account. This can lead to a difference of around 1 keV in the gamma ray energy determined. Monte Carlo simulations were compared to the lineshapes of plots of gamma ray counts against the difference in velocities at the time of the reaction and at the emission of the gamma ray, $\beta_{reac} - \beta_{ems}$. This method resulted in a lifetime value of 11^{+7}_{-5} fs for the state of interest [38].

1.9 Summary of Previous Experiments

A summary of the experiments probing the key resonances of the ^{22}Na(p,γ)^{23}Mg reaction and their results is given in Table 1.1.

The resonance strengths of the key resonance in the ^{22}Na(p,γ)^{23}Mg reaction determined by the two direct measurements, as well as those calculated using lifetime measurements of ^{23}Mg state associated with the resonance are plotted in Figure 1.7. The most recent and sensitive indirect measurements of the resonance strength are further discrepant from both direct measurements, to the extent that the direct measurements would not have been able to observe the resonance if it were as weak as the indirect measurements indicate.

Simulations suggest that the mass of ^{22}Na ejected from a nova goes like $\tau^{0.7}$ [38]. The detectability distance of the ^{22}Na then goes like the square root of the amount of mass ejected. Figure 1.8 shows how the ejected mass of ^{22}Na varies with the lifetime of the key excited state,

Ref.	Method	τ (fs)	J^π	E_x (keV)	E_γ (keV)	B_p	$\omega\gamma$ (meV)
[45]	^{23}Na(^{3}He,d)	–	–	–	–	–	0.29 – 20
[42]	^{22}Na(p,γ)	–	–	7785(3)	7334	–	1.8 ± 0.7
[56]	^{23}Al($\beta\gamma$)	–	≥ 3/2+	7784(3)	–	10(8)×10^{-3}	0.4(3)^a
[46] [47]	^{12}C($^{12}C,n$)	10(3)	(7/2$^+$) [46] 7/2$^{(+)}$ [47]	7784.6(11)	7333.7(11)	–	–
[50]	^{23}Al($\beta\gamma$)	–	(7/2$^+$)	7787.4	7335.1	–	–
[51]	^{23}Al($\beta\gamma$)	–	(5/2$^+$, 7/2$^+$)	7787.2(6)	7335.2(6)	–	–
[43, 44]	^{22}Na(p,γ)	–	–	7784.7(12)	7332.7(12)	–	$5.7^{+1.6}_{-0.9}$
[48]	^{23}Al($\beta\gamma$)	–	(7/2)$^+$	7786.9(5)	7335	3.7(9)×10^{-2}	$1.4^{+0.5}_{-0.4}$ ^{b}
[57]	^{3}He(^{24}Mg,α)	<12	–	7787.2(6)	7335	–	> 0.16 ^{c}
[52]	^{24}Mg(p,d)	–	3/2$^+$, 5/2$^+$	7788(5)	–	–	–
[55]	^{23}Al($\beta\gamma$)	–	(7/2)$^+$	7787.2(5)	7335.1(9)	6.5(8)×10^{-3}	0.24(8)^b
[38]	^{3}He(^{24}Mg,α)	11^{+7}_{-5}	7/2$^+$	7785.0(7)	$7333.0^{+0.5}_{-0.2}$	6.8(17)×10^{-3}	$0.24^{+0.11}_{-0.04}$ ^{d}

Table 1.1 Summary of results from experiments investigating the ^{22}Na(p,γ)^{23}Mg. The gamma ray energy listed is for the transition from the state of astrophysical interest to the first excited state in ^{23}Mg. *a*) From [55], using the lifetime value from [46]. *b*) Using the lifetime value from [46] *c*) From [55], using the branching ratio from [55]. *d*) Calculated using all measured values.

assuming a 1.25 $M_\odot$ ONe white dwarf, and an ejected mass of $7 \times 10^{-9} M_\odot$ at a lifetime of 10 fs [38].

A new lifetime measurement that is also sensitive to the uncertainties in the spin and excitation energy of the state of interest could shed light on the underlying cause of the discrepant resonance strength measurements and provide updated information for use in models of ^{22}Na ejected by a nova in advance of the upcoming COSI mission.

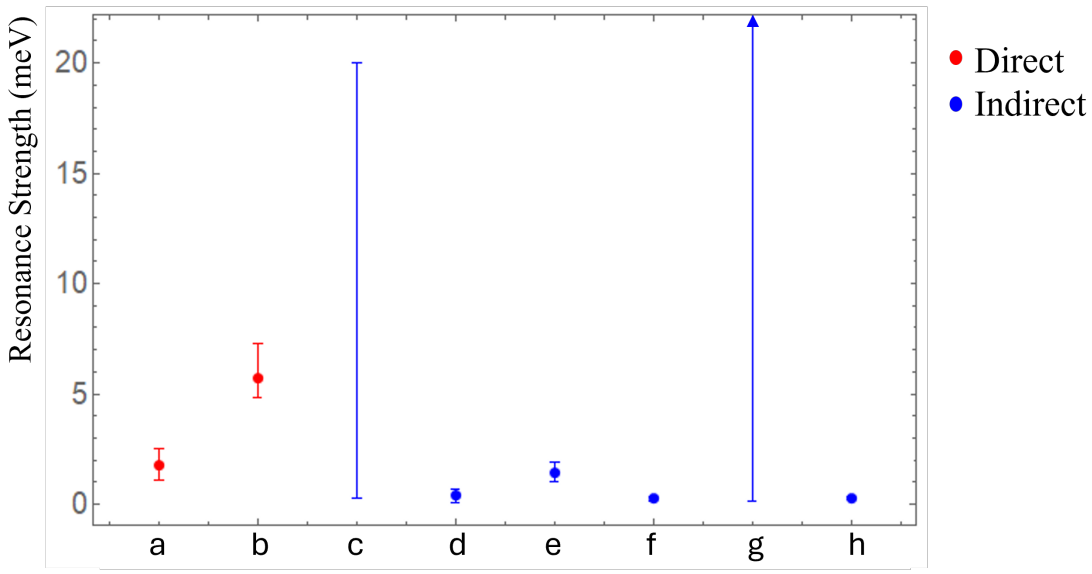

Figure 1.7 Resonance strengths determined for the key resonance of the ^{22}Na(p,γ)^{23}Mg reaction. a) From [42]. b) From [43]. c) From [45] d) From [56], value from [55] calculated using the lifetime value from [46]. e) From [48], calculated using the lifetime value from [46]. f) From [55], calculated using the lifetime value from [46]. g) From [55]. A lower limit on the resonance strength calculated using the upper limit on the lifetime from [57]. h) From [38].

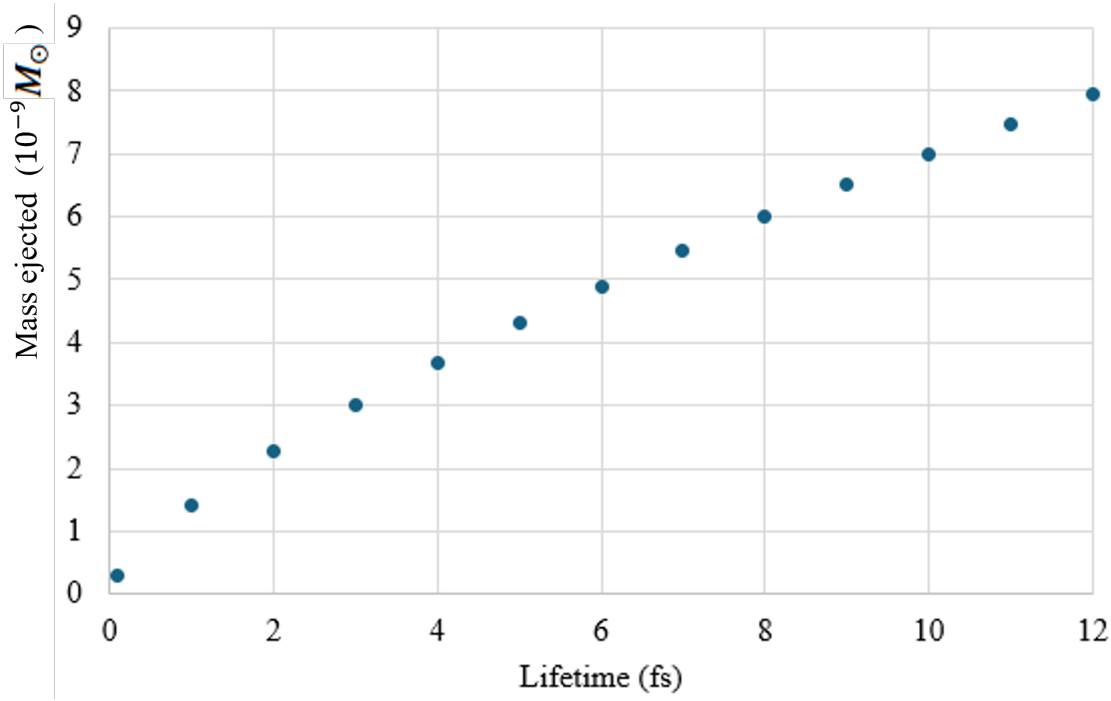

Figure 1.8 Plot of the trend of ejected ^{22}Na as the lifetime of the key excited state in ^{23}Mg changes. Assumes a 1.25 $M_\odot$ ONe white dwarf, and an ejected mass of $7 \times 10^{-9} M_\odot$ at a lifetime of 10 fs [38].

CHAPTER 2

THE DOPPLER SHIFT LIFETIMES SETUP

The Doppler Shift Lifetimes (DSL) setup at TRIUMF in Vancouver, Canada has been used to make measurements of the lifetimes of excited states in several nuclei. The setup consists primarily of a ΔE-E telescope and one or more HPGe detectors. Lifetimes are extracted from data taken with the DSL setup using the Doppler Shift Attenuation Method (DSAM). This chapter describes the two iterations of DSL–DSL1 and DSL2–as well as the fundamentals of DSAM and solid-state detectors such as those used in DSL.

2.1 Doppler Shift Attenuation Method

The lifetimes of excited states in nuclei vary across a wide range, depending on the structure of the nucleus, the decay mode, and in the case of electromagnetic transitions, the multipolarity and energy of the transition. Different methods are more suitable to determining lifetimes within different ranges. There is some overlap in the ranges in which different techniques can reliably measure nuclear lifetimes, but generally electronic timing techniques are used to measure lifetimes down to the nanosecond level, recoil distance methods are used to measure lifetimes within the range of a few picoseconds to nanoseconds, and DSAM can be used to measure lifetimes in the range of a few femtoseconds to a few picoseconds [58]. Techniques including the partial x-ray coincidence technique (PXCT) can be used to determine even shorter lifetimes in the $10^{-17} - 10^{-15}$ s range.

PXCT [59] involves detecting x-rays in coincidence with charged particles such as protons. The ratio of the x-rays associated with the charged particle-emitting nucleus to those associated with the daughter nucleus can be used in comparison with known atomic lifetimes to determine the lifetime of the charged particle-emitting state [60]. Electronic techniques rely on the distribution of time delays from the creation to deexcitation of the nucleus following the decay relation

$$dI(t)/dt = I_0 \lambda e^{-\lambda t} \tag{2.1}$$

Recoil distance methods allow the nucleus to travel through vacuum for a set distance, after which

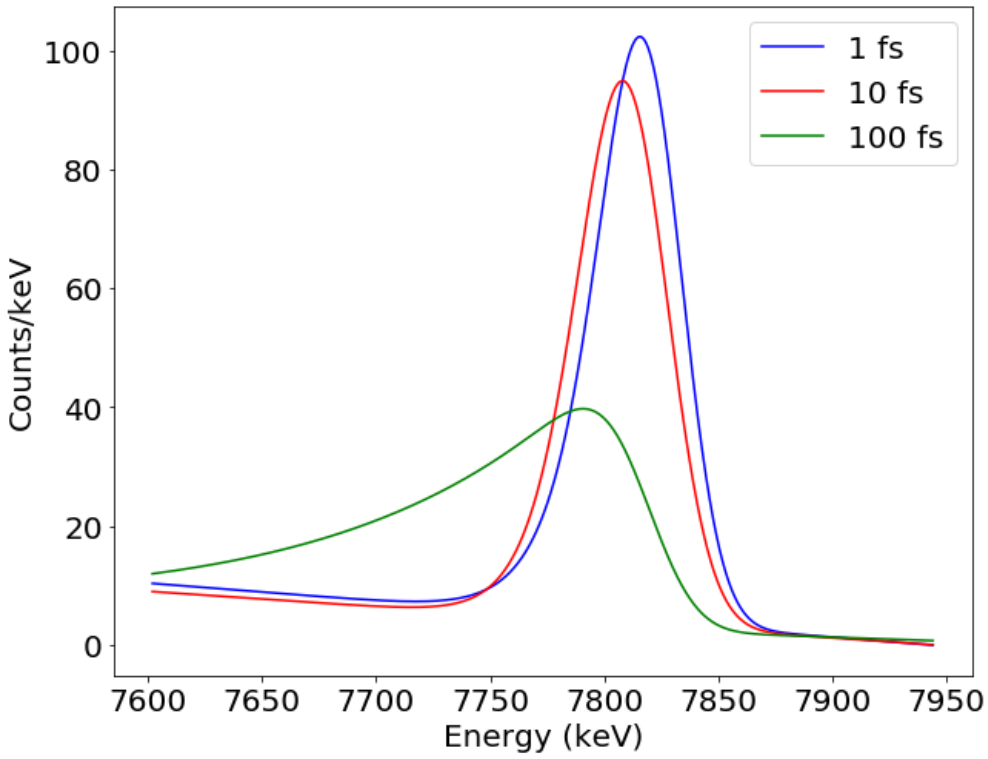

Figure 2.1 Simulated effect of different lifetimes on the gamma peak from the astrophysically significant excited state in ^{23}Mg. Population via ^{3}He($^{24}Mg,\alpha$)^{23}Mg* with a ^{24}Mg energy of 74 MeV at the time of reaction, and an excitation energy of 7785 keV used in the simulation.

it encounters a metal stopper. The discreet Doppler shift between the gamma rays emitted in the vacuum and those emitted by nuclei that have been stopped can be used to determine the lifetime of the state [58].

If an ensemble of nuclei can deexcite and emit gamma rays before coming to a stop, the shape as well as the location of the peak will be affected, depending on the lifetime of the state. DSAM utilizes lineshape analysis of Doppler shifted gamma rays to determine lifetimes. Figure 2.1 shows a simulation illustrating the difference in gamma peak shape and location due to the Doppler shift, assuming different lifetimes of the same state.

The Doppler shifted energy of the emitted gamma ray is given by

$$E = E_0 \frac{\sqrt{1-\beta^2}}{1-\beta\cos\theta} \tag{2.2}$$

where E_0 is the rest energy of the gamma ray, $\beta = v/c$, and θ is the angle between the emission direction and the observer. For a nucleus in a stopping medium, such as those created by nuclear

reactions of beam particles with particles implanted in a target substrate, the velocity of the particle and thus also β are time dependent. In order to model the distribution of Doppler shifted gamma rays for the lineshape analysis, the rest energy of the gamma ray and the stopping power of the target material, which corresponds to the time dependence of β, are necessary. The target material is chosen such that the ion stopping time within the medium, which depends on stopping power and density of the medium and energy of the ions, is on the order of the lifetime of the excited states to be measured.

Many experiments utilizing DSAM, including the one discussed in this work, utilize inverse kinematics. Inverse kinematics refers to impinging a heavy beam upon a light target. The use of inverse kinematics is favorable for lifetime measurements utilizing DSAM for several reasons, including the fact that recoil velocities tend to be larger for a given center-of-mass energy than when impinging a light beam upon a heavy target, leading to greater Doppler shifts. Recoil velocities in experiments employing inverse kinematics also tend to be close to the velocities at which the stopping power of the target material is at a maximum, which increases the sensitivity of the measurement [61].

2.2 Semiconductor Detectors

Germanium and silicon are semiconductors that can be utilized for radiation detection. Semiconductor detectors have the best energy resolution of the radiation spectrometers that see widespread use. These detectors are frequently referred to as semiconductor diode detectors or solid-state detectors.

The lattice structure seen in crystalline solids results in allowed energy bands for the electrons of the solid. The lower energy band is known as a valence band. The electrons in the valence band are the outer electrons that are bound within the crystal, or participate in covalent bonding in materials such as germanium and silicon. There is a higher energy band known as the conduction band. Electrons in the conduction band are free to flow in the material.

Metals have valence bands that are not completely full, which leads to high electrical conductivity because the charge carriers can move throughout the material with only a small amount of

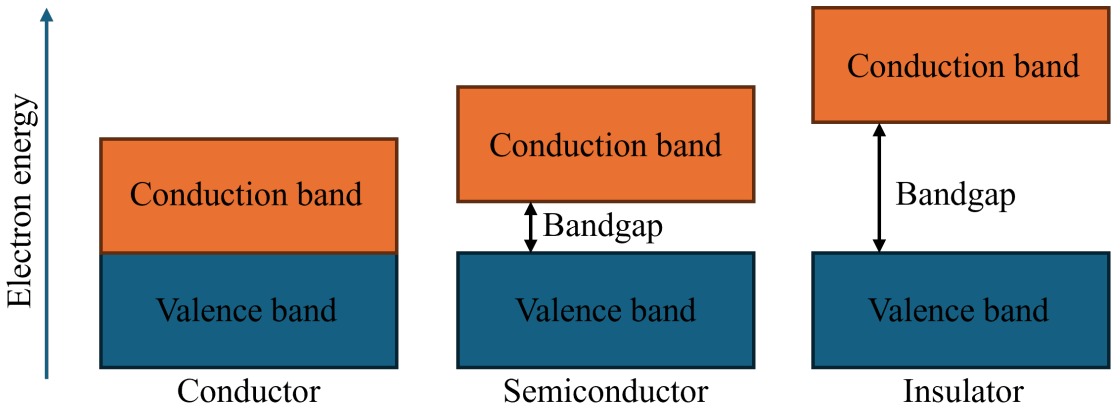

Figure 2.2 Illustration of the band structure for conductors, semiconductors, and insulators.

energy input. Insulators and semiconductors have a full valence band, and the valence band and conduction band are separated by the bandgap, as shown in Figure 2.2. Electrons must cross the bandgap in order to reach the conduction band, which limits the conductivity of the material. The bandgap for an insulator is generally greater than 5 eV. Semiconductors are an intermediate case, with a bandgap of around 1 eV [62].

Impurities can be introduced into the lattice of a semiconducting material in order to increase its electrical conductivity. This is referred to as doping. The dopant has an electron structure such that when covalent bonds are formed with the surrounding semiconductor material, there is at least one electron or hole left over, which is only weakly bound to its original site. This means only a small amount of energy is required to turn these electrons into conduction electrons.

When ionizing radiation moves through a solid-state detector, it creates electron-hole pairs along its path by exciting an electron in a covalent bond within the valence band across the bandgap to the conduction band so it can move throughout the crystal, leaving behind a vacancy in the valence band. A reverse bias voltage is applied to prevent the electron-hole pairs from recombining to reestablish equilibrium so they instead drift in opposite directions in the material. The number of electron-hole pairs produced is proportional to the energy of the ionizing radiation. Silicon and germanium semiconductor detectors generally rely on the integration of the currents from both the movement of the electrons and the holes.

The voltage applied in order to efficiently collect the charge carriers will cause conductivity, resulting in a discernible leakage current. Random fluctuations in the leakage current results in noise in the detected spectrum, so efforts to reduce leakage current are taken when semiconductor detectors are designed. At higher temperatures, more electron-hole pairs can be thermally generated, so semiconductor detectors are often cooled to further reduct leakage currents.

In the case of Si detectors used to detect heavy charged particles such as alpha particles, interactions between the charged particles and the detector material are driven by coulomb forces between the charged particles and the negatively-charged orbital electrons of the detector. It is possible for the charged particles to interact directly with the detector nuclei, though this is rare. These charged particles will typically not be deflected by any encounter with the detector and will thus travel in straight paths, but will eventually lose enough energy to these interactions to come to a stop.

Si detectors can be used as particle identifier telescopes, in which a thinner Si detector, referred to as the ΔE detector, is placed in front of a thicker Si detector, which is referred to as the E detector. A charged particle incident to this ΔE-E telescope will deposit some of its energy in the ΔE detector, then continue on to deposit more (ideally the rest) of its energy in the thicker E detector. The amount of energy deposited in each detector depends on the stopping power, which is in turn dependent on the mass and charge of the particle. ΔE-E telescope detector thicknesses are determined such that particles of interest in a specific case within expected energy ranges will come completely to a stop within the E detector. More information on using ΔE-E telescopes for particle identification is given in section 4.4.

Gamma rays can interact with matter in several ways, but in the case of radiation detection, there are three specific mechanisms that dominate the interactions of the gamma rays with the detector material.

The first is photoelectric absorption, which dominates at low gamma ray energies (up to a few hundred keV). Photoelectric absorption occurs when an incident gamma ray photon interacts with a Ge atom in a HPGe detector and is completely absorbed. Its energy, $h\nu$, is transferred to an atomic

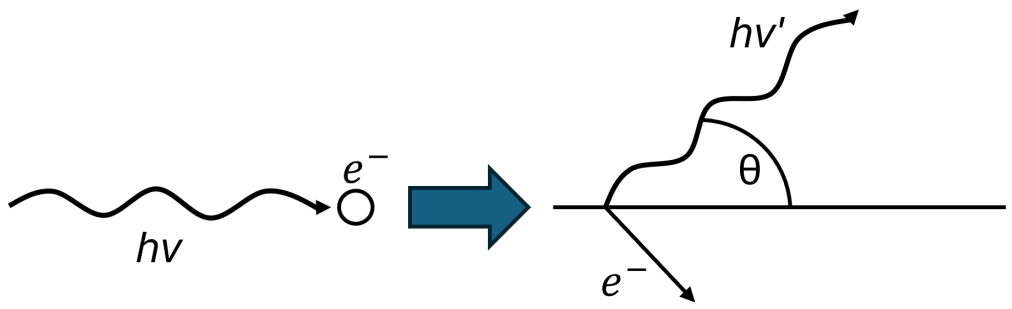

Figure 2.3 Photon and electron before Compton scattering interaction (left) and after interaction (right).

electron, which is then emitted with energy

$$E_{e^-} = h\nu - E_b \tag{2.3}$$

where E_b is the electron's binding energy in its original shell.

The second interaction mechanism is Compton scattering, which dominates at gamma ray energies from a few hundred keV to a few MeV. Compton scattering results in the production of a recoil electron and a scattered gamma ray. The incident gamma ray transfers some of its energy to the electron, with the energy division between the two being dependent on the scattering angle. The energy of the electron is given as

$$E_{e^-} = h\nu \left(\frac{(h\nu/m_0c^2)(1-\cos\theta)}{1+(h\nu/m_0c^2)(1-\cos\theta)} \right) \tag{2.4}$$

where m_0c^2 is the rest mass energy of an electron, equal to 511 keV, and θ is the scattering angle as illustrated in Figure 2.3.

The maximum energy that can be transferred to an electron in a Compton interaction corresponds to a head-on collision, where $\theta = \pi$. All other scattering angles can occur, which leads to an energy continuum below the full energy of the incident gamma ray. The maximum energy transfer of a head-on collision corresponds to the drop off of the continuum, known as the Compton edge.

The last main interaction mechanism is pair production. Pair production is possible starting from 1022 keV–twice the electron rest mass–and it dominates above a few MeV. A gamma ray with an energy above 1022 keV can interact with a nucleus within the coulomb field of that nucleus and

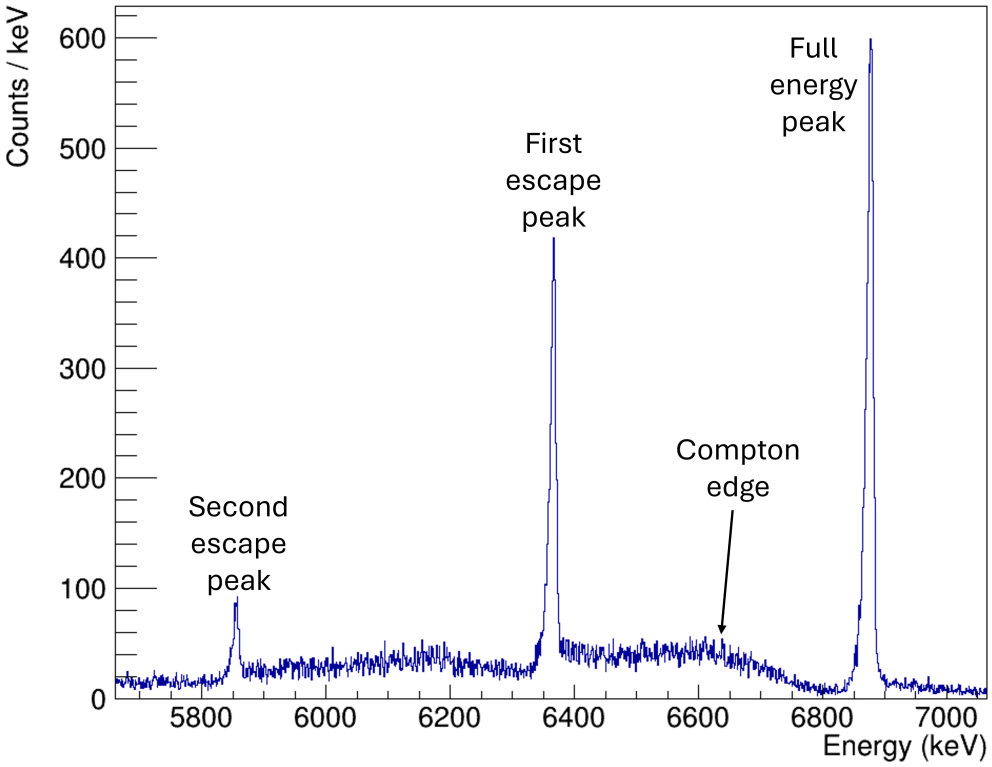

Figure 2.4 Simulation of the gamma spectrum for the 6.88 MeV peak from ^{28}Si with the full energy peak, first and second escape peaks, and Compton edge indicated.

produce an electron-positron pair. The incident energy above 1022 keV transfers to kinetic energy that is shared by the electron and positron pair, as represented in the equation

$$E_{e^-} + E_{e^+} = h\nu - 2m_0c^2 \tag{2.5}$$

The positron will annihilate with another electron, producing two 511 keV photons. If one of the annihilation photons escapes the detector, a peak known as the first escape peak will arise 511 keV below the peak at the full energy of the incident gamma ray. If both annihilation photons escape, the second escape peak will occur at 1022 keV below the full energy peak.

Figure 2.4 indicates the features of a gamma spectrum due to these processes.

HPGe detectors often consist of four tightly arranged Ge crystals within one cryostat. Detectors in this configuration are referred to as clover detectors. Ge has a low bandgap, which results in a relatively high probability for electron-hole pairs to be generated thermally. For this reason, HPGe detectors are cryogenically cooled with liquid nitrogen in order to reduce noise in the gamma

spectrum. The low bandgap lends itself to good energy resolutions due to more charge carriers per unit energy, on the order of a few hundred eV to a few keV full width at half maximum (FWHM) depending on the energy of the incident radiation. Si has a higher bandgap, which results in somewhat worse energy resolutions of around a few keV to a few tens of keV FWHM.

2.3 DSL1

The DSL setup at TRIUMF is used to measure gamma rays in coincidence with charged particles produced in the reactions that populate excited states in nuclei in order to make lifetime measurements of primarily astrophysically significant states using DSAM.

The first iteration of the DSL setup, DSL1, was completed in 2005 [63]. It was first built to measure the lifetime of the 4.03 MeV state in ^{19}Ne, which corresponds to the key resonance in the ^{15}O$(\alpha,\gamma)^{19}$Ne reaction under the conditions of an X-ray burst [64]. A successful lifetime measurement was published in 2006 [65], and the results of an improved measurement with cleaner targets were published in 2008 [66].

DSL1 was later used to set an upper limit of 1.8 fs on the lifetime of the 6.79 MeV state in ^{15}O, which has a strong impact on the rate of the limiting ^{14}N$(p,\gamma)^{15}$O reaction in the CNO cycle. These results were published in 2014 [67].

DSL1 was used to set the 12 fs upper limit on the key excited state in ^{23}Mg, published in 2016, as discussed in the previous chapter [57]. It was also used in an experiment attempting to measure the lifetime of the 6.390 MeV state in ^{31}S corresponding to the key resonance of the ^{30}P$(p,\gamma)^{31}$S reaction which limits the flow to heavier masses in nova nucleosynthesis. The lifetimes of several states in ^{31}S were determined or constrained, but limited statistics prevented a determination of the key lifetime. [68].

DSL1 primarily utilized a HPGe detector placed at 0° with respect to the beam to detect gamma rays, though in some instances a second HPGe detector placed at 90° was used as a reference to determine unshifted energies or monitor the stability of electronics. A Si ΔE-E telescope consisting of two single-channel detectors, each with an active area of 150 mm^2, was used. The ^{19}Ne experiments used a 25 μm-thick ΔE detector and a 500 μm-thick E detector. The ^{15}O and

^{23}Mg experiments utilized a 100 μm-thick ΔE detector and a 500 μm-thick E detector. The ^{31}S experiment initially used a 500 μm-thick ΔE detector and a 1000 μm-thick E detector, though the 500 μm ΔE detector was damaged in a first run of the experiment which failed due to contaminated targets and a poor beam tune, and a 87 μm ΔE detector was used in a second attempt of the experiment [69]. DSL1 experiments all utilized ^{3}He-implanted Au foil targets held in a target ladder in front of the Si detector telescope.

The DSL chamber has a cold trap cooled with liquid nitrogen in order to prevent carbon buildup on the surface of the target. The target ladder is also cooled via BeCu fingers to prevent ^{3}He diffusion from the target, though an insulating ceramic BN plate serves as the point of contact between the target ladder and the shroud to keep the targets at a higher temperature than the cold trap so contaminants do not condense on the target [67]. A turbomolecular pump is used to keep the DSL chamber under vacuum. Two collimators are placed upstream of the target ladder to constrain the beam spot, which decreases uncertainty in the reaction location, which increases the sensitivity of lifetime measurements. The first collimator, furthest upstream at 73 mm from the target, has a diameter of 2.5 mm, and the second collimator at 49 mm from the target has a diameter of 3.0 mm. DSL1 also utilized a third collimator, 14.2 mm downstream from the target, between the target and the ΔE detector. This collimator had a 4 mm diameter aperture, defining and limiting the angular acceptance of the Si detectors to $0 - 8°$.

A schematic of DSL1 is shown in Figure 2.5.

DSL1 is limited by several factors. Higher beam intensities than those used in previous DSL1 experiments will cause the targets to heat and the ^{3}He to diffuse, degrading the targets. This means higher beam rates cannot be used. The ^{3}He density of the targets cannot be increased due to the blistering limit discussed in section 3.1. Therefore detection efficiency is the focus of plans to improve the sensitivity of the setup.

2.4 DSL2

DSL was upgraded to DSL2 in 2022 to increase the angular coverage, which in turn increases the efficiency, and therefore statistics and sensitivity. This work is the first experiment run with the

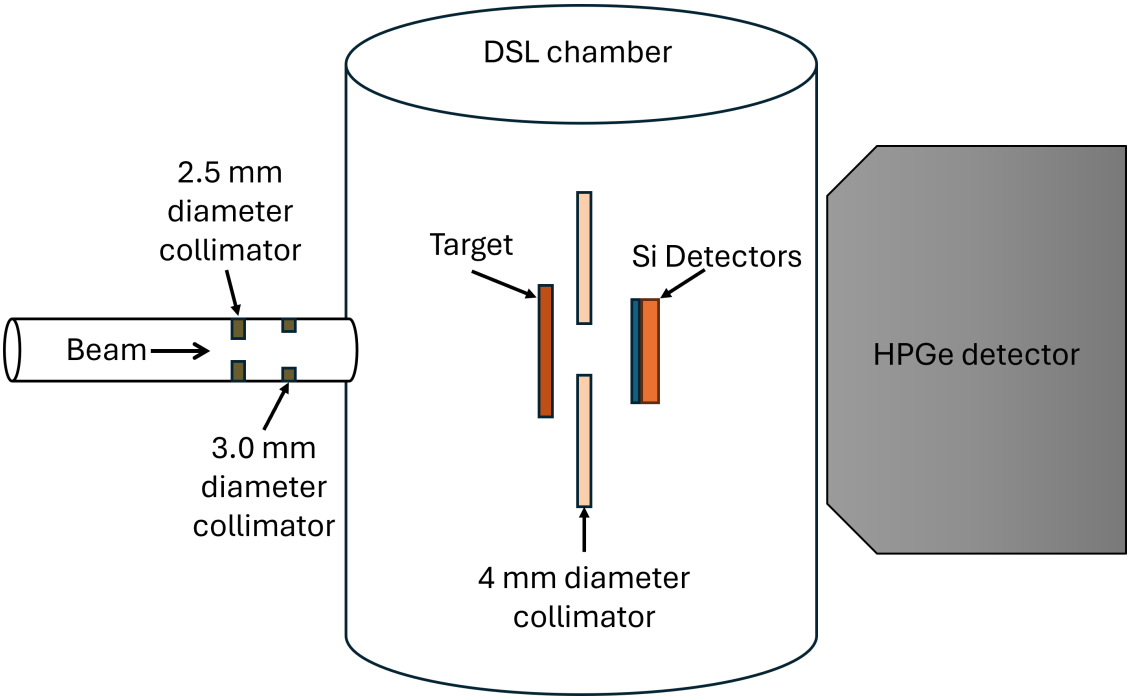

Figure 2.5 Schematic of the DSL1 setup on the beamline (not to scale).

new setup. The main upgrade was to the silicon detector telescope, with necessary changes made to the chamber and electronics to support the new detectors.

The angular coverage of the Si detector telescope was increased by upgrading from 150 mm^2 detectors to 2450 mm^2 detectors manufactured by Micron Semiconductor Ltd. This eliminated the need for the collimator previously placed between the target ladder and the ΔE detector. The ΔE detector was upgraded from a single channel detector to a 16×16 strip double sided Si strip detector. The pixelation produced by the overlapping strips allows for more precise particle location determination. This in turn allows for correction for the lower energy of particles at larger emission angles when setting gates on the charged particles, as well as taking into account the effect of alpha emission angle on the Doppler shift of the associated gamma ray. More information on the use of the pixelation for gating is provided in section 4.6.

The E detector used in DSL2 is a MSX25 type detector and has a thickness of 1000 μm. The ΔE detector used in the experiment this work focuses on is a W1 type detector with a thickness of 75 μm. A second ΔE detector with a thickness of 140 μm is available for use in future DSL2

Date/Time	E Detector Leakage Current (nA)	ΔE Detector Leakage Current (nA)
12/12/22 09:00	47	16
12/13/22 11:00	36	8
12/13/22 17:00	37	7
12/14/22 10:00	36	6
12/14/22 16:00	38	7
12/15/22 10:00	35	6
12/16/22 11:00	37	6
12/17/22 10:00	36	6
12/18/22 13:30	30	5

Table 2.1 Leakage current measured in each Si detector during experiment S2193. The first entry is from shortly before beam was first delivered to the setup. The last entry is from after the end of the experiment but while the setup was still cooled with liquid nitrogen.

experiments. The Si detectors were manufactured with ceramic frames with a lower coefficient of thermal expansion than standard frames used. The Si detectors get radiatively cooled by the cold target ladder. Each strip of the ΔE detector has a width of approximately 3 mm. Both detectors have a dead layer of 500 nm on both the Ohmic and junction sides. The E detector has a recommended bias voltage of 140 V, and the ΔE detector has a recommended bias voltage of 10 V. The leakage currents recorded in the Si detectors just before, during, and just after the first DSL2 experiment are given in Table 2.1. Drawings of the front and back of both Si detectors are shown in Figure 2.6.

The ΔE detector is placed at 18.38 mm downstream from the target ladder. The E detector is at 24.11 mm downstream from the target. Figure 2.7 shows the target ladder and ΔE-E telescope installed on the flange.

A new flange was designed and manufactured for the DSL chamber to support the new ΔE-E Si detector telescope and associated cabling. Figure 2.8 shows a drawing of the new flange, with all of the connections used during the first DSL2 experiment mapped out. The increase in the number of channels of the ΔE detectors from the DSL1 configuration required an additional feedthrough on the flange for that detector. Collimator and target ladder currents were monitored, as well as the target ladder temperature. The shroud temperature was not monitored during this experiment. A support plate for the preamplifiers associated with each detector was also manufactured.

The two collimators that were used in DSL1 placed upstream of the target ladder are still used

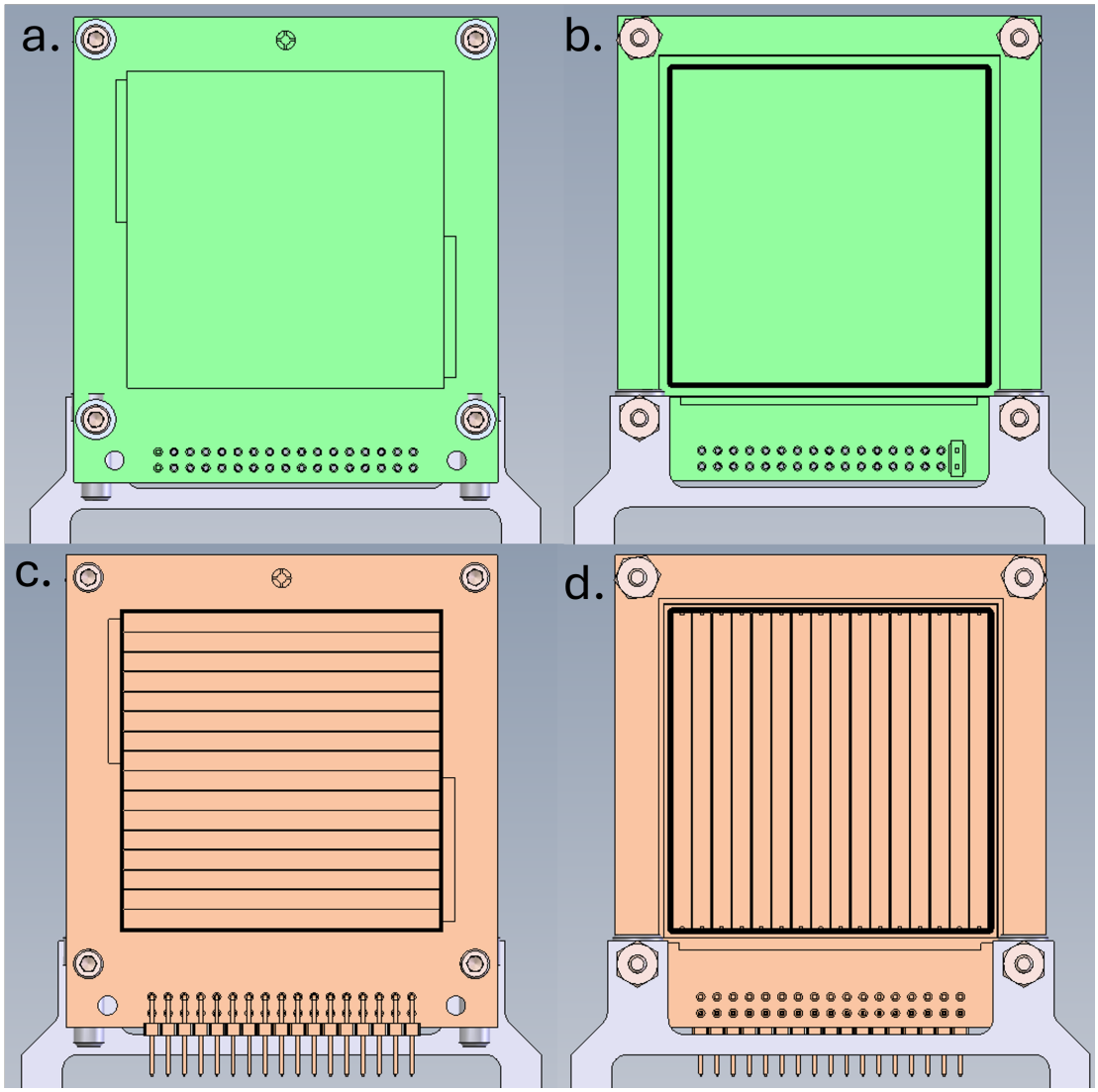

Figure 2.6 a) Drawing of the front of the E detector, as it looks mounted on the chamber flange. b) Drawing of the back of the E detector, mounted. c) Drawing of the front of the ΔE detector, mounted. d) Drawing of the back of the ΔE detector, mounted.

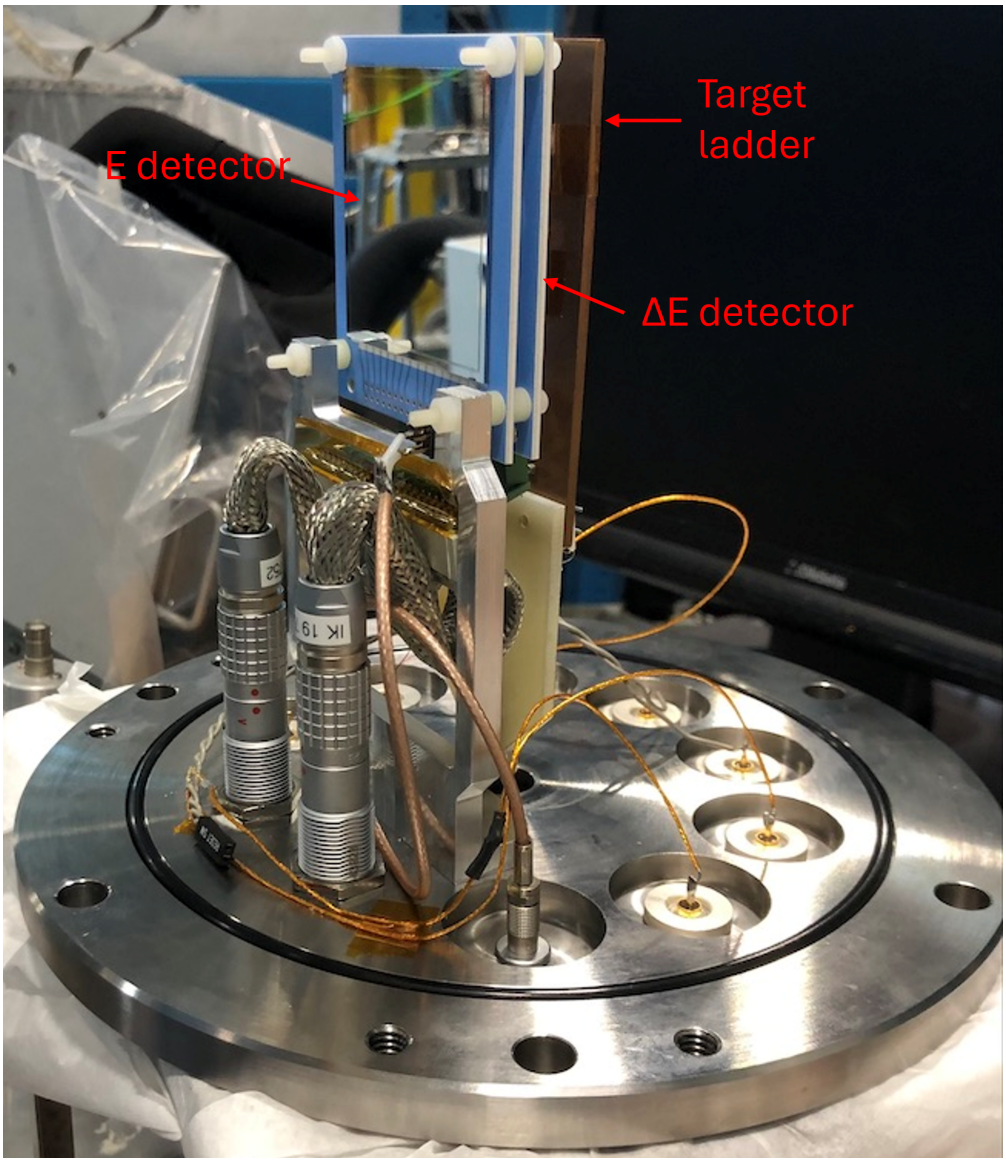

Figure 2.7 View of the Si detector telescope and target ladder installed on the chamber flange. The back of the E detector is most visible.

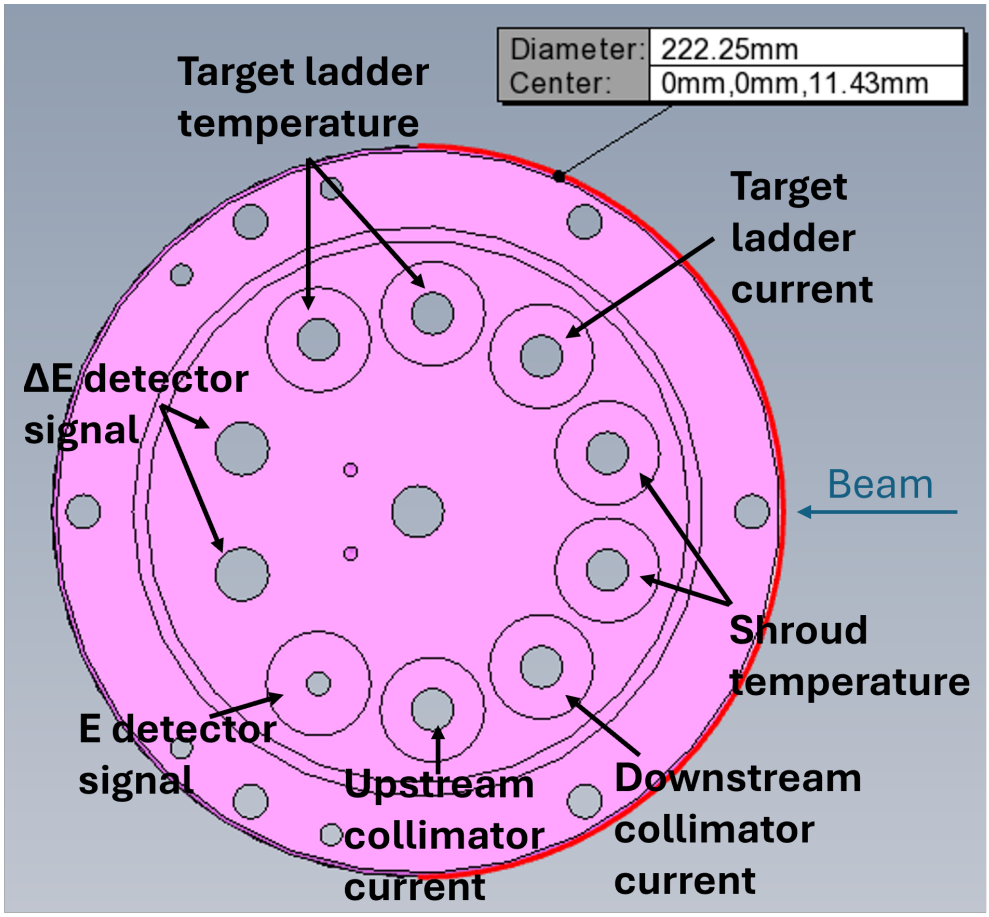

Figure 2.8 Drawing of the inside of the chamber flange manufactured for DSL2 with all of the connections used in the first experiment labeled. View is looking down from above.

in DSL2. They can be seen in Figure 2.9, which also shows the DSL2 flange installed at the bottom of the chamber.

A drawing of the full DSL2 setup and a picture of the full setup on the beamline are shown in Figure 2.10 and Figure 2.11. The first DSL2 experiment used a HPGe clover detector from the Gamma-Ray Infrastructure For Fundamental Investigations of Nuclei (GRIFFIN) array [70]. The HPGe detector was positioned between 0.7 and 0.8 mm away from the outside of the DSL chamber.

The DSL2 setup on the beamline before the HPGe detector was added can be seen in Figure 2.11.

The basic procedure to prepare for a beam-on experiment with the DSL2 setup is as follows:

- Install ΔE-E Si detector telescope and target ladder on flange

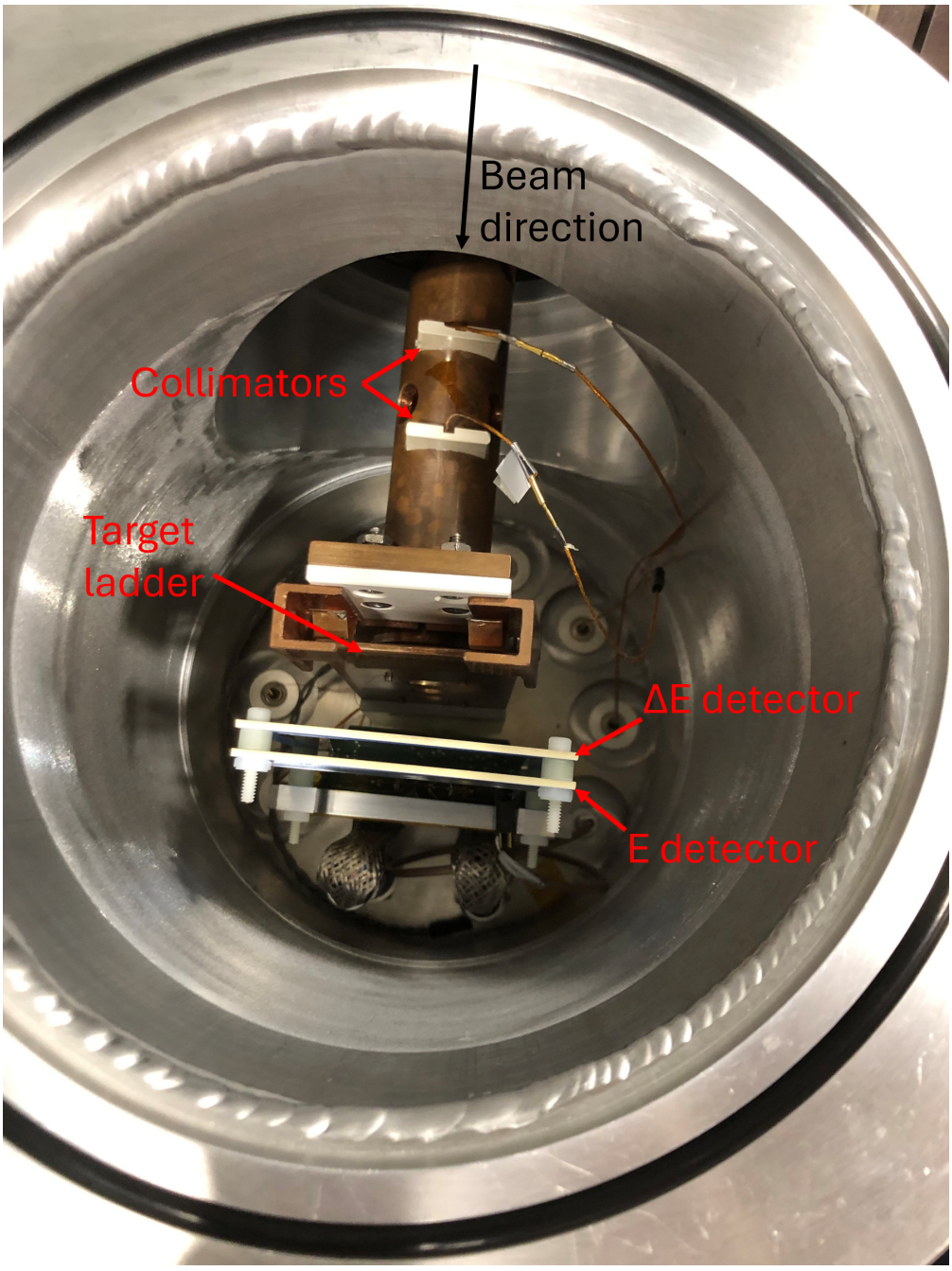

Figure 2.9 View into the DSL chamber from above with the Si detectors installed on the flange and the flange installed on the chamber.

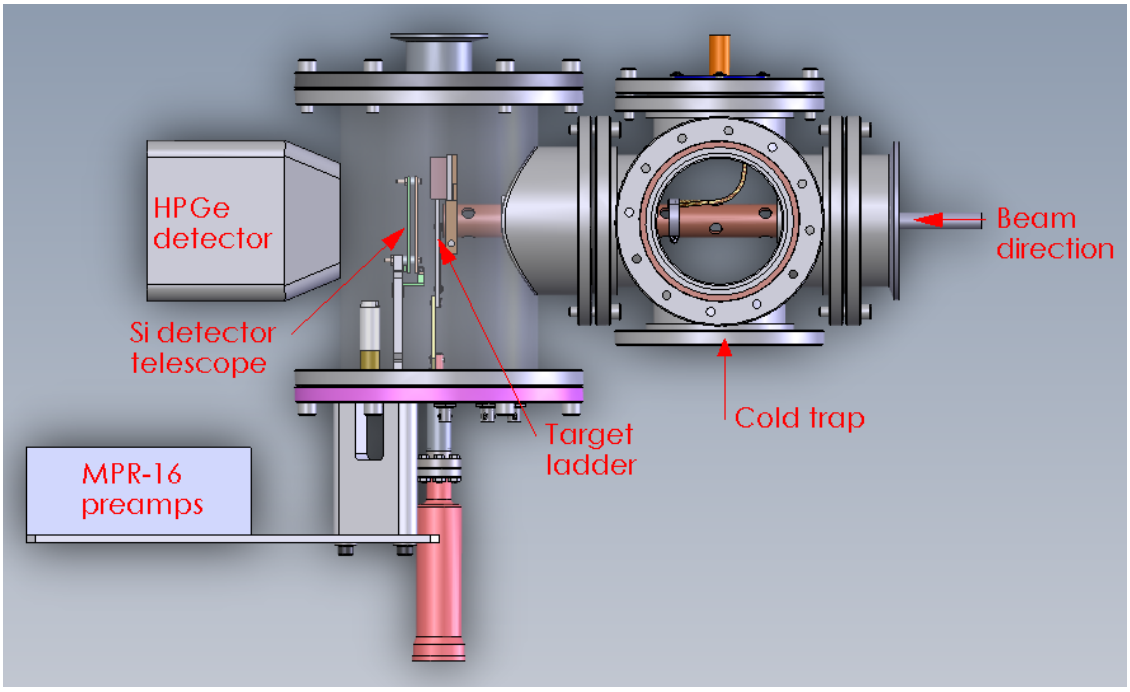

Figure 2.10 Drawing of the full DSL2 setup.

- Connect Si detectors and any other desired readouts to flange feedthroughs
- Install flange carefully in chamber with chamber top off, connecting the preamp support plate during this process
- Connect other readout cables (such as temperature and current monitors) to their sources
- Install upstream collimators
- Connect BeCu cold finger to the target ladder
- Seal chamber top
- Initiate pump down with roughing pump
- Once vacuum has reached a few mTorr activate the turbomolecular pump
- Pump down to the nTorr level
- Fill cold trap L2N dewar

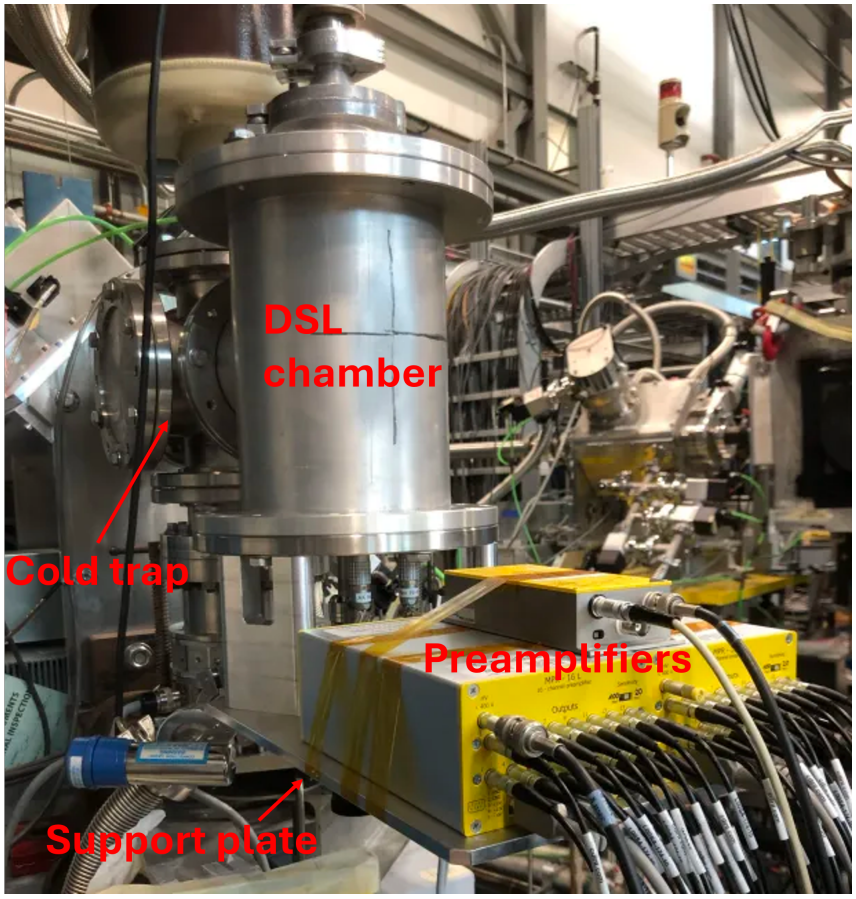

Figure 2.11 The DSL chamber on the beamline, as configured for DSL2.

- Connect preamplifiers to DAQ/HV power supply
- Bias Si detectors
- Arrange the HPGe detector outside the DSL chamber at 0° to the beam direction. Connect to DAQ and power supply, and cryogenically cool
- Take data!

CHAPTER 3

^{24}Mg(^{3}He, α)^{23}Mg EXPERIMENT

The first experiment using DSL2 was proposed in 2021 and approved by the TRIUMF Experiments Evaluation Committee (EEC) in the beginning of 2022. This experiment, experiment S2193, ran at the end of 2022. It serves as the main experiment for this thesis.

3.1 Targets

Four ^{3}He-implanted Au foil targets were produced for the experiment. One was produced at Lawrence Livermore National Laboratory (LLNL) by John Wilkinson and Nicholas Esker, and three were produced at TRIUMF by Barry Davids. Both sets of targets used gold foils that were 0.025 mm thick with a tolerance of ± 15% and had a purity of 99.99+%.

3.1.1 LLNL Target

The target produced at LLNL was implanted using the negative ion source at the Center for Accelerator Mass Spectrometry. The implantation area was approximately 1 cm × 0.75 cm. The ^{3}He deposition was performed at 30 keV, with a resulting integrated dose of 3.8×10^{17} atoms and implantation concentration of 5.11×10^{17} ions/cm^2 in the implanted region. The implanted region on this target is marked by a visible brownish spot, indicating some level of contamination.

3.1.2 TRIUMF Targets

The targets produced at TRIUMF were implanted using a 30 keV, 3.2 μA beam. The ^{3}He was delivered in the +2 charge state.

Three overlapping implantation spots were made on each target to extend the densest region of implanted ^{3}He, while keeping all regions under the helium blistering threshold of approximately 6×10^{17} ions/cm^2 [71], under the assumption that the beam distribution was normal with the densest region in the center. Each spot was 2.7 mm apart, as this was determined to be the maximum distance between spots that wouldn't result in regions of lower ^{3}He density between each spot. Figure 3.1 shows the simulated distribution of ^{3}He on each target. According to the current on the target ladder during implantation, each spot received an integrated current of 4.25 μAh, though the current on the target ladder was not suppressed, so the current readings were not completely

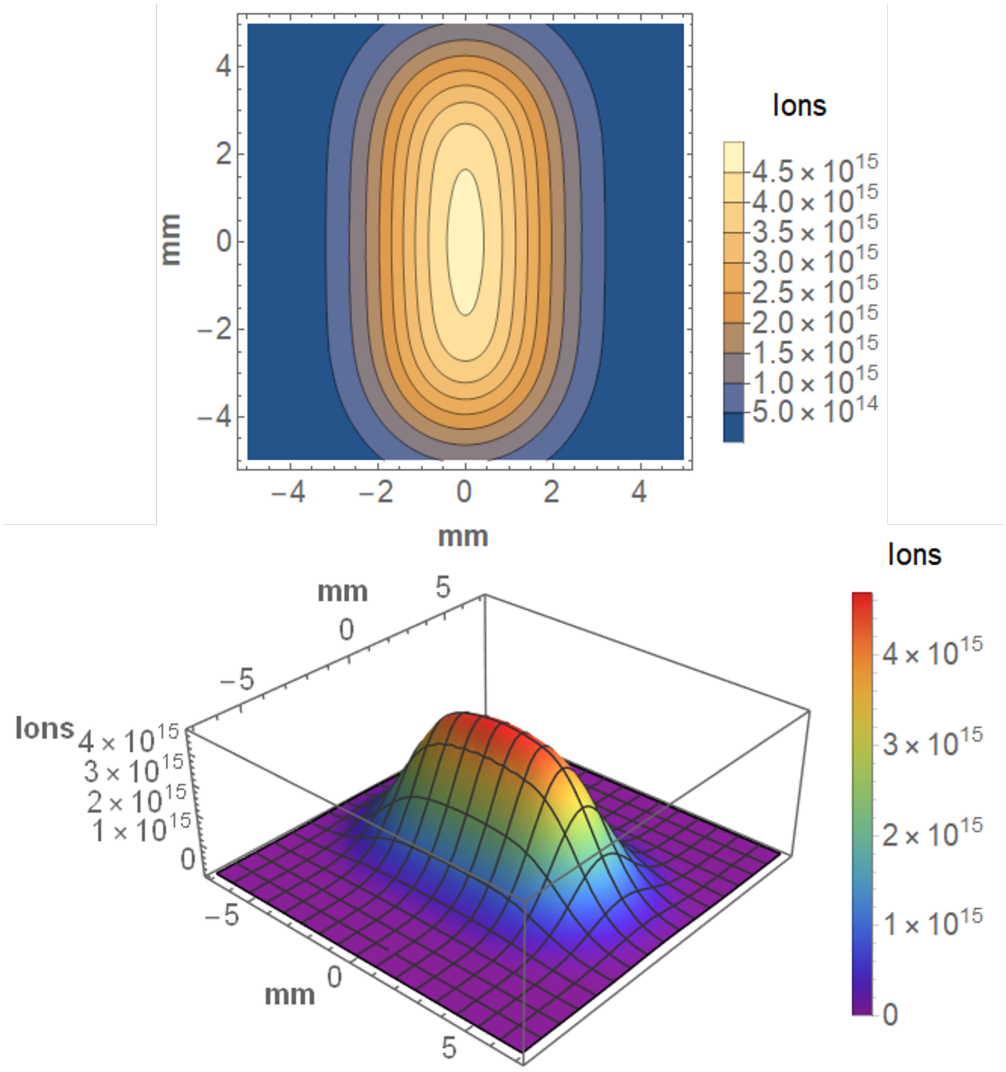

Figure 3.1 Top: 2D distribution of ^{3}He in one target produced by three overlapping implantation spots. Bottom: 3D representation of the same distribution.

accurate.

The targets were implanted while mounted in the target ladder in the DSL chamber. The ^{3}He beam was intended to impinge upon the horizontal center of each Au foil, but due to uncertainty in the beam alignment, the implanted region ended up being split between the target ladder and target foil on the downstream left side of each target. The darkened regions on the copper top plate of the target ladder in Figure 3.2 shows the shape, size, and positioning of the implanted region for each target.

The topmost target in the target ladder was replaced by the LLNL target for the experiment. At

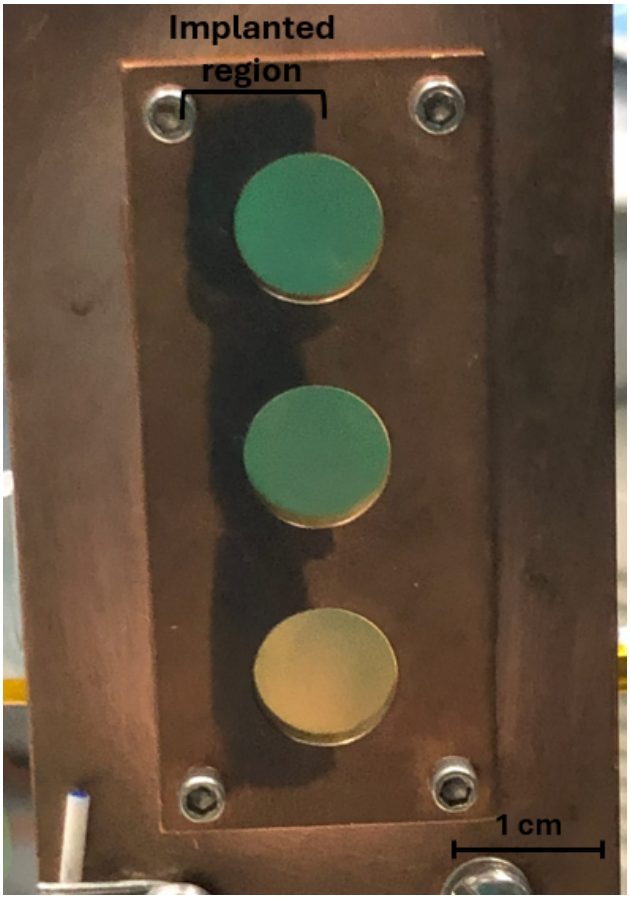

Figure 3.2 The targets produced at TRIUMF on the target ladder.

the time of the target switch, the two remaining TRIUMF targets were moved so the densest region of ^{3}He would be as close to the center of the window on the target ladder for each target as possible, while also trying to prevent the ^{24}Mg beam during the experiment from impinging upon a region with no ^{3}He, since the partial implantation into the target ladder caused a sharp cutoff in ^{3}He on the downstream left side of the target. It was also vital that the targets be arranged so the Au foil still filled the whole aperture to prevent beam from impinging directly on the Si detectors. The target ladder configuration used during the experiment is shown in Figure 3.3.

Only the LLNL target and the TRIUMF target in the middle target ladder aperture were used during the experiment. Data was taken on the LLNL target from the beginning of the experiment to approximately halfway through the originally scheduled shifts, and the TRIUMF target was used from then until the end of the experiment.

Figure 3.3 The targets on the target ladder in the configuration used in the experiment. The topmost target was produced at LLNL, and the lower two targets were produced at TRIUMF. The top two targets were used during the experiment.

3.2 Electronics

Three preamplifiers were used to supply power to the Si detectors, as well as connect the detectors to the data acquisition (DAQ) system. A single channel Mesytec MPR-1 preamplifier was used for the E detector, and two 16-channel Mesytec MPR-16 preamplifiers were used for the ΔE detector, with one preamplifier dedicated to the 16 horizontal strips of the detector and one dedicated to the 16 vertical strips.

The electronics used with the GRIFFIN HPGe detector are able to handle data throughput up to 50 kHz per crystal. Three GRIF-16 digitizers were used to read in the data from the silicon and germanium detectors. GRIF-16s are 16-channel, 14-bit analogue-to-digital converter (ADC) modules with a sampling rate of 100 MHz [72]. Initially, one GRIF-16 was dedicated to each 16-channel preamplifier, and the third GRIF-16 was used for the E detector and four clovers of the germanium detector, though two ΔE silicon strip channels were moved to the third GRIF-16 early in the experiment due to frequent malfunctioning of their original GRIF-16 channels.

The data collected by the GRIF-16s were stored using the Maximum Integrated Data Acquisition System (MIDAS) developed by the Paul Scherrer Institute (PSI) and TRIUMF [73]. The data were then sorted using GRSIsort, which was developed by the GRIFFIN collaboration at TRIUMF.

A diagram of the electronics setup for this experiment is shown in Figure 3.4.

3.3 Beam

A stable ^{24}Mg beam was produced using the Offline Ion Source (OLIS) at TRIUMF-ISAC. OLIS has four ion sources that can be used to ionize atoms for acceleration [74], with the Multi-charge Ion Source (MCIS) being used for this beam. Shavings of Mg metal were used in MCIS, initially with no support gas. The ^{24}Mg was ionized to the +5 charge state, resulting in a mass-over-charge ratio (A/q) of 4.8.

The first accelerator in the ISAC I experimental hall is an 8 m, 35 MHz Radio Frequency Quadrupole (RFQ). Ions from OLIS are injected into the RFQ where they are accelerated and bunched. The RFQ can accelerate ions from about 2 keV/u to 150 keV/u [75], and can provide between 85 and 170 ns separation between bunches [76].

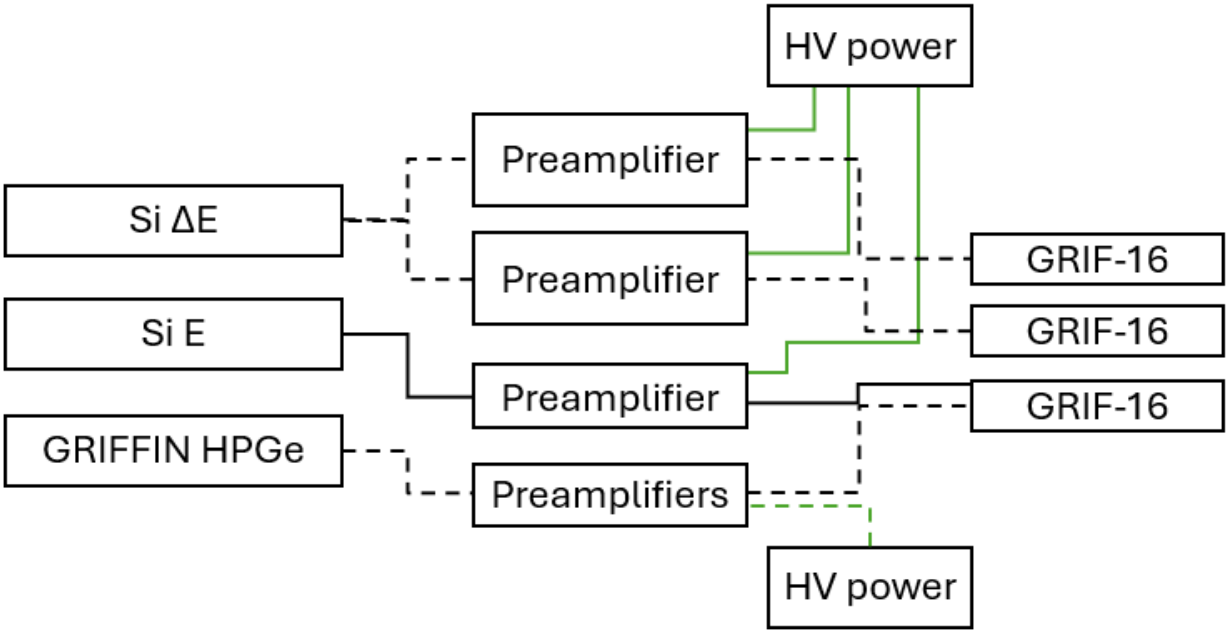

Figure 3.4 Block diagram of the electronics used for data acquisition in this experiment. Power supply is represented by green lines. A dashed line indicates multiple connections.

The secondary accelerator of ISAC I is a 5.6 m, 105 MHz drift tube linac (DTL). The DTL requires the A/q of the beam to be between 3 and 6. Because MCIS is able to provide a A/q value of 4.8 for the ^{24}Mg beam, the foil for charge stripping between the RFQ and DTL was not required [77]. The DTL is used to accelerate the beam from about 150 keV/u to 1.5 MeV/u [76].

For experiments in the ISAC II facility such as this one, a superconducting linac is then used to accelerate ions to a maximum energy of 7.5 MeV/u, for A/q = 5 [78].

A diagram of the TRIUMF-ISAC facility is shown in Figure 3.5.

Prior to delivery to the experimental setup, the beam energy was measured to be 75.005 ± 0.045 MeV. On December 12th, 2022, approximately 1 enA of beam was delivered to the DSL2 chamber, beginning TRIUMF experiment S2193. Figure 3.6 shows the DSL setup on the beamline during the experiment. The next few hours were used to optimize the configuration and settings of the DAQ. Later in the day, the current was increased from 1 enA to 5 enA, and shortly after increased to 10 enA.

Early on December 13th, the beam current started to become intermittent and fall below the

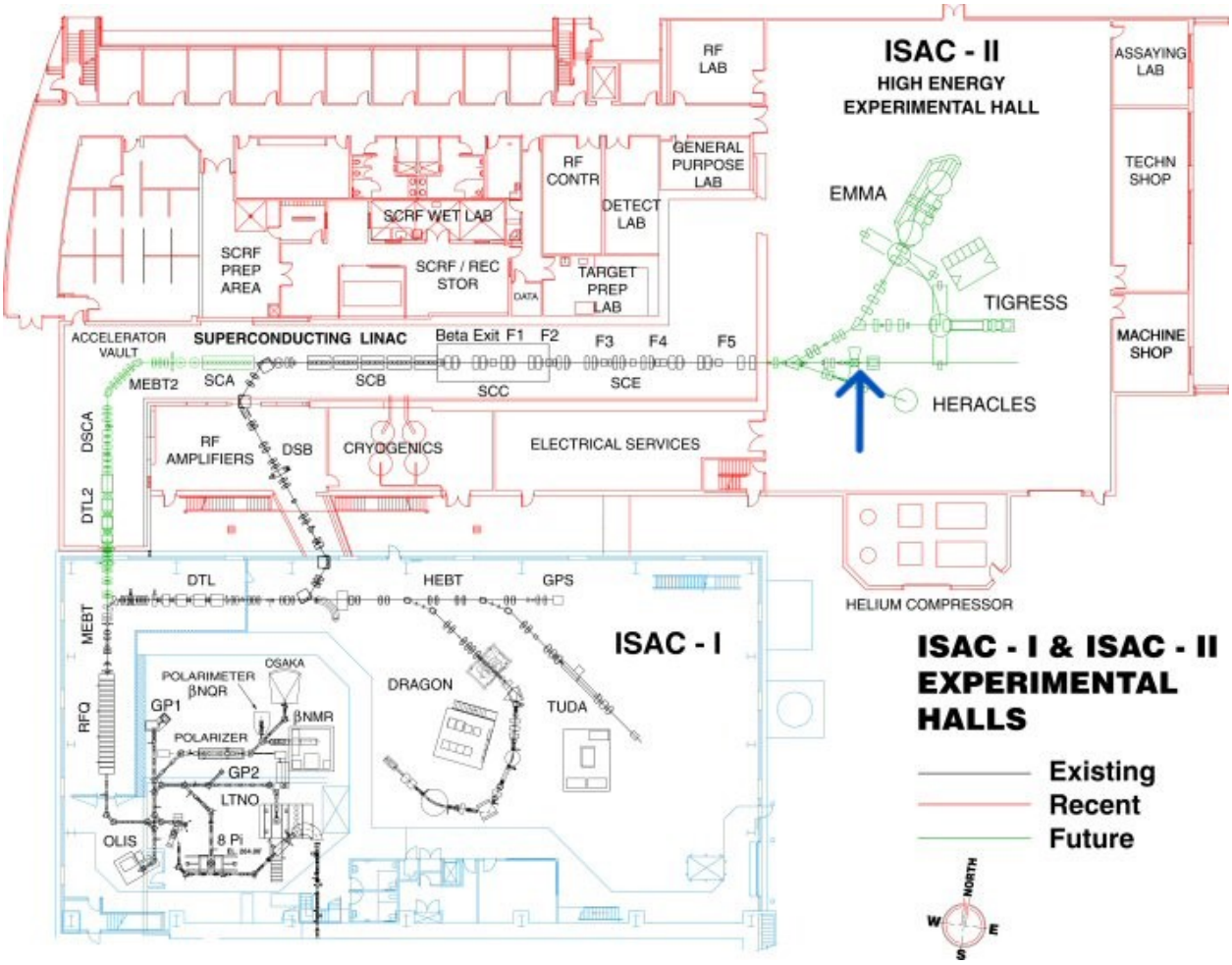

Figure 3.5 Floor plan of the TRIUMF-ISAC facility [79]. The blue arrow indicates the location of the DSL2 setup.

minimum approved current for the experiment of 5 enA. Several attempts were made to recover the beam over the course of the next few days. During attempts to increase the output beam current from MCIS on December 14th, the use of oxygen as a support gas was tested. This initially allowed the plasma in MCIS to ignite well and provided beam currents around the requested 15 enA to the experimental setup for several hours, though the current ultimately remained unstable. On December 17th, delivery of the beam to the experimental setup was paused for additional tuning attempts, and was not recovered. The experiment was ended early, with the plan of finishing the remaining shifts once more beam development had occurred.

The experiment was approved for 24 shifts of at least 5 enA of ^{24}Mg beam. After the experiment,

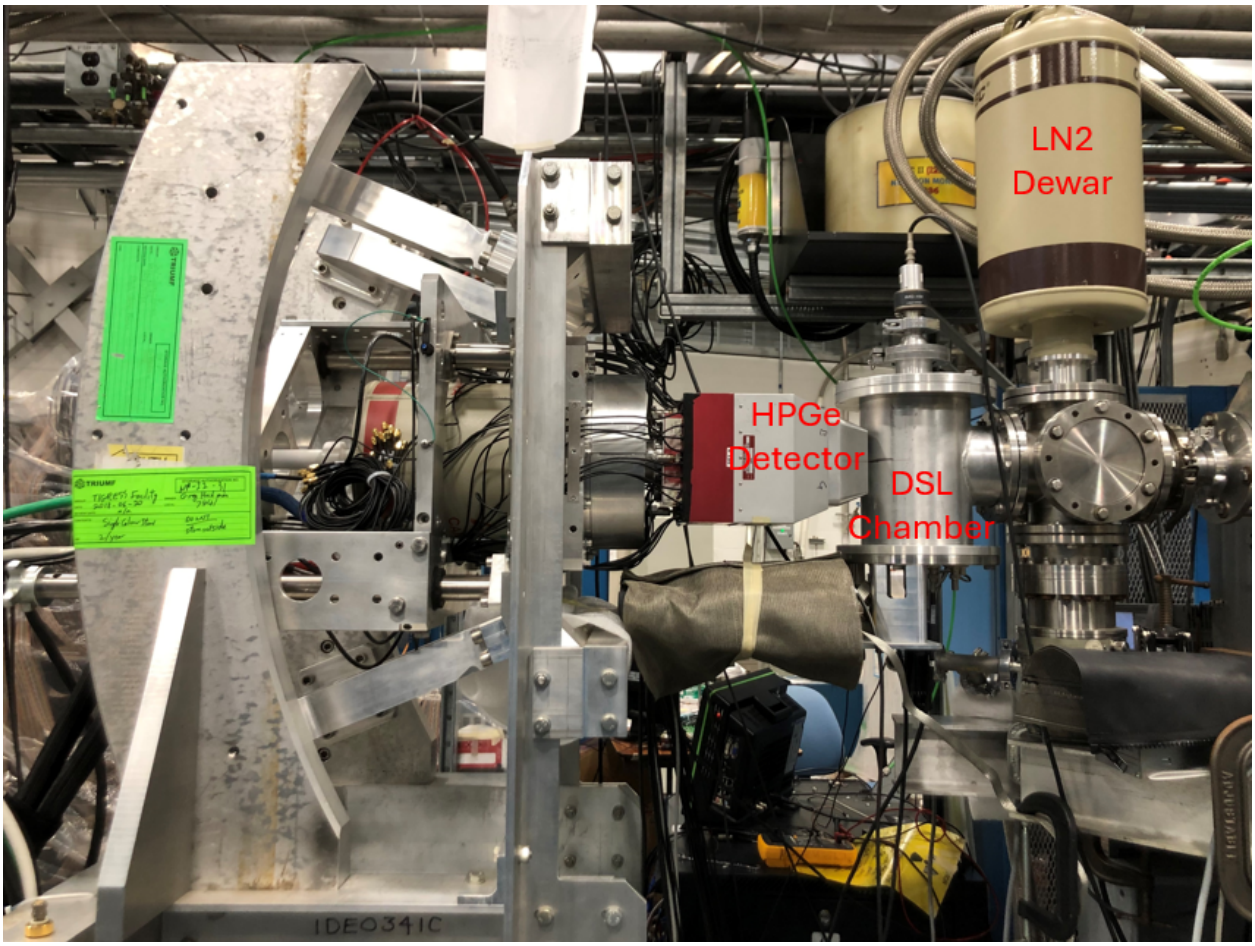

Figure 3.6 DSL setup on the beamline during experiment S2193. Beam direction is right to left.

the official tally of shifts during which at least 5 enA of beam could have been delivered was 10. The beam current during the experiment was integrated to determine the amount of ^{24}Mg incident on the target was 2.49×10^{15} ions. A plot of the beam current on target throughout the entire experiment is shown in Figure 3.7.

When the ^{24}Mg beam was first put on target, the pressure in the DSL chamber was 11 nTorr. The temperature on the target ladder recorded during the experiment is shown in Figure 3.8.

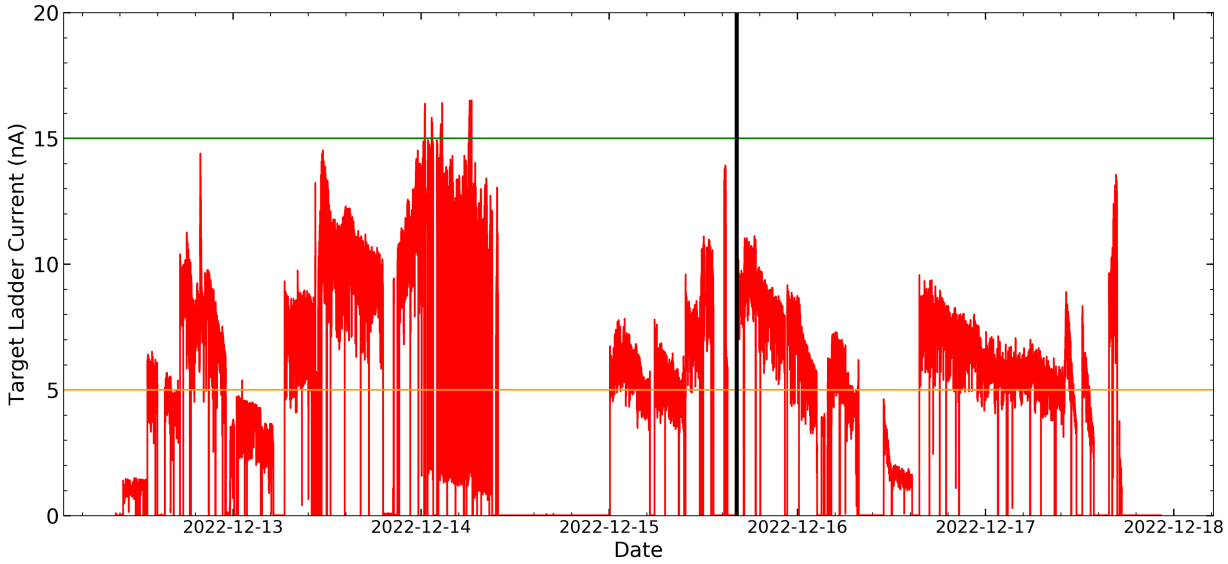

Figure 3.7 Beam current on the target ladder during experiment S2193. The green line indicates the requested 15 enA beam current, and the orange line indicates the minimum approved beam current of 5 enA. The vertical black line indicates when the switch was made from taking data on the LLNL target to taking data on the TRIUMF target.

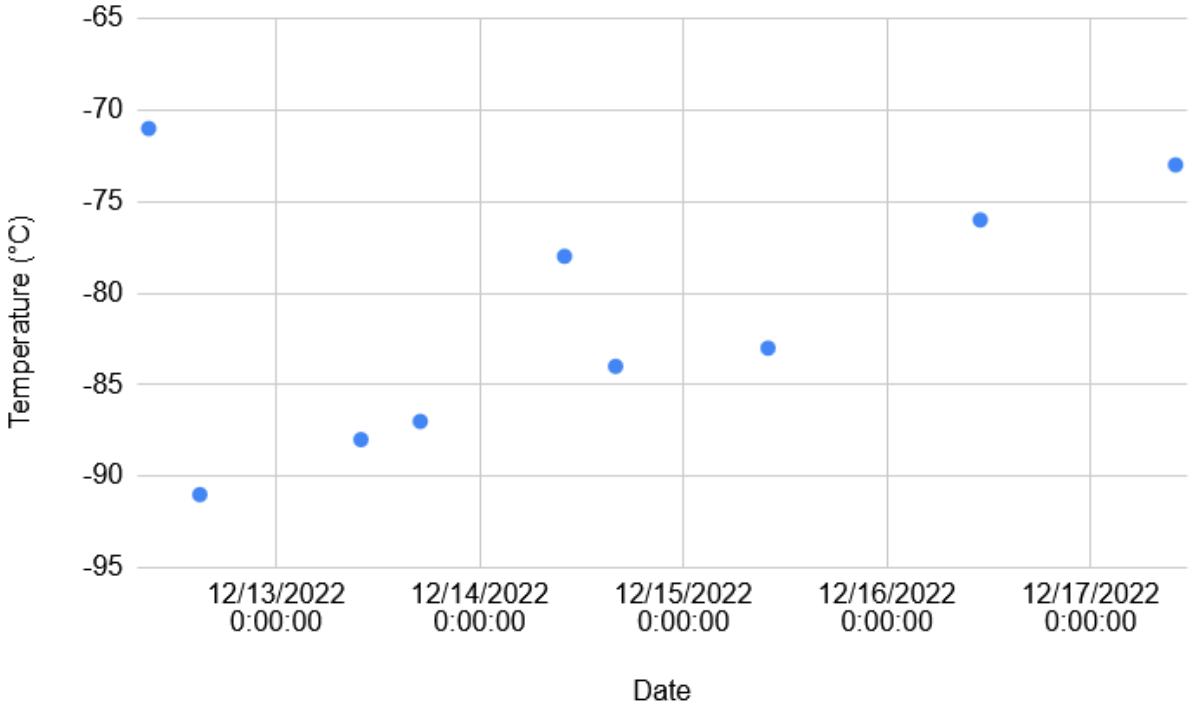

Figure 3.8 Target ladder temperature readings taken during the experiment.

CHAPTER 4

^{24}Mg(^{3}He, α)^{23}Mg EXPERIMENT ANALYSIS METHODS

This chapter outlines the analysis procedure for the first dataset taken with the DSL2 setup.

4.1 Calibration

The analysis process began with calibration of the data taken with all detectors.

4.1.1 Si Detectors

Two triple alpha sources were used to calibrate the Si detectors. A calibration run was taken both before and after the beam time of the experiment. The ΔE detector was calibrated using a triple alpha source containing ^{239}Pu, ^{241}Am, and ^{244}Cm, and the E detector was calibrated using a triple alpha source containing ^{148}Gd, ^{230}Th, and ^{244}Cm. The ^{239}Pu/^{241}Am/^{244}Cm source was secured to the downstream side of the target ladder, and the ^{148}Gd/^{230}Th/^{244}Cm source was secured to the downstream inside wall of the DSL chamber, aligned with the center of the E detector.

During the post-experiment calibration run, the ^{239}Pu/^{241}Am/^{244}Cm source was secured to the target ladder in such a way that it was not perfectly parallel to the ΔE detector, though it was still centered relative to the detector, which resulted in the lower edge of the source holder shielding the lowest horizontal strips of the ΔE detector from the α particles. This clearly demonstrated which set of strips of the ΔE detector was the horizontal strips and which was the vertical strips, and also indicated which of the horizontal strips was at the bottom of the detector.

The strips of the ΔE detector are named such that strips 1-16 indicate the 16 horizontal strips of the detector, where strip 1 is the topmost strip and strip 16 is the bottommost strip, and strips 17-32 indicate the 16 vertical strips of the detector. Which strip is the leftmost and which is the rightmost of the vertical strips has yet to be determined. There are only two feedthroughs that connect the preamplifiers to the ΔE detectors. It is known which one corresponds to the horizontal strips and which corresponds to the vertical strips, but this makes it difficult to determine the orientation of the vertical strips. This could be determined by close investigation of the feedthrough for the vertical strips, and confirmed by shielding the left or right side of a source and observing which strips detect fewer particles. During the pre-experiment calibration run, strips 12 and 32 were reading

Isotope	α **Energy** (keV)	**Intensity** (%)
^{239}Pu [80]	5105.5(8)	11.94(7)
	5144.3(8)	17.11(14)
	5156.59(14)	70.77(14)
^{241}Am [81]	5442.80(13)	13.1(3)
	5485.56(12)	84.8(5)
^{244}Cm [82]	5762.64(3)	23.10(10)
	5804.77(5)	76.90(10)
^{148}Gd [83]	3182.690(24)	100
^{230}Th [84]	4620.5(15)	23.40(10)
	4687.0(15)	76.3(3)

Table 4.1 α particle energies and relative intensities for each isotope used for Si detector calibration for this experiment.

into faulty GRIF-16 channels. This was fixed in the early stages of the experiment, but there was no data for these channels during the pre-experiment calibration run. There is no data for strip 16 during the post-experiment calibration run due to the aforementioned shadow from the source holder.

All of the isotopes in the triple alpha sources except ^{148}Gd produce at least two strong α peaks less than 100 keV apart. Table 4.1 lists the strongest peaks associated with each isotope.

An exponentially modified Gaussian (EMG) function of the form

$$f(x;N,\mu,\sigma,\tau) = \frac{N}{2\tau}\exp\left[\frac{1}{2}\left(\frac{\sigma}{\tau}\right)^2 + \frac{x-\mu}{\tau}\right] \times \operatorname{erfc}\left[\frac{1}{\sqrt{2}}\left(\frac{\sigma}{\tau} + \frac{x-\mu}{\sigma}\right)\right] \tag{4.1}$$

where N is the area under the curve, μ is the mean, σ is the width, and τ is the exponential decay constant, was fit to each peak in each strip for both calibration runs. For the isotopes with multiple overlapping peaks, the appropriate number of EMGs were summed, with the assumption that σ and τ, which depend on the response of the detector, were the same for each of the summed peaks due to the closeness in energy of the peaks. One value for N was used for each set of summed peaks, with each peak's contribution scaled by the relative intensity of that peak. A flat linear background was added to the fit. Figure 4.1 shows a sample fit for the ^{239}Pu peak.

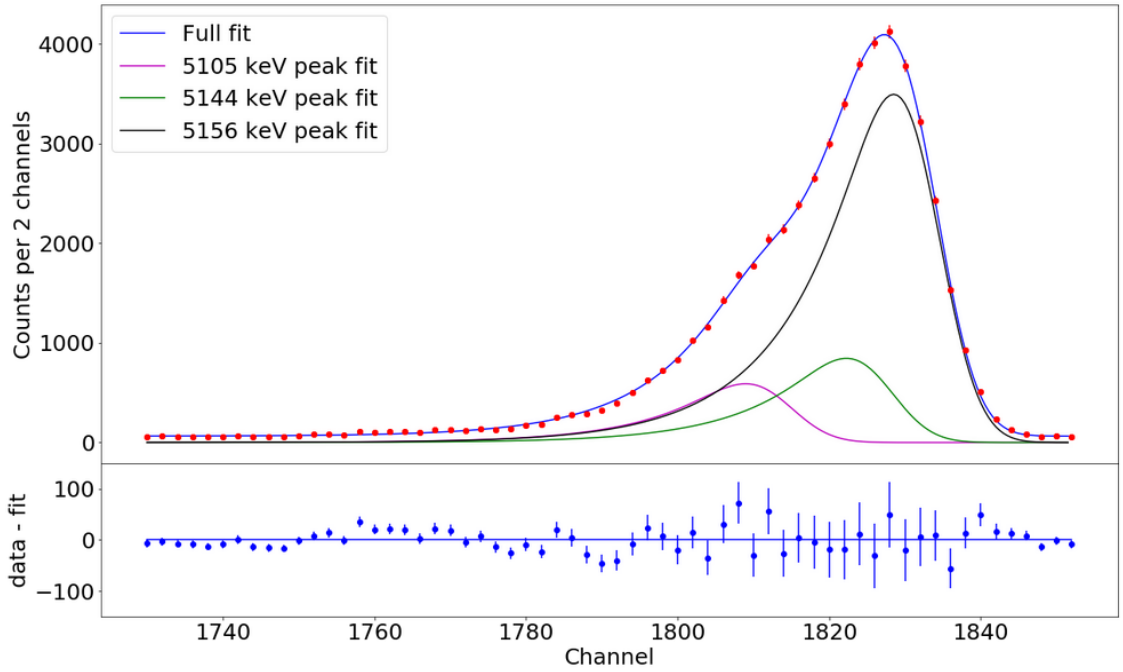

Figure 4.1 Fit of the three ^{239}Pu peaks from the post-experiment calibration run in strip 9, which is a horizontal center strip.

The percent difference in channel location of the maximum of the stronger ^{244}Cm peak for each strip between the pre- and post-experiment runs is shown in Figure 4.2. Data for strips 12, 16, and 32 are missing due to the aforementioned lack of data in one of the calibration runs for each of these strips.

The relatively large differences observed in the vertical edge strips between runs is caused by a loss of resolution in these strips observed after the experiment. Figure 4.3 shows a comparison of the triple alpha spectra from the pre- and post-experiment calibration runs for a vertical edge strip. It should be noted that the post-experiment calibration run did last longer than the pre-experiment calibration run, so it does have higher statistics.

No spikes in temperature were recorded during the experiment, so it is unknown if a sharp change in temperature or excessive cold caused the loss in resolution. The leakage current of the ΔE detector is read out as a single value, instead of on a strip-by-strip basis. There were no recorded increases in the ΔE detector leakage current, though this provides little information about individual strips. Since specific features that could be used to check the calibration during individual runs

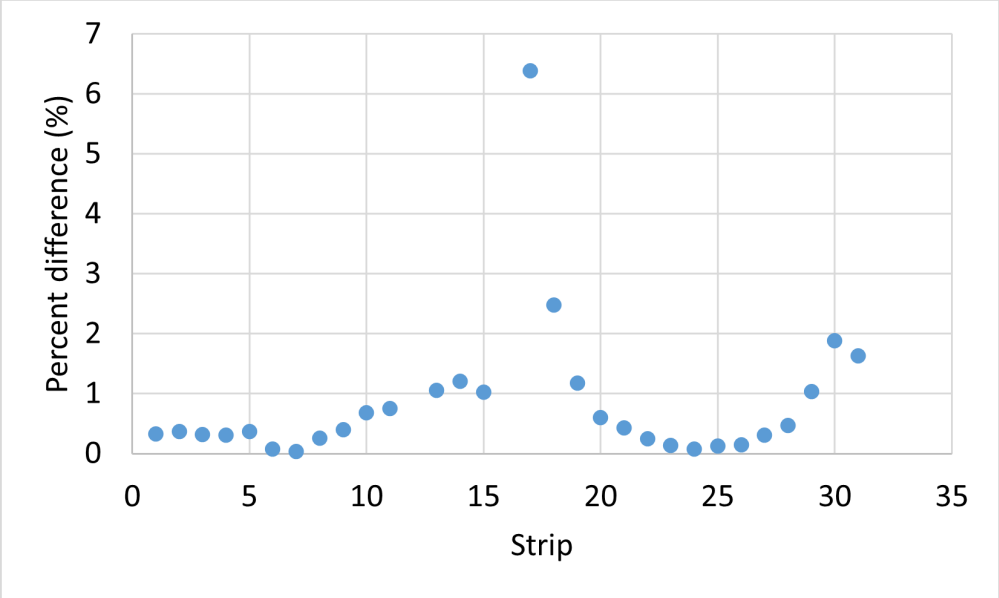

Figure 4.2 Percent difference in the location of the maximum of the higher energy peak from ^{244}Cm between the pre- and post-experiment calibration runs.

were not present in the spectrum, as can be seen in Figure 4.4, the cause of this apparent resolution loss was investigated in other ways. The mean of the entries in each strip was plotted for several edge and center strips for each run of the experiment, shown in Figure 4.5. This was done to look for changes in the spectra of the edge strips not seen in the center strips that could indicate a damaging event. The general step down in the means in each strip at the target switch is believed to be caused by the increased contamination of the target produced at LLNL. The mean of the entries is taken for all charged particles detected in a strip during a run, and increased contamination leads to more fusion evaporation reactions producing more higher energy light particles.

As of now, the cause of the resolution loss of the vertical edge strips remains unknown, though it does not appear that any specific detector-damaging incident occurred during the experiment. It is unlikely that the resolution loss is caused by radiation damage to the strips, since the edge strips had the lowest event rates. No data has been taken with the detector since the post-experiment calibration run, so it is unknown if the detector is still exhibiting this apparent resolution loss. The post-experiment resolutions of the E detector and the strips of the ΔE detector at the highest source energy are given in Table 4.2.

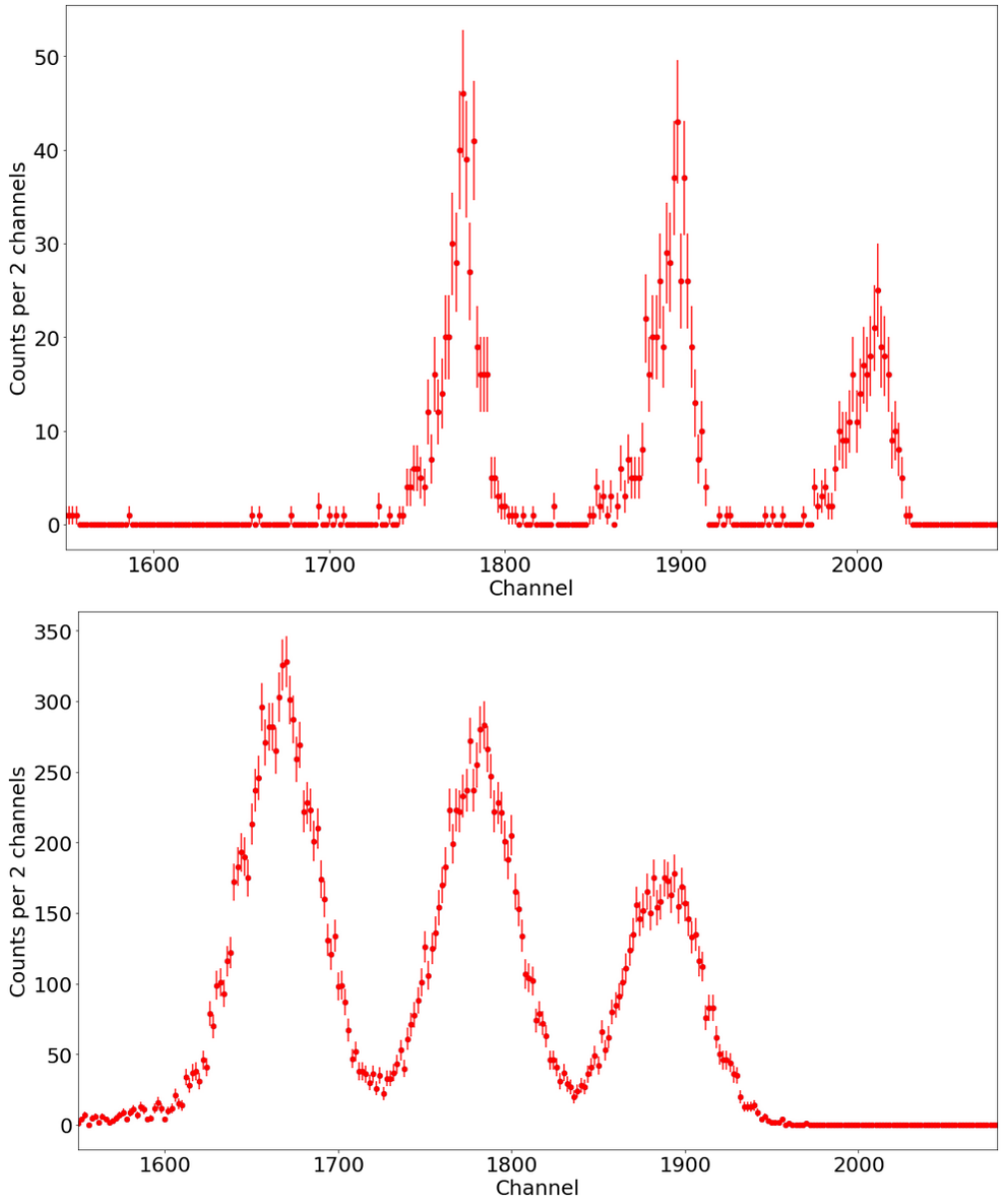

Figure 4.3 Uncalibrated triple alpha spectrum from the pre-experiment calibration run (top) and post-experiment calibration run (bottom) in vertical edge strip 17.

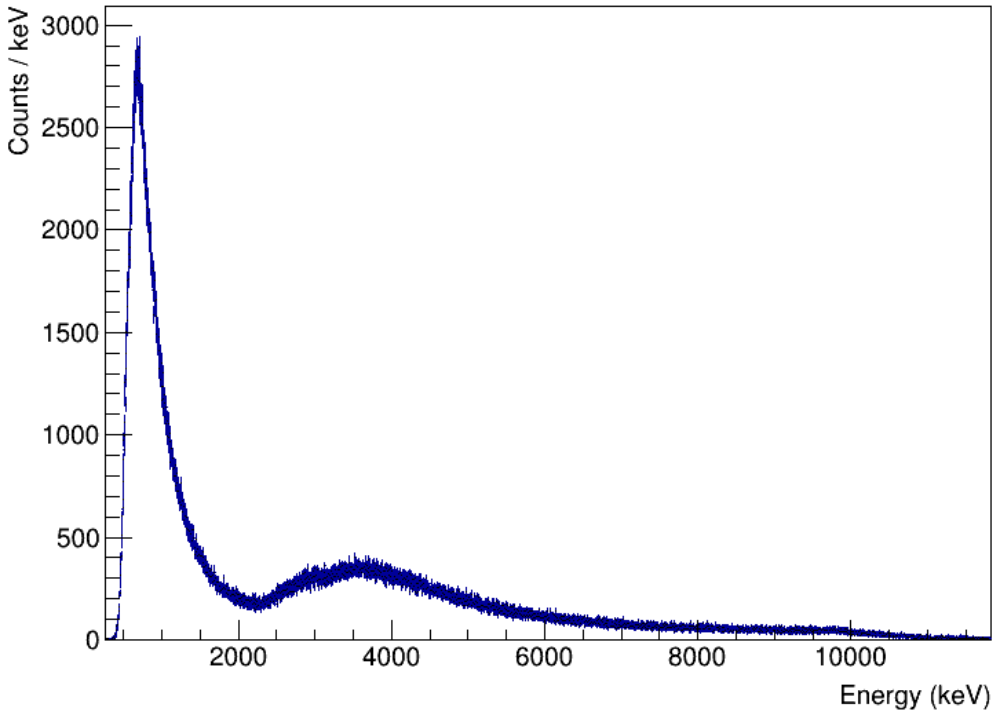

Figure 4.4 Charged particle energy spectrum in a single center strip of the ΔE detector during a 1 hour run on the target produced at LLNL.

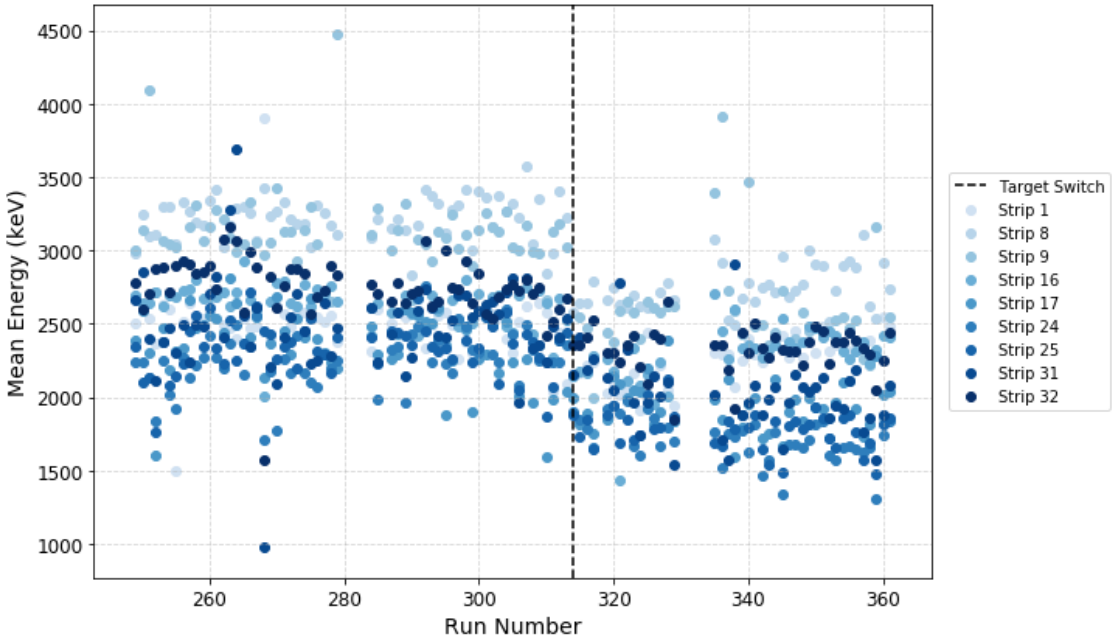

Figure 4.5 The mean energy of all entries per run in several strips of the ΔE detector. Strips 1 and 16 are horizontal edge strips, strips 8 and 9 are horizontal center strips, strips 17 and 32 are vertical edge strips, and strips 24 and 25 are vertical center strips.

Detector	Resolution (FWHM) (%)
E detector	1.25
Strip 1	0.90
Strip 2	0.88
Strip 3	0.81
Strip 4	0.79
Strip 5	0.75
Strip 6	0.75
Strip 7	0.75
Strip 8	0.78
Strip 9	0.81
Strip 10	0.84
Strip 11	0.86
Strip 12	0.86
Strip 13	0.89
Strip 14	0.79
Strip 15	0.51
Strip 16	N/A
Strip 17	2.59
Strip 18	1.72
Strip 19	1.26
Strip 20	1.05
Strip 21	0.93
Strip 22	0.80
Strip 23	0.75
Strip 24	0.76
Strip 25	0.76
Strip 26	0.79
Strip 27	0.87
Strip 28	1.03
Strip 29	1.18
Strip 30	1.74
Strip 31	2.24
Strip 32	3.01

Table 4.2 Post-experiment resolution in the E detector and each strip of the ΔE Si detector at 5.8 MeV.

A linear fit of the channel locations of the maxima of the strongest α peak for each isotope and the known energies of those α particles was produced for each strip, using the post-experiment calibration run. The statistics were much higher in the post-experiment calibration run, and fewer channels were missing, which makes it the more favorable option. It is unknown when the loss of resolution in the small number of vertical edge strips occurred, but the difference between the peak maxima pre- and post-experiment even in these strips is minimal. Additionally, the pixels composed from edge strips are rarely used in the analysis presented in the rest of this work due to the lower statistics at broader angles. Strip 16, which did not have post-experiment calibration data, referred to the pre-experiment calibration run.

4.1.2 HPGe Detectors

Before the beam was delivered to the experimental setup, a ^{56}Co gamma source was used to calibrate the HPGe detectors. This calibration was used for preliminary online analysis during the experiment.

After the end of beam delivery to the experimental setup, a ^{56}Co source, a ^{60}Co source, a ^{152}Eu source, and a ^{244}Cm/^{13}C source were used for a post-experiment calibration of the HPGe detectors. The ^{244}Cm/^{13}C source produces 6128.63(4) keV gamma rays [85] via the ^{13}C(α,$n\gamma$)^{16}O reaction. This calibration allowed for preliminary analysis and peak identification after the experiment, though it was discovered that the calibration using these source runs was poor at high energies, as can be seen in Figure 4.6. The HPGe clover was moved away from the DSL chamber after the experiment for the ^{244}Cm/^{13}C calibration run so the source could be centered with respect to the Ge crystals. It is possible that this change caused a shift in the calibration.

The initial post-experiment calibration allowed for identification of several gamma rays from states that are long-lived enough to not exhibit a Doppler shift, referred to as stopped lines, in the experimental spectrum. These stopped lines were used in a second and successful attempt to calibrate the experimental data. An EMG function was fit to each of these peaks, and the channel locations of the maxima of the peaks were used for the calibration. Table 4.3 shows the peaks used.

The calibration using the stopped peaks improved the calibration at high energies, as can be

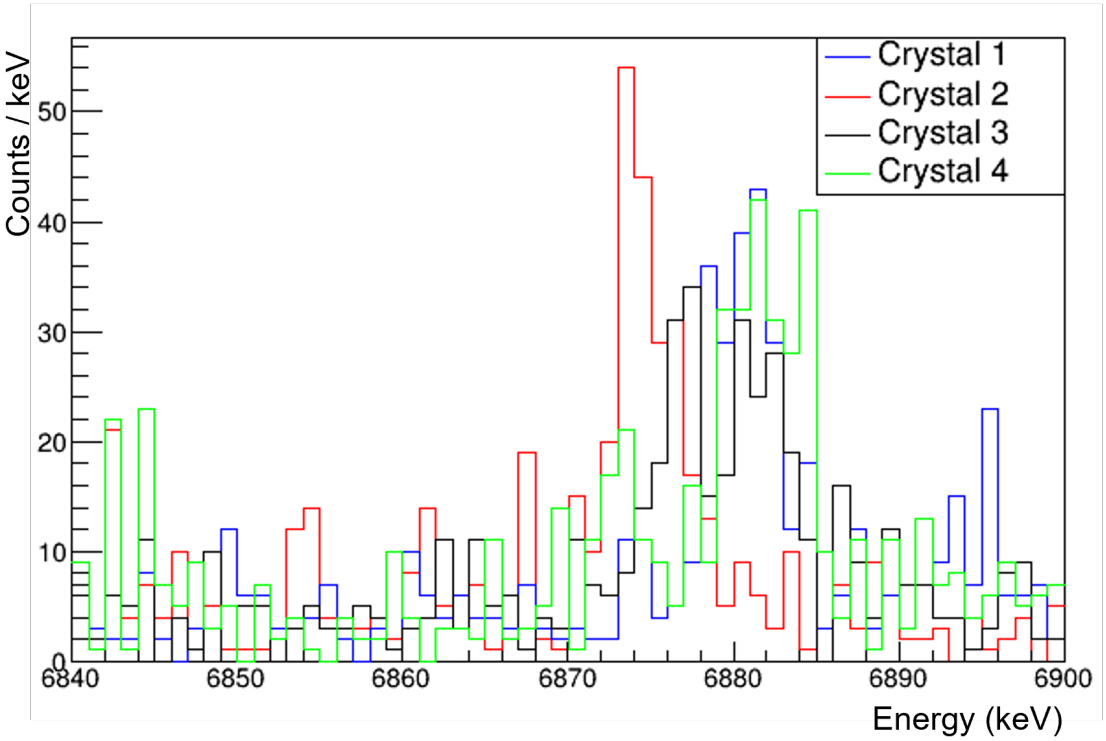

Figure 4.6 The gamma spectrum from each crystal for the 6.88 MeV gamma ray from ^{28}Si in the experimental data using the original post-experiment source calibration.

Nucleus	Gamma Energy (keV)
^{197}Au	279.01(5) [86]
^{37}Ar	1611.24(5) [87]
^{35}Cl	3162.5(1) [88]
^{28}Si	6878.79(8) [89]

Table 4.3 The sources and energies of the gamma rays used in the final calibration of the HPGe detectors.

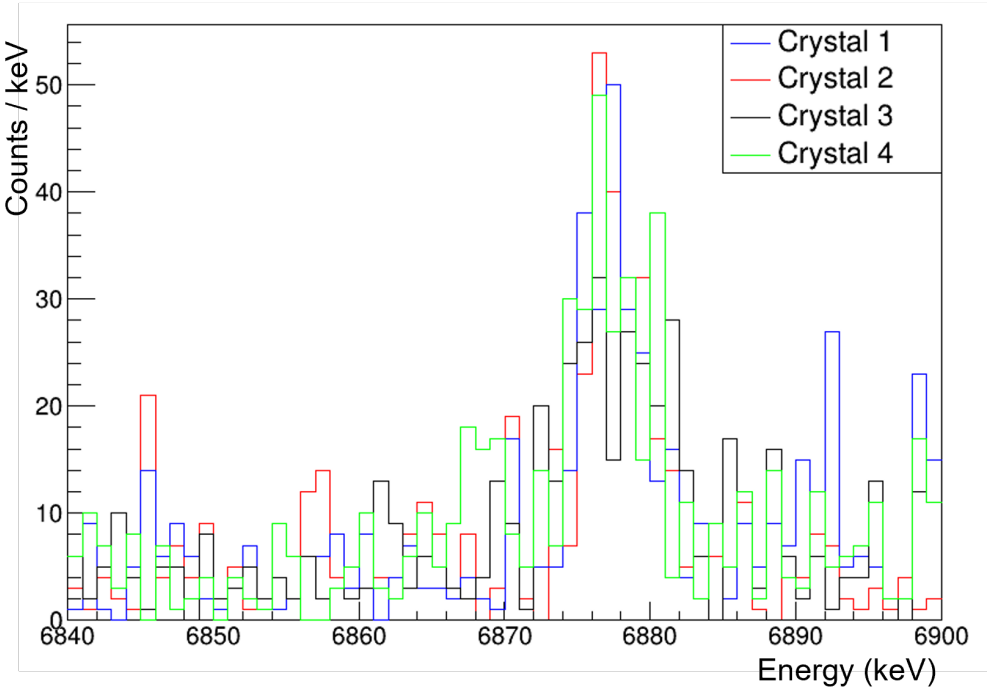

Figure 4.7 The gamma spectrum in each crystal of the HPGe detector for the 6.88 MeV gamma ray from ^{28}Si with the new calibration applied.

seen in Figure 4.7. The new calibration was checked in several peaks across the energy spectrum to ensure the calibration held at all energies of interest. There were no issues with the calibration in individual crystals.

Addback is a method to reduce Compton background at low energies and improve full-energy-peak statistics at high energies. There is a chance that a gamma ray will deposit some of its energy in one of the crystals by Compton scattering, then continue to deposit the rest of its energy in one or more of the other crystals. These partial gamma-ray energy depositions can be reconstructed by summing the energies in all crystals within a specified time window. The improved resolution of the HPGe detectors after the updated calibration revealed a double peaking issue in gamma peaks in the addback spectrum above approximately 3 MeV, shown in Figure 4.8.

This double peaking in the addback spectrum could be caused by crosstalk between the HPGe crystals, or it could be due to the different calibration applied to each crystal leading to incorrect

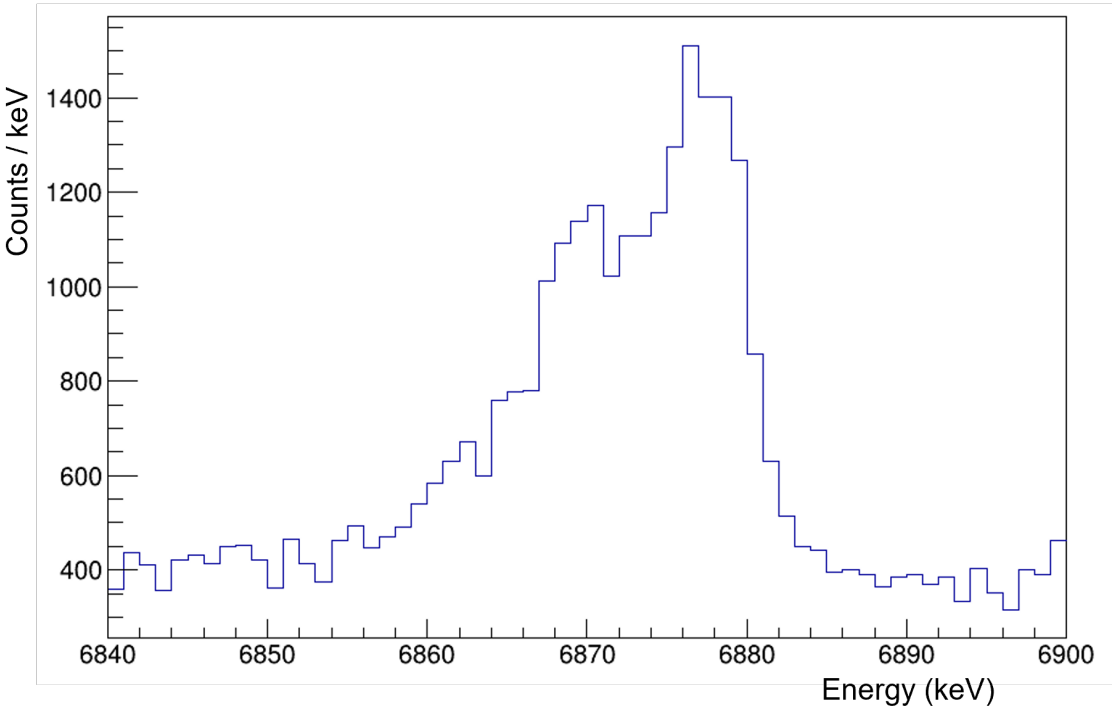

Figure 4.8 The 6.88 MeV gamma-ray peak from ^{28}Si in the addback spectrum. The feature around 6.869 MeV is not physical.

summing in the addback. It was concluded that it was not one specific crystal adding back incorrectly. The addback would hurt systematics more than it was improving statistics, so analysis proceeded with the singles spectrum. Figure 4.9 shows the singles and one addback spectrum for the 6.87 MeV gamma ray from ^{28}Si. The multiplicity 2 spectrum shows the hits that are reconstructed using signals in two of the crystals.

4.2 Response function

The differential pulse height distribution produced by a detector such as the HPGe gamma ray detectors when interacted with by a radiation source is referred to as the response function of the detector. The response function varies with energy, affecting energy resolution and lineshape. Several stopped gamma rays across the experimental spectrum were fit with an EMG function in order to determine the experimental detector response as a function of energy.

The relationship between the σ and τ parameters of an EMG function and energy can be char-

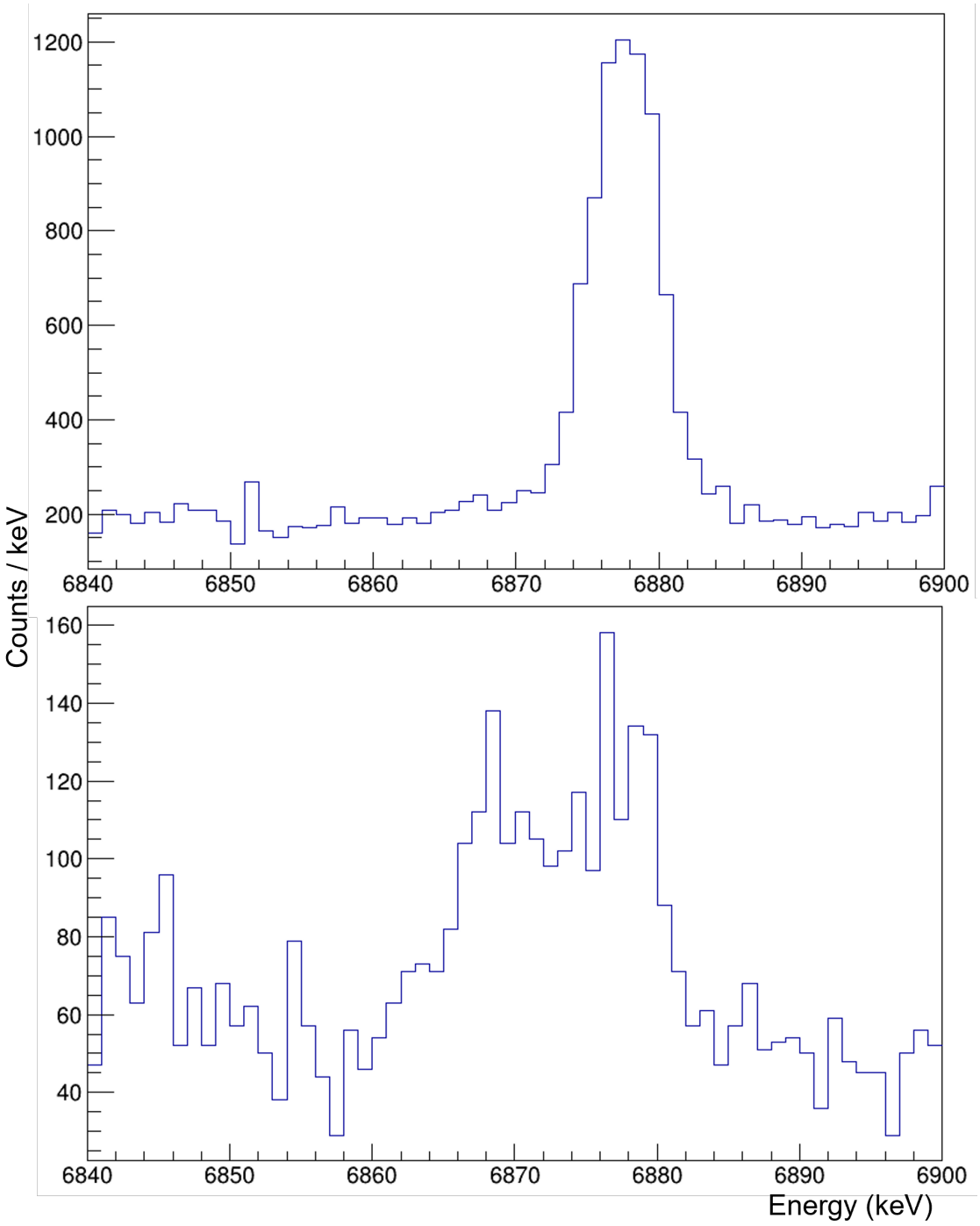

Figure 4.9 The 6.88 MeV gamma from ^{28}Si in the singles spectrum (top) and the multiplicity 2 spectrum (bottom).

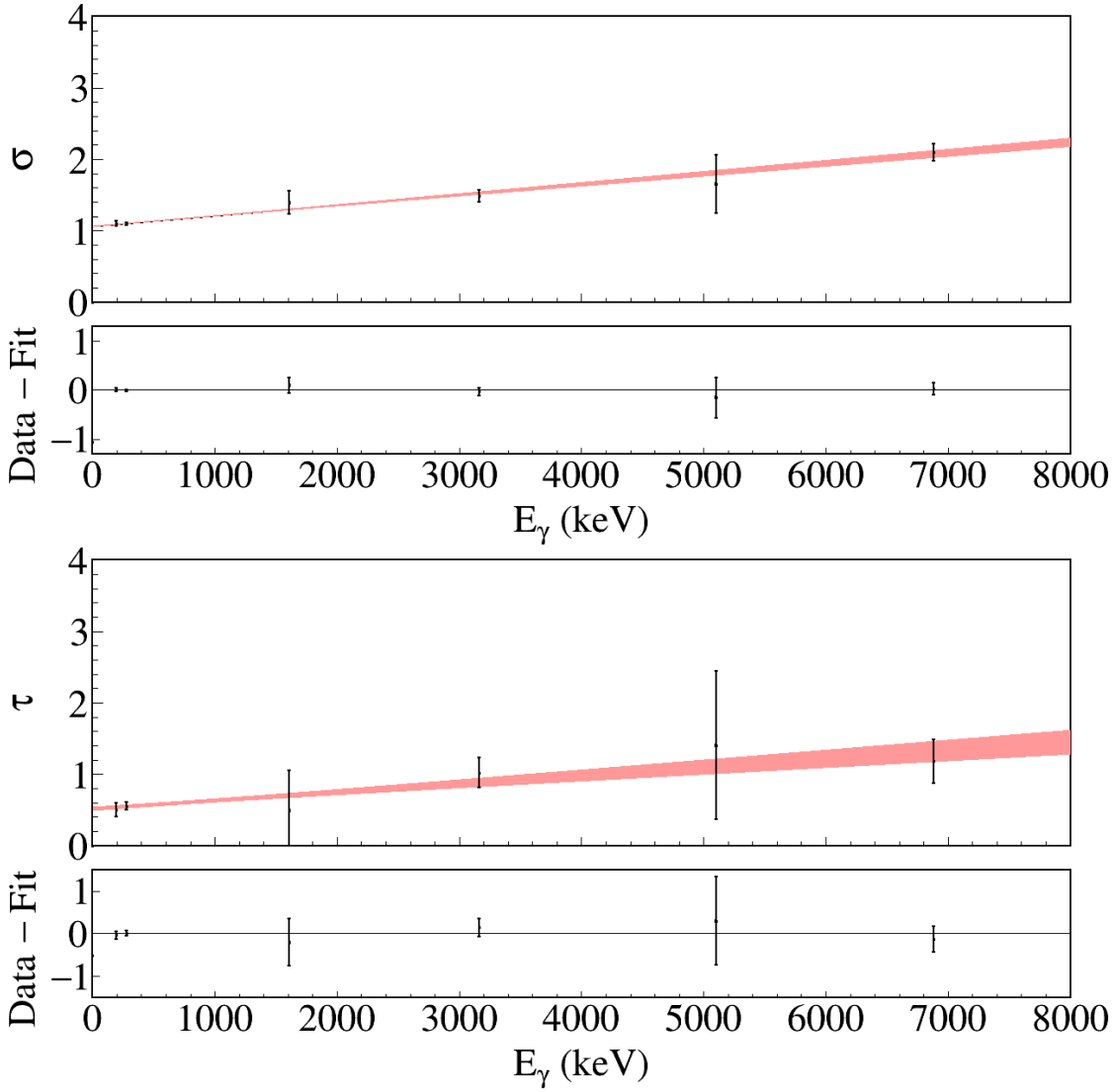

Figure 4.10 Linear fit of the σ (top) and τ (bottom) parameters of an EMG as a function of energy.

acterized by linear expressions. These expressions are important when modeling the experimental data. The linear fits of these parameters determined for this experiment are shown in Figure 4.10.

4.3 Detector Coincidences

Production of ^{23}Mg in this experiment will always coincide with the production of an alpha particle. The lifetimes that can be determined using DSAM are short enough that the detection of the emitted gamma ray will coincide with the detection of an alpha particle. In order to reduce background, a timing gate is set so only events with both a gamma ray and a charged particle detected are included. Figure 4.11 shows a sample timing spectrum produced by subtracting the

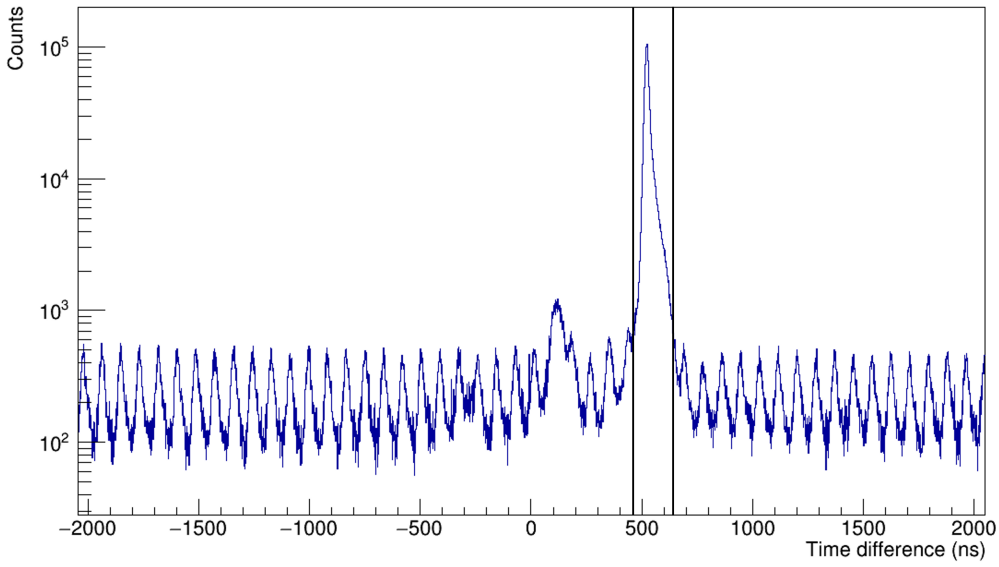

Figure 4.11 Time difference between events in the HPGe detectors and the ΔE detector. The black lines indicate the time gate set.

time of a detected charged particle from the time of a detected gamma ray, as well as the timing gate used in this analysis. More investigation is needed to understand the feature around a time difference of 100 ns.

4.4 Particle Identification

The energy loss of charged particles as they traverse a medium, or the stopping power of the medium, can be described by the Bethe formula,

$$-\frac{dE}{dx} = \frac{4\pi e^4 z^2}{m_0 v^2} NB \tag{4.2}$$

where e is the charge of an electron, ze is the incident particle charge, m_0 is the rest mass of an electron, v is the primary particle velocity, N is the number density of the absorber atoms, and

$$B \equiv Z\left[\ln\frac{2m_0v^2}{I} - \ln\left(1-\frac{v^2}{c^2}\right) - \frac{v^2}{c^2}\right] \tag{4.3}$$

where I is the average excitation and ionization potential of the absorber, which usually has to be determined experimentally for each case, and Z is the atomic number of the absorber atoms. For nonrelativistic particles ($v << c$), the stopping power can be written as

$$\frac{dE}{dx} = C_1\frac{z^2}{v^2}\ln(C_2v^2) \tag{4.4}$$

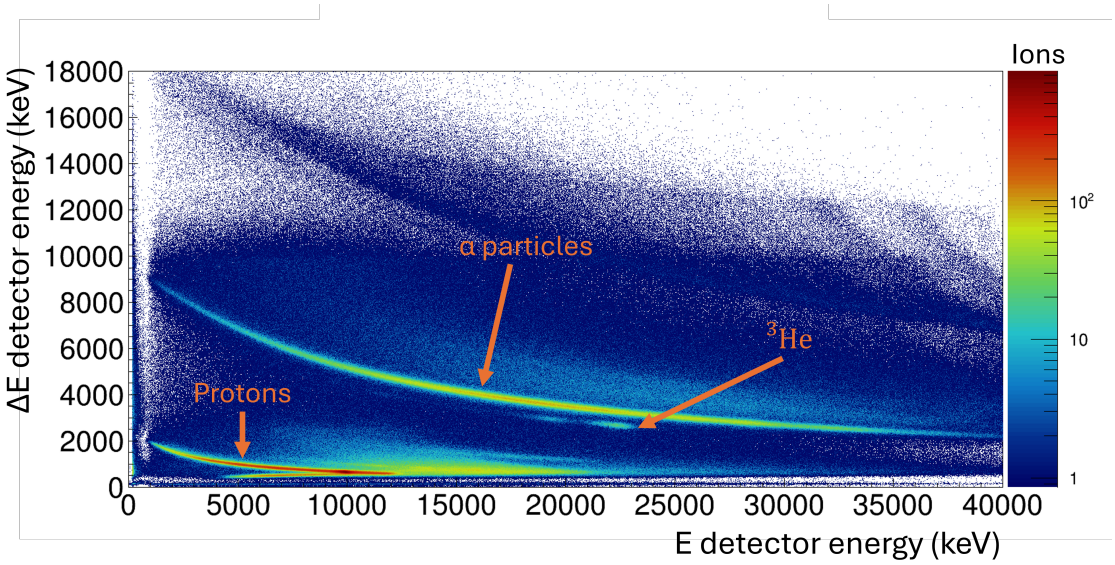

Figure 4.12 PID plot for all data taken using the target produced at LLNL. The proton, ^{3}He, and alpha particle bands are indicated.

where C_1 and C_2 are constants. Solving $E = \frac{1}{2}Mv^2$ where E is the energy of the incident particle and M is the incident particle mass, for v^2 allows us to substitute an energy-dependent expression for v^2, resulting in

$$\frac{dE}{dx} = C_1' \frac{Mz^2}{E} \ln(C_2' \frac{E}{M}) \tag{4.5}$$

where C_1' and C_2' are modified versions of the previous constants. From this, we can conclude that the energy loss ΔE of a particle in a set amount of a material such as silicon, Δx, is mildly dependent on the energy of the energy of the particle, but is largely sensitive to Mz^2. This can be expressed as

$$E\Delta E \propto Mz^2 \tag{4.6}$$

Therefore, a plot of the energy deposited by particles in the ΔE detector versus the energy deposited in the E detector of the Si telescope will show identifiable hyperbolic curves for different particle groups as defined by different values of M and z [62]. This plot is referred to as a particle identification (PID) plot. A PID plot from this experiment is shown in Figure 4.12.

4.5 Target Analysis

It was assumed before the experiment that the target produced at LLNL had more contaminants on its surface than the target produced at TRIUMF did, due to the visible discolored spot on the target surface. It was also suspected that the TRIUMF target had less ^{3}He due to the misalignment of the ^{3}He beam during implantation. Analysis after the experiment was able to confirm both of these assumptions.

Much of the background in the experiment was produced by fusion evaporation reactions between the beam particles and contaminants on the surface of the targets. Fusion evaporation reactions occur when two heavy ions collide and fuse to form an excited compound nucleus. The evaporation part of the reaction occurs when the compound nucleus then emits light particles such as protons, neutrons, and alpha particles. Figure 4.13 shows two PID plots, each produced from runs of similar length and incident beam current for each of the two targets used. It is clear from the increased number of particles, including those above the alpha band, that more contamination was present on the target produced at LLNL.

PACE4 [90], a modified version of the JULIAN fusion evaporation code [91] in the LISE++ package [92], was used to calculate the most likely reaction products from fusion evaporation reactions of the ^{24}Mg experimental beam and ^{12}C and ^{16}O surface contaminants on the targets. The gamma spectrum with a broad gate on all alpha particles was investigated to identify stopped peaks that could be attributed to these fusion evaporation reaction products.

A rough analysis of the identified peaks did in fact confirm a higher level of contamination on the target produced at LLNL. This rough analysis investigated both the number of peaks that were able to be associated with fusion evaporation reaction products and counts in these peaks normalized to amount of incident beam.

The amount of ^{3}He in each target was estimated by integrating the number of counts in the region representing elastically scattered ^{3}He on the PID plot created for each target and normalizing to the number of beam particles delivered to each target. Figure 4.14 shows the normalized amount of scattered ^{3}He in each run during the experiment. From this it was concluded that the spot on

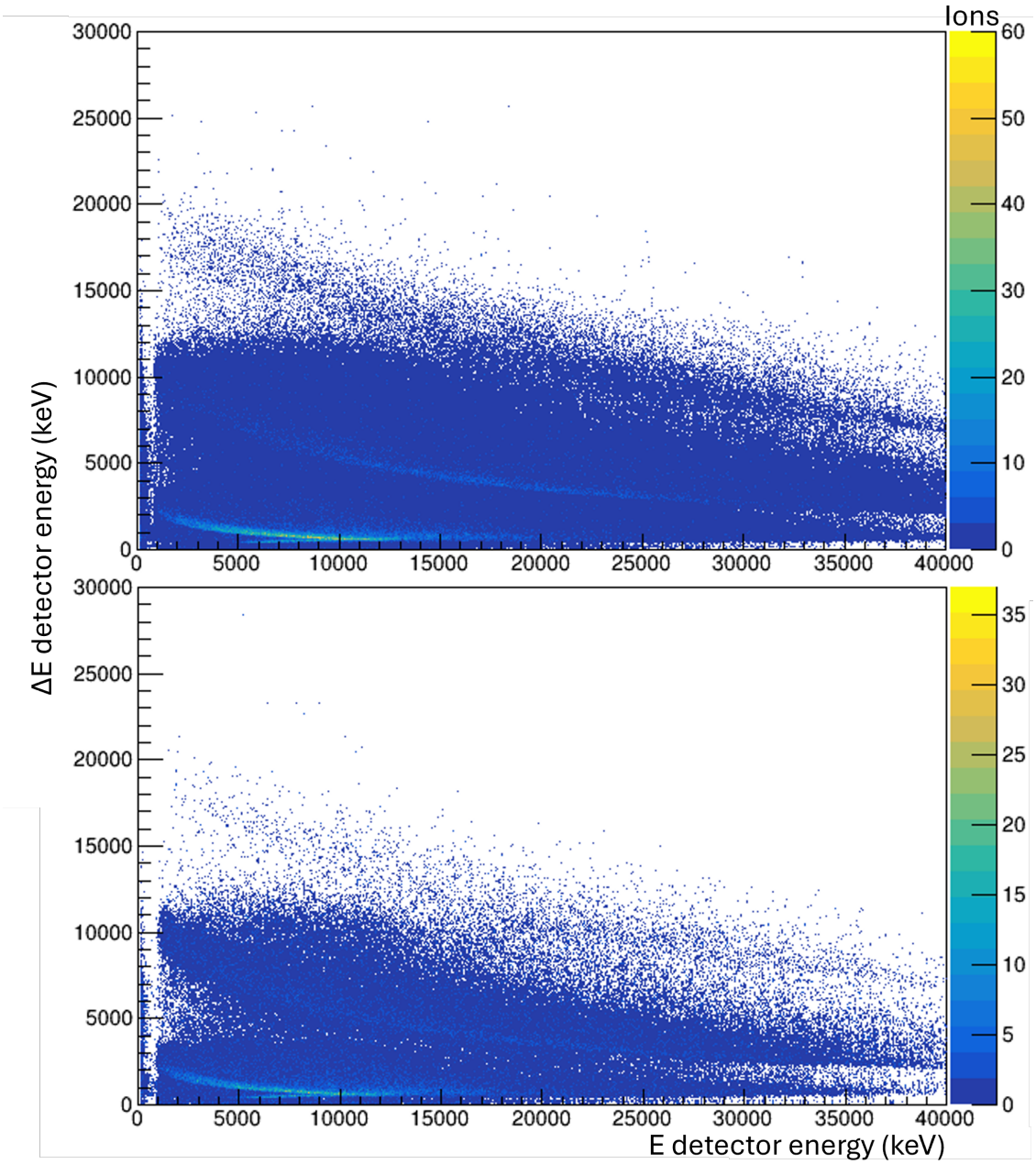

Figure 4.13 PID plots from runs with equal amount of incident beam on the target produced at LLNL (top) and on the target produced at TRIUMF (bottom).

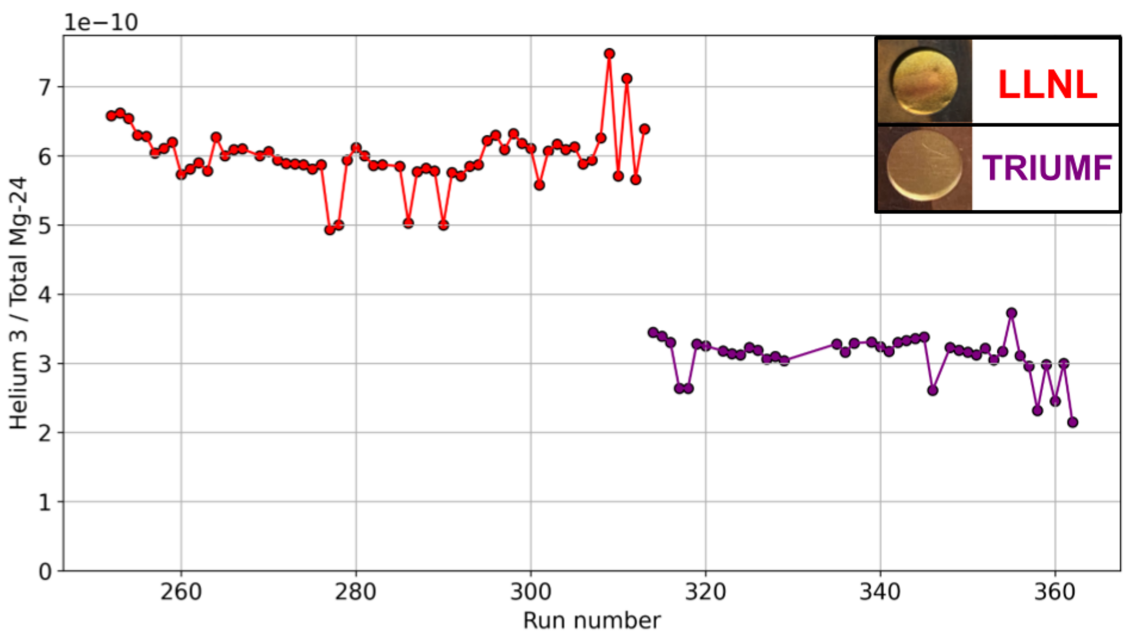

Figure 4.14 Scattered ^{3}He during each run of the experiment, normalized against the amount of incident ^{24}Mg beam in each run. The inset figures show photos of the two targets used, and the text color indicates which data points correspond to each target. Figure by Chloe Ricker.

the LLNL target that the beam impinged upon had about twice as much ^{3}He as the spot on the TRIUMF target impinged upon by the beam. It was also determined that not much ^{3}He was lost as the targets were bombarded during the experiment.

Due to the contamination on the target produced at LLNL, the analysis proceeded using only the data taken on the target produced at TRIUMF. More beam time was spent on the target produced at LLNL due to the unplanned early conclusion of the experiment caused by the loss of the beam. The target produced at LLNL also contained more ^{3}He at the spot impinged upon by the ^{24}Mg beam than the target produced at TRIUMF. However, the signal-to-background ratio in the regions of interest in the gamma spectra was too poor for proper analysis when the full dataset was used. In the case of the peak of astrophysical interest around 7.8 MeV, the signal-to-background ratio is significantly worse in the data taken on the LLNL target, as shown in Figure 4.15.

4.6 Pixel Groups

The 32 overlapping strips of the ΔE detector produce pixels that can be used to constrain the location of a detected charged particle. A hit map of all charged particles detected during a one

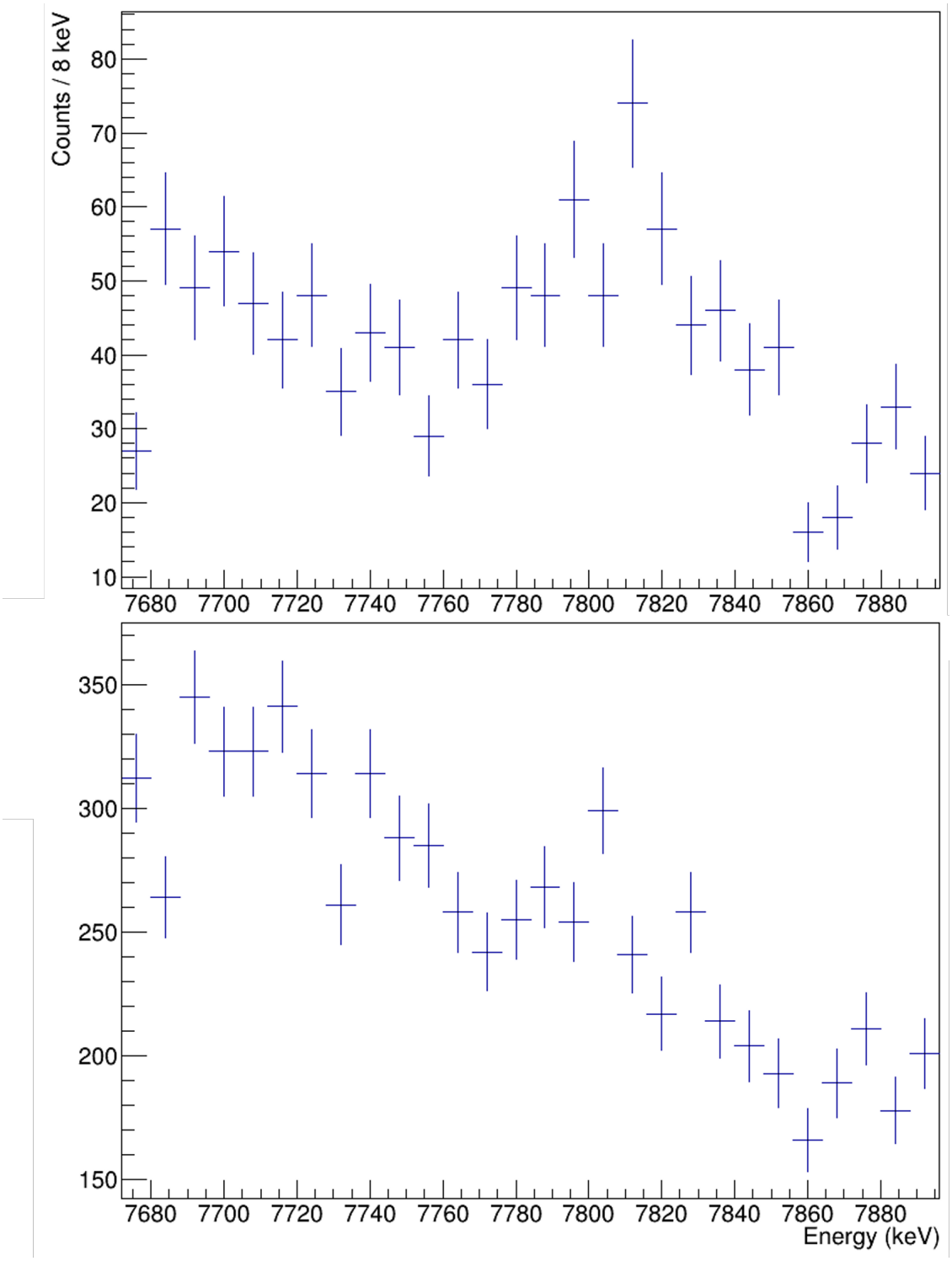

Figure 4.15 Gamma spectra showing the peak of astrophysical interest in the data taken on the target produced at TRIUMF (top) and on the target produced at LLNL (bottom).

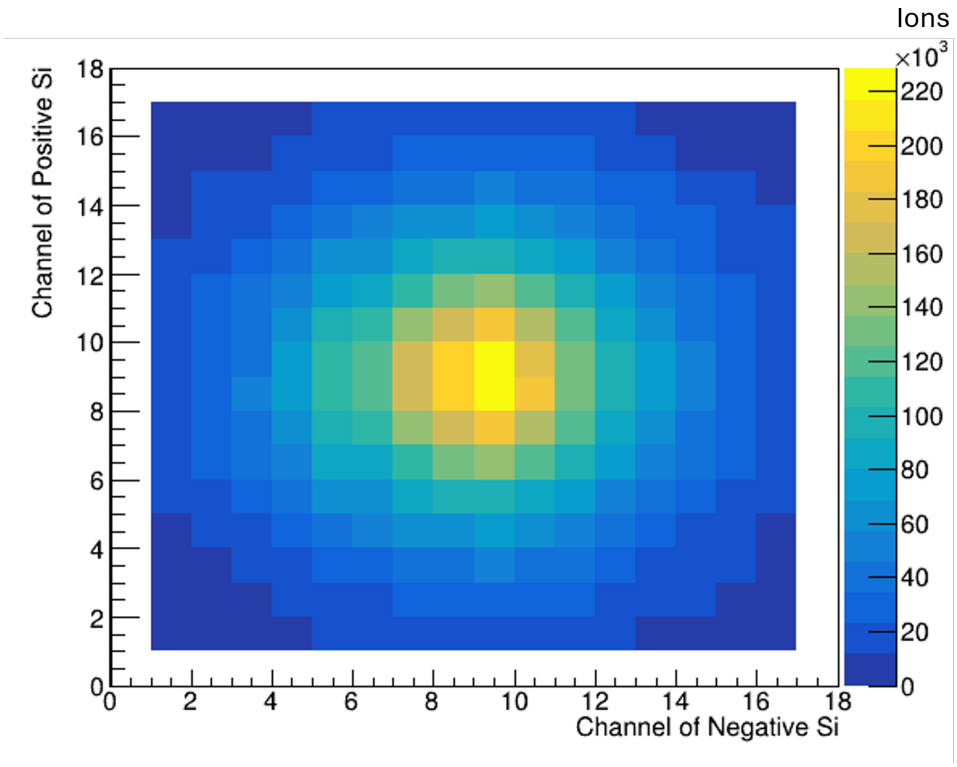

Figure 4.16 Map of charged particle interactions with each pixel of the ΔE detector during a 1 hour run of the experiment.

hour run of the experiment is shown in Figure 4.16. This served as confirmation that the beam was aligned with the center of the detector, which allows for the pixels to be grouped symmetrically despite not knowing which vertical strip was leftmost and which was rightmost.

The pixels created by the overlap of two strips were identified each by a number 1-256 and assigned to ring-like groups. Figure 4.17 shows the name assigned to each pixel and the group definitions.

The approximate angular coverage of each group is listed in Table 4.4. This was determined using the distance between the target and the ΔE detector and the distance of the topmost pixel edge from the center of the detector to calculate the approximate maximum angular acceptance of the group, as illustrated in Figure 4.18. The angular coverage of the group was then defined as the angles between the previous group's maximum angular acceptance and the group's own maximum.

In order to produce alpha gated gamma spectra, a gate on all alpha particles was first applied. Then specific alpha energy gates were set on each group for each state investigated to select particular

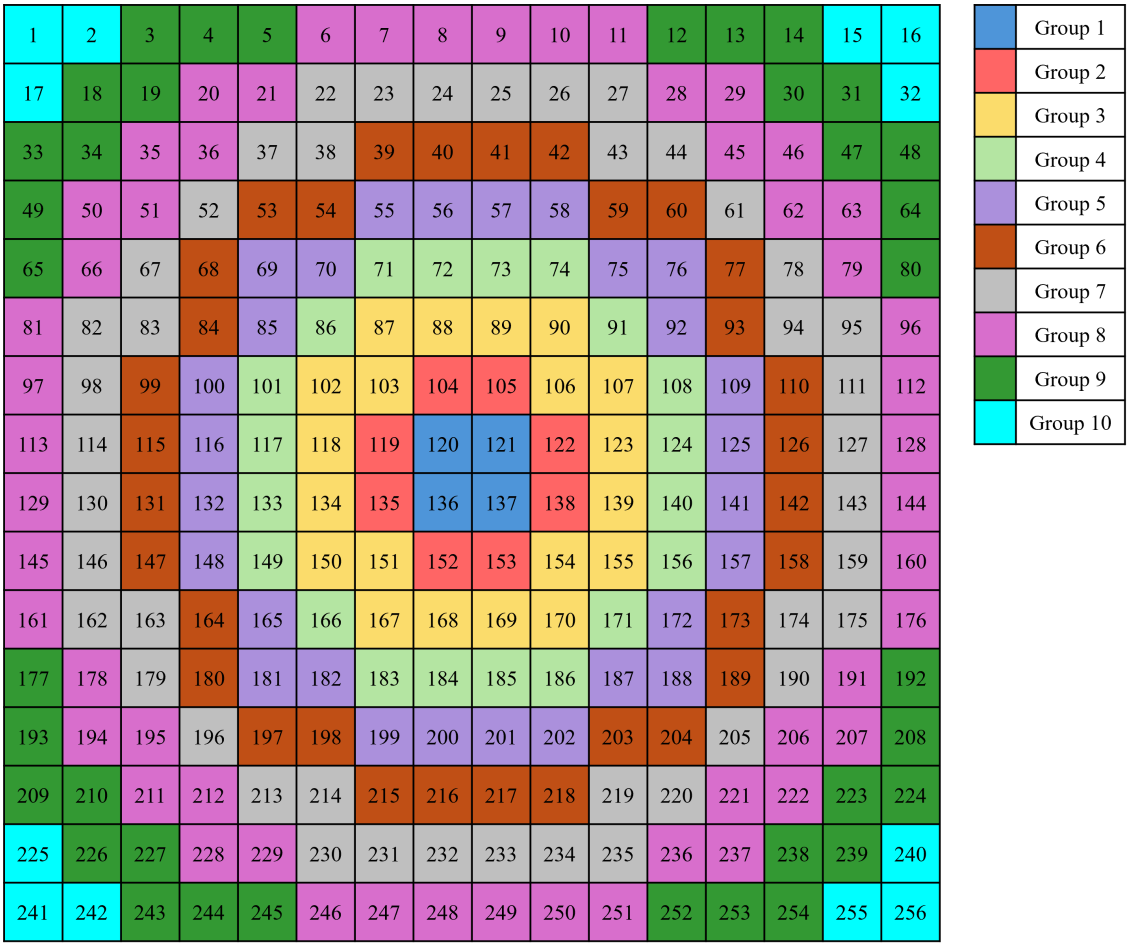

Figure 4.17 Map of the pixels of the ΔE detector and the groups comprised of them. In this orientation strip 17 is the leftmost vertical strip.

Group	Angular Coverage
1	0°–9.65°
2	9.65°–18.78°
3	18.78°–27.02°
4	27.02°–34.22°
5	34.22°–40.37°
6	40.37°–45.57°
7	45.57°–49.96°
8	49.96°–53.68°
9	53.68°–56.83°
10	56.83°–59.54°

Table 4.4 Approximate angular coverage of each group of ΔE detector pixels, starting from the center of the detector.

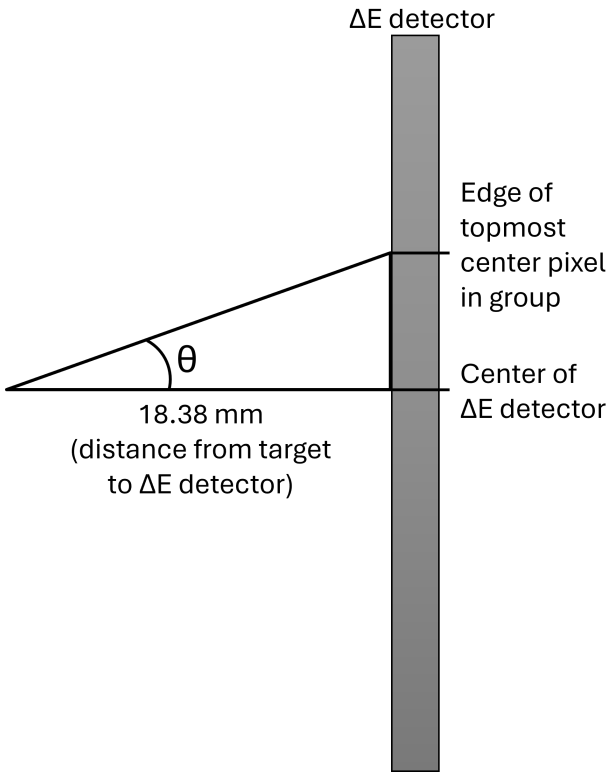

Figure 4.18 Schematic of how the approximate angular coverage of each group of pixels was calculated.

states in ^{23}Mg populated by the ^{24}Mg(^{3}He,α) reaction. These gates were initially determined using the GEANT4 simulation discussed in section 4.7, and were fine-tuned empirically using experimental data to produce the best signal-to-background ratio in the gamma spectra. The use of pixel groups for gating mitigates the effects of kinematic broadening of the alpha particles on the coincident gamma ray spectrum.

4.7 GEANT4 Simulation

Monte Carlo simulations utilize random sampling to produce numerical results. A Monte Carlo simulation was developed in GEANT4 in order to model lineshapes with known parameters for comparison with experimental data in order to carry out the DSAM lifetime determination. GEANT4 provides the ability to simulate the interactions of various particles with matter [93, 94].

The simulation begins by sampling the position in which the transfer reaction takes place. The depth profile of the implanted ^{3}He was calculated using SRIM [95], and from this, the simulated

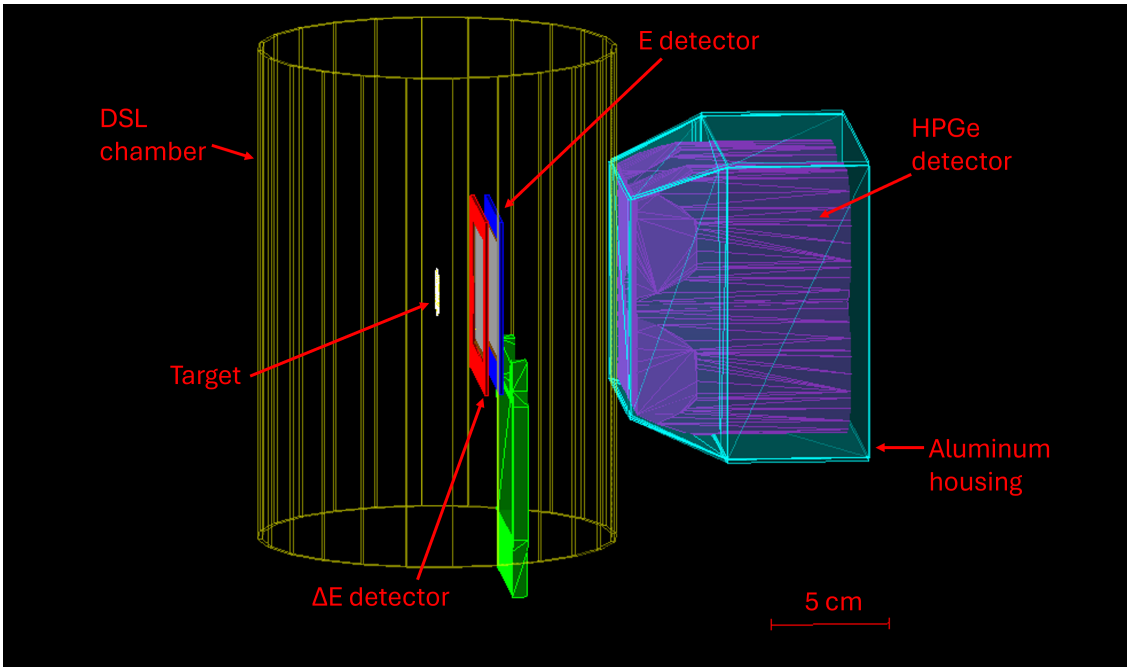

Figure 4.19 Geometry of the DSL2 setup in the GEANT4 simulation.

Au target was updated from 25 μm of pure Au to a 0.2 μm 68% Au region followed by a 24.8 μm pure Au region. The kinetic energy of the beam is modeled as a 2D Gaussian with a spread of 0.2% FWHM. The energy of the ^{24}Mg at the time of the reaction is dependent upon the position within the target, due to energy loss in the target. The stopping power provided by GEANT4 is expected to be accurate within 10% in general [96]. A Q-value for the ^{3}He(^{24}Mg,α) reaction to the ground state in ^{23}Mg of 4.0464 MeV [97] is used, with the specific Q-value for the population of each excited state is calculated following

$$Q = Q_0 - E_{ex} \tag{4.7}$$

where Q_0 is the aforementioned 4.0464 MeV, and E_{ex} is the excitation energy of the populated state in ^{23}Mg. A lifetime for the populated state is also defined.

The simulated geometry of the setup is shown in Figure 4.19. The HPGe crystals are taken to be one single detector, and the geometry of the GRIFFIN detector's aluminum housing is simplified. The target ladder is left out of the simulation for simplicity, though the frame that holds the Si detector telescope is included to take into account the fact that it will block some gamma rays.

The angular emission of the alpha particles is sampled from a distribution determined by FRESCOX. More information on the FRESCOX input is provided in section 4.7.1. The EMG response function of the HPGe detectors as discussed previously in section 4.2 is applied to the gamma rays recorded. Each simulation prepared for use in the lineshape analysis was ran with a number of events sufficient to produce at least an order of magnitude more counts in the peak of interest in the simulated spectra than in the experimental data in order to minimize the effect of statistical fluctuations in the simulation on the quality of the fit of the simulation to the data.

4.7.1 FRESCOX Angular Distribution

FRESCO was developed to perform coupled-reaction channels calculations by Prof. Ian Thompson at LLNL (and previously at the University of Surrey). Its most recent iteration, which was used in this work, is known as FRESCOX [98]. Optical model parameters are required for the calculation of a transfer reaction such as this. The parameters used are taken from [99] and [100]. FRESCOX calculations take into account the spin and parity of the nuclear excited states being populated, which grants the analysis some sensitivity to spin and parity.

The angular distribution for the outgoing alpha particles generated by FRESCOX is in the center-of-mass frame, while the GEANT4 simulation is in the lab frame. Therefore a conversion between the two frames must be done in order to use the FRESCOX output in the simulation. For each alpha emission angle output by FRESCOX in the center-of-mass frame, the angle in the lab frame is calculated using

$$\tan\theta = \frac{\sin\theta'}{\cos\theta' + \gamma} \tag{4.8}$$

where θ is the emission angle in the lab frame, θ' is the emission angle in the center-of-mass frame, and γ is defined as

$$\gamma = \sqrt{\frac{m_a m_b E_a}{m_b(m_b + m_B)Q + m_B(m_B + m_b - m_a)E_a}} \tag{4.9}$$

where m_a is the mass of the projectile nucleus (in this case ^{24}Mg), m_b is the mass of the ejected alpha particle, m_B is the mass of the ^{23}Mg, and E_a is the energy of the ^{24}Mg at the time of the reaction, taken to be 74 MeV.

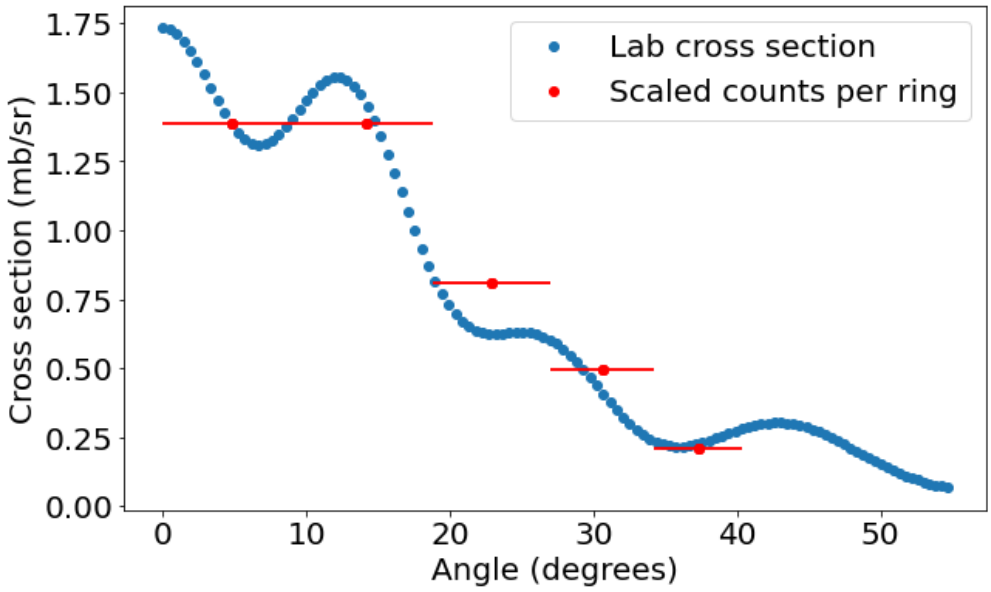

Figure 4.20 Plot of FRESCOX output in the lab frame (blue) and experimental counts per pixel ring scaled by the geometric efficiency of the detector (red) for the 6th excited state in ^{23}Mg. The horizontal bars on the experimental data indicate the angular coverage of the ring.

The differential cross section at each angle in the lab frame is calculated following

$$\frac{(d\sigma/d\Omega)'_{\theta'}}{(d\sigma/d\Omega)_{\theta}} = \frac{\sqrt{1-\gamma^2\sin^2\theta}}{\left(\gamma\cos\theta+\sqrt{1-\gamma^2\sin^2\theta}\right)^2} \tag{4.10}$$

where $(d\sigma/d\Omega)$ is the cross section. The GEANT4 simulation samples from the distribution of the cross section as a function of angle.

A sample FRESCOX output converted to the lab frame and compared to experimental data is shown in Figure 4.20.

4.8 MCMC Bayesian Analysis

Bayesian inference is a method to determine the probability of a hypothesis, in this case constructed of model parameters, given prior evidence, in this case experimental data, using Bayes' Theorem [101]. The set of experimental data, D, is compared to the set of model parameters, x, while also considering the probabilities involved. The experimental data in this case are the observed gamma spectra, and the model parameters are used to simulate gamma spectra.

$P(x)$ represents the prior probability distribution, which is an expression of the uncertainties

associated with the model parameters. $P(D)$ is the probability of observing the experimental data without taking into account the model. Given that the data were observed and thus are known, $P(D)$ is treated as a normalization factor in this case. $P(D|x)$ is the likelihood of the data being observed given the model parameters. In the case of this work, for one specific gamma spectrum, this is determined by fitting the simulated spectra to the experimental spectrum and quantifying the goodness of fit using the χ^2 of the fit. From these, the probability distribution of the model parameters given the data, or the posterior distribution, can be determined following

$$P(x|D) = \frac{P(D|x)P(x)}{P(D)} \tag{4.11}$$

Because the experimental data are gamma spectra represented by a number of observed counts per bin, the analysis is performed on a bin-by-bin basis [102]. The likelihood in this scenario is taken to be

$$\mathscr{L}(x) \approx \exp\left[-\sum_{i=1}^{n} \frac{[y_i^{\text{exp}} - y_i^{\text{mod}}(x)]^2}{2\sigma_i^2}\right] \tag{4.12}$$

where n is the number of bins in the spectrum, y_i^{exp} is the number of counts in a given bin in the experimental spectrum, y_i^{mod} is the number of counts in a given bin in the simulated spectrum, and σ_i accounts for all uncertainties, which are assumed to be Gaussian [68].

The model parameters considered in this analysis are the lifetime of the excited state, the energy of the gamma ray emitted, the relative background generated by convoluting a linear background with the simulated spectrum scaled to fit the data, and the stopping power of the target.

The priors for each parameter are set as follows:

- Lifetime: A uniform prior is used. In the case of a short-lived state, the prior is set between at minimum 0 and the maximum lifetime simulated, since a negative lifetime is unphysical.
- Gamma ray energy: A uniform prior is used. Previously a Gaussian distribution had been considered, using the literature value as the mean and the uncertainty bounds as 1σ uncertainty, but initial analysis suggested the literature values for the gamma ray energy and its uncertainty were not sufficiently certain for this analysis. The uniform prior spans the range of simulated energies.

- A Gaussian distribution for the background level based on the uncertainty of the linear fit in the region around the gamma ray peak was used.

- A Gaussian distribution for the stopping power was used, centered at the database values provided by GEANT4 and assuming a 1σ uncertainty of 10% [96].

A Markov chain is a process in which the next state or event in a sequence is only determined by the current event, uninfluenced by past events [103]. The Markov chain Monte Carlo (MCMC) algorithm used in this work generates random walk through the parameter space populated by the Monte Carlo simulations produced using GEANT4. Each step is determined by the product of the prior and the likelihood [104, 105].

The model outputs are then reduced to a smaller number of uncorrelated variables through principal component analysis (PCA) [106]. In PCA, the first principal component of the set of variables is a linear combination of the original variables such that the most variance between the variables is explained. The next principal component explains most of the remaining variance, and so on until the addition of more principal components does not lead to meaningful gain in the cumulative explained variance. The projection of the counts per bin of each simulation onto each principal component is referred to as the latent outputs. In general, the purpose of PCA is to reduce the dimensionality of the problem while extracting features of the original set.

Gaussian Process (GP) is a probabilistic model that can be used for regression tasks [107]. GP's extrapolation ability is often poor, but the inclusion of unrealistic simulations can also decrease predictive accuracy [108], so a plausible but not restrictive range of parameter values should be chosen for simulations. A GP model is fit for each latent output, and a GP emulator is trained on the input-output behavior of the model. The GP emulator and MCMC sampler used in this work are from the surmise package [109] from the Bayesian Analysis of Nuclear Dynamics (BAND) framework [110].

The simulations are split into training and test sets in order to validate the emulator. The training set is used to fit the emulator, and the test set is to check its predictive accuracy. The accuracy of

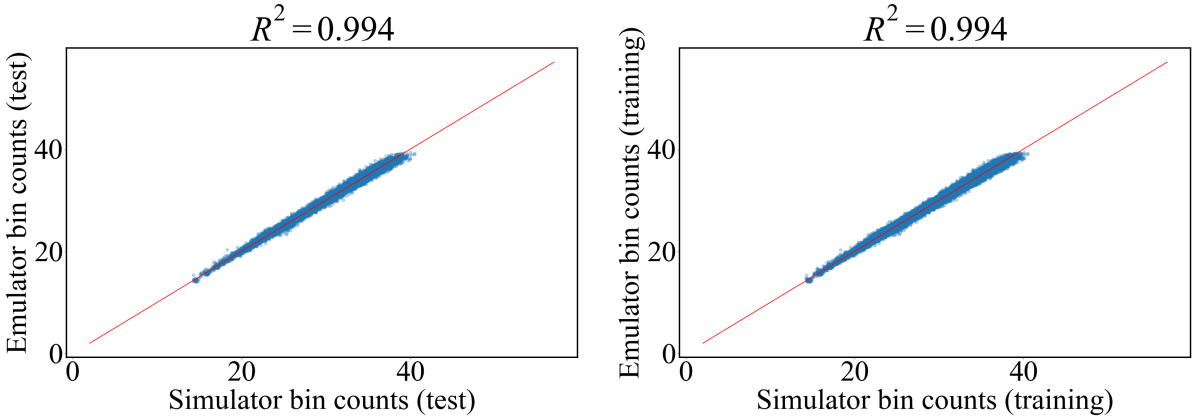

Figure 4.21 Comparison of the R-squared values for the training and test outputs of the emulator.

the emulator is evaluated using the mean squared error and the R-squared value, comparing the emulator results to the simulated spectra. A sample visualization of the R-squared calculation is shown in Figure 4.21.

The output from the MCMC Bayesian analysis provides information on the correlation between the investigated parameters. Discussion of the output of the analysis, including correlation between parameters, will be included in the next chapter on a case-by-case basis for each state in ^{23}Mg that was investigated. A general workflow of the MCMC Bayesian analysis is shown in Figure 4.22.

Bayesian statistical analysis as applied to DSAM provides several advantages. Not least of which is the ability to analyze the uncertainty in the lifetime result comprehensively, taking into account uncertainties in other values including systematic uncertainties. The correlation between parameters, such as between the lifetime and the gamma ray energy, may be improperly estimated in a standard χ^2 minimization frequentist approach. Not only does the Bayesian analysis allow for the uncertainties in the results due to correlations between parameters and the uncertainty in each parameter to be taken into account, but it also provides information about the correlation between parameters. In cases such as the analysis of the astrophysical state of interest in ^{23}Mg, where there is uncertainty in the excitation energy of the state and thus the gamma ray energy, being able to meaningfully quantify the correlation between the lifetime and the gamma ray energy, as well as the impact of the uncertainty in the gamma ray energy on the lifetime results provides vital insight into the issue.

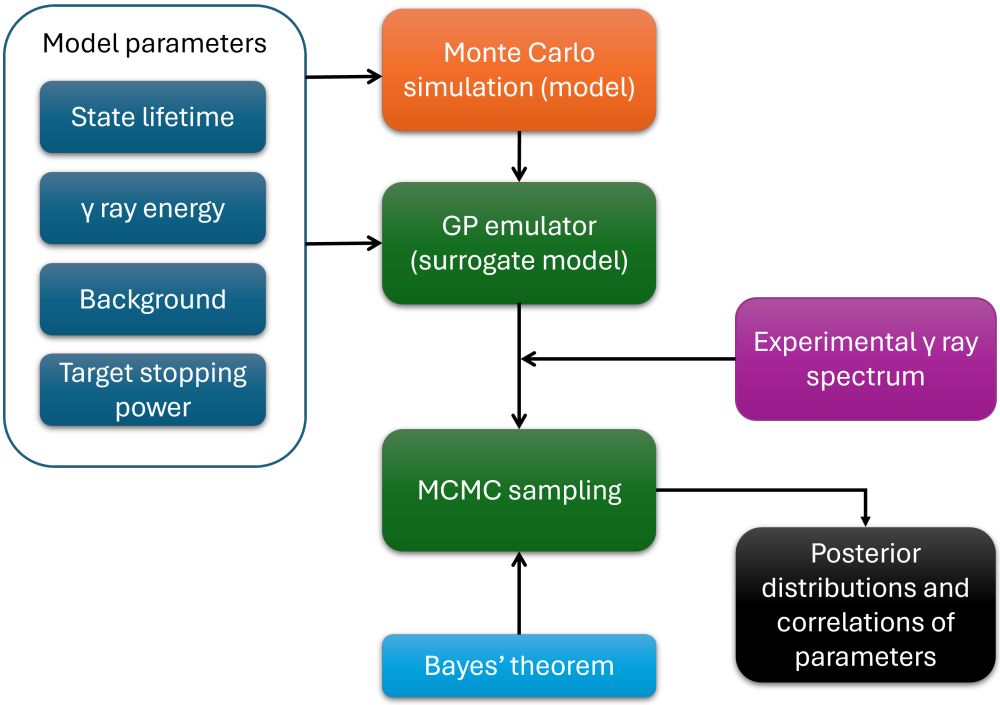

Figure 4.22 Workflow of the MCMC Bayesian analysis used in this work, adapted from [68].

The first application of a MCMC-based Bayesian analysis to DSAM data was developed by the DSL collaboration and was published in 2023 [68].

CHAPTER 5

RESULTS AND DISCUSSION

The results from the MCMC Bayesian analysis of the DSL2 data following the procedure outlined in the previous chapter are given here, in order of excitation energy. The results are summed up in one table, and discussed in the context of nuclear astrophysics and nuclear structure.

5.1 2nd Excited State

The 2nd excited state in ^{23}Mg has a literature excitation energy of 2051.6(4) keV, and a spin and parity of $7/2^+$ [13]. A sample fit of a simulation for this state scaled to fit the data and convoluted with a sloped linear background for this state is shown in Figure 5.1. The gamma spectrum shown was produced by gating on the alpha particles in groups 1 and 2 of the ΔE detector, with the energy gates used for each group given in Table 5.1.

The corner plot from the MCMC Bayesian analysis for this state is shown in Figure 5.2. The prior and posterior probability distributions for each parameter are plotted on the diagonal, and the plots below the diagonal show the correlation between the parameters.

The lifetime determined by this analysis for this state is 52^{+14}_{-12} fs. The gamma ray energy determined is $1597.4^{+0.8}_{-0.7}$ keV, corresponding to an excitation energy of $2048.2^{+0.8}_{-0.7}$ keV. The excitation energy determined for this state is lower than the current literature values of 2051.6(4) keV [13], though in relatively good agreements with the previous measurements of the excitation energy, shown in Figure 5.3. Previous measurements of the gamma ray energy include values of 1600 keV [47], 1601.4(13) keV [57], and 1601.8(11) keV [111], which are higher than the value determined in this work. The benefit of the Bayesian analysis used in this work allows for both the lifetime and the excitation energy (and as a result, the gamma ray energy) to be determined and the

Group	Low Energy Bound (MeV)	High Energy Bound (MeV)
1	31.20	33.10
2	27.82	31.68

Table 5.1 High and low energy bounds of the gates applied to the total deposited energy of alpha particles corresponding to each group to produce the experimental spectrum for the 2nd excited state in ^{23}Mg.

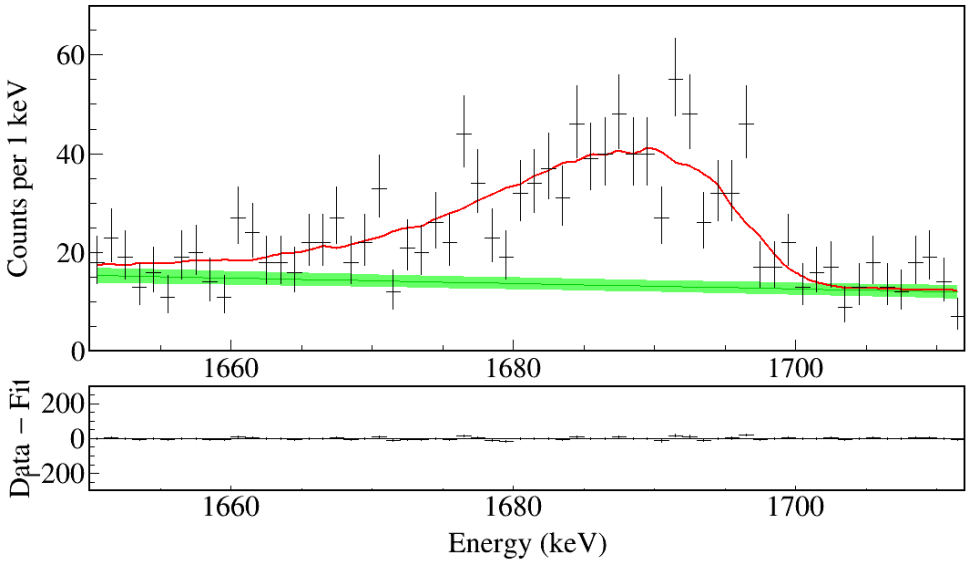

Figure 5.1 Scaled simulation plus sloped linear background fit to the experimental data for the gamma peak from the 2nd excited state in ^{23}Mg. The simulation assumes a lifetime of 60 fs, a gamma ray energy of 1597 keV, and uses the default stopping power provided in GEANT4.

uncertainties in both to be taken into account, preventing uncertainty in one value from influencing the other. The current literature value of the half-life of this state is 65(12) fs [13], corresponding to a lifetime of about 94(17) fs. The lifetime determined in this experiment is lower than the current literature value, and will be discussed more in section 5.6. The experiment using DSL1 to measure the lifetime of this state reported a value of 104(18) fs [57], though it is possible this value was influenced by the feeding of the 2nd excited state by the 4th excited state at an excitation energy of 2714 keV. The 4th excited state has a literature lifetime of 94(11) fs [13]. This analysis used the gamma spectrum produced by gating on the first two groups of pixels, and the 4th excited state appears to be successfully gated out for these groups, as the strongest peak from that state is not apparent in the experimental gamma spectrum. Future analysis using more pixel groups may need to modify the alpha gates on the other groups to mitigate the feeding from the 4th excited state.

5.2 6th Excited State

The 6th excited state in ^{23}Mg has a literature excitation energy of 2905.2(7) keV and a spin and parity of $3/2^+$ [13]. A sample fit of scaled simulation convoluted with a sloped linear background to

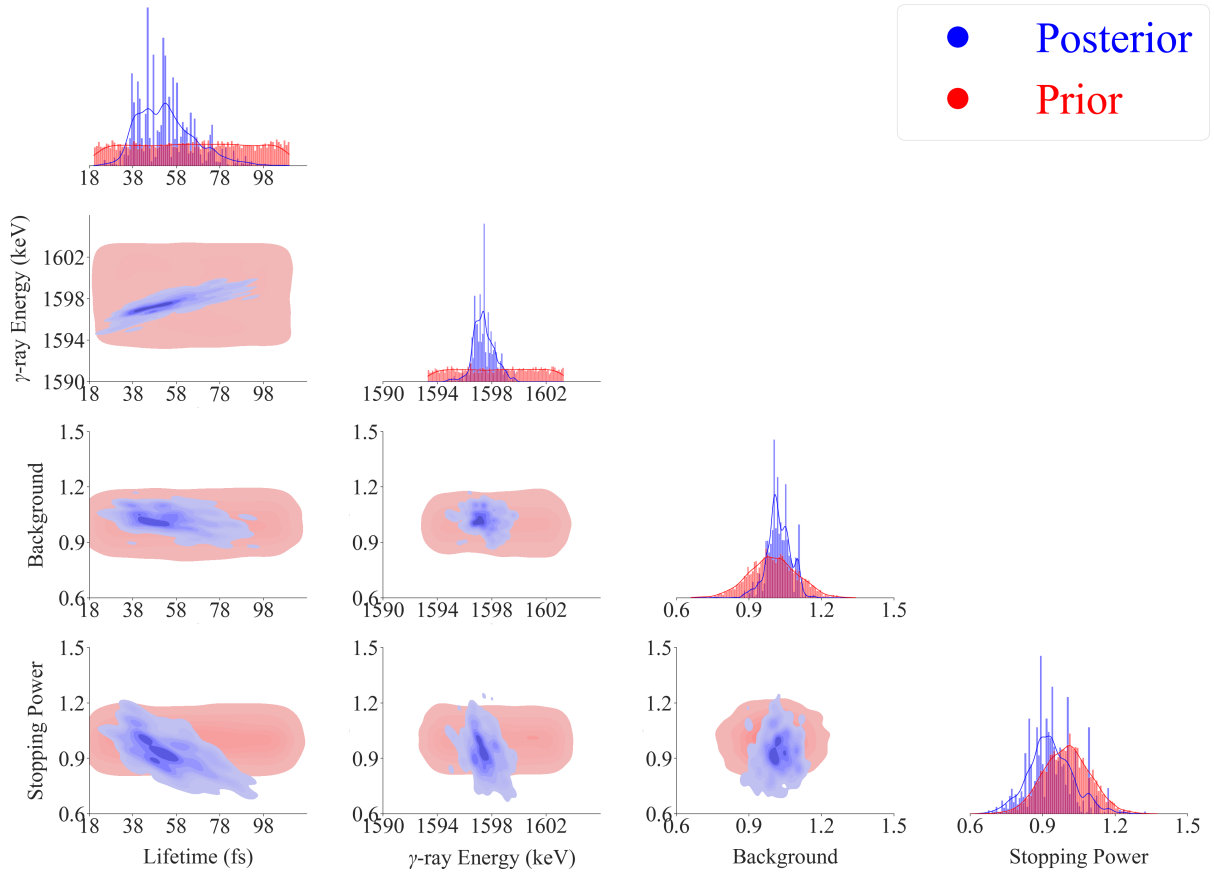

Figure 5.2 Corner plot output from the MCMC Bayesian analysis for the 2nd excited state in ^{23}Mg.

Group	Low Energy Bound (MeV)	High Energy Bound (MeV)
1	29.44	31.46
2	25.84	30.40

Table 5.2 High and low energy bounds of the gates applied to the total deposited energy of alpha particles corresponding to each group to produce the experimental spectrum for the 6th excited state in ^{23}Mg.

the experimental data for the 6th excited state in ^{23}Mg is shown in Figure 5.4. The gamma spectrum shown was produced by gating on the alpha particles in groups 1 and 2 of the ΔE detector, with the energy gates used for each group given in Table 5.2.

The resultant corner plot from the MCMC Bayesian analysis for this state is shown in Figure 5.5. It is clear from the posterior distribution of the background that the background was somewhat overestimated in the prior, though a benefit of the Bayesian analysis is that this is taken into account

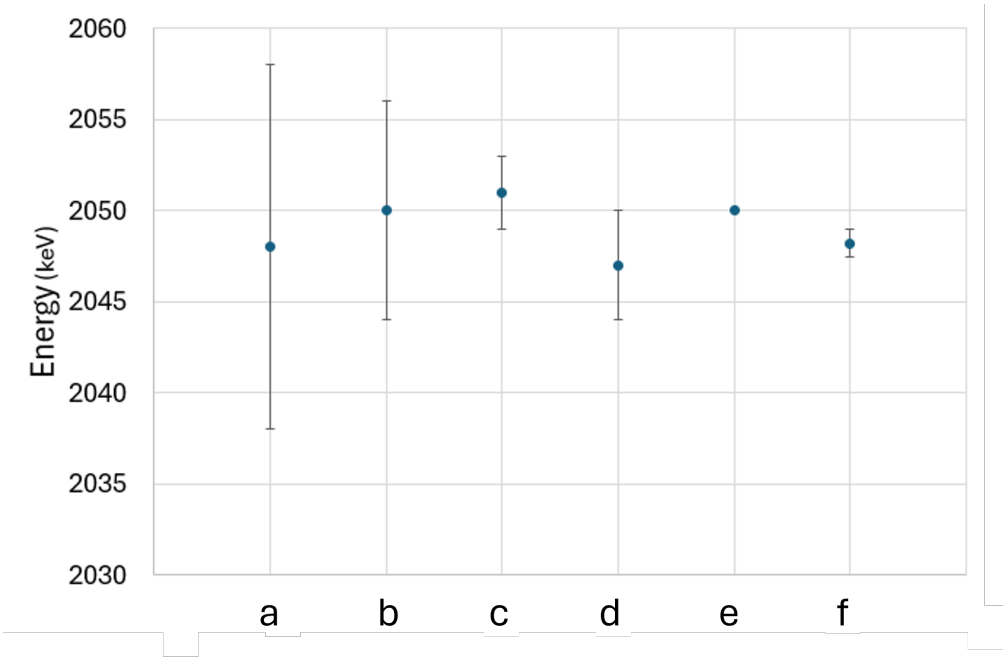

Figure 5.3 All published measurements of the excitation energy of the 2nd excited state in ^{23}Mg. a) From [112]. b) From [113]. c) From [114]. d) From [115]. e) From [47]. f) This work.

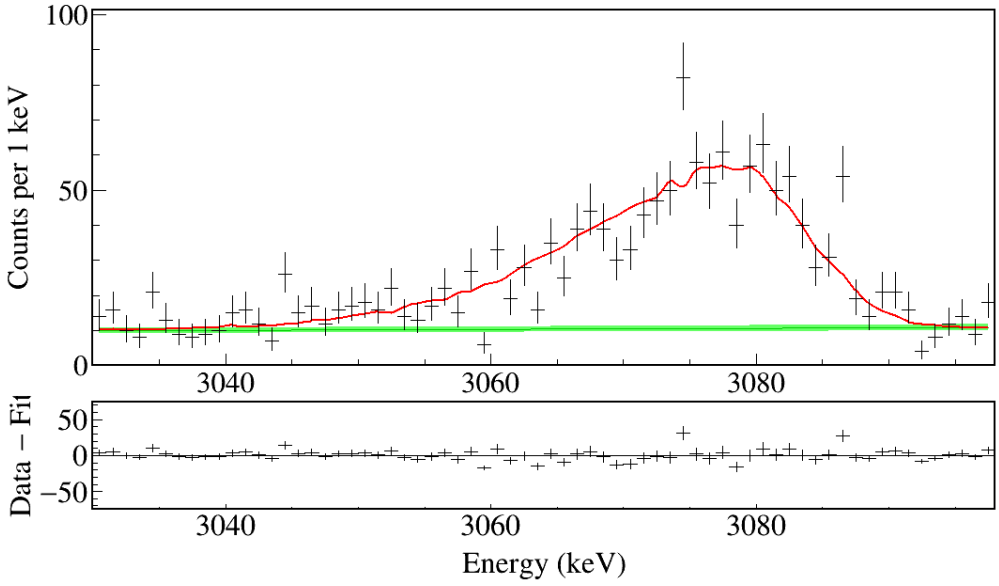

Figure 5.4 Scaled simulation plus sloped linear background fit to the experimental data for the gamma peak from the 6th excited state in ^{23}Mg. The simulation assumes a lifetime of 6 fs, a gamma ray energy of 2901 keV, and uses the default stopping power provided in GEANT4.

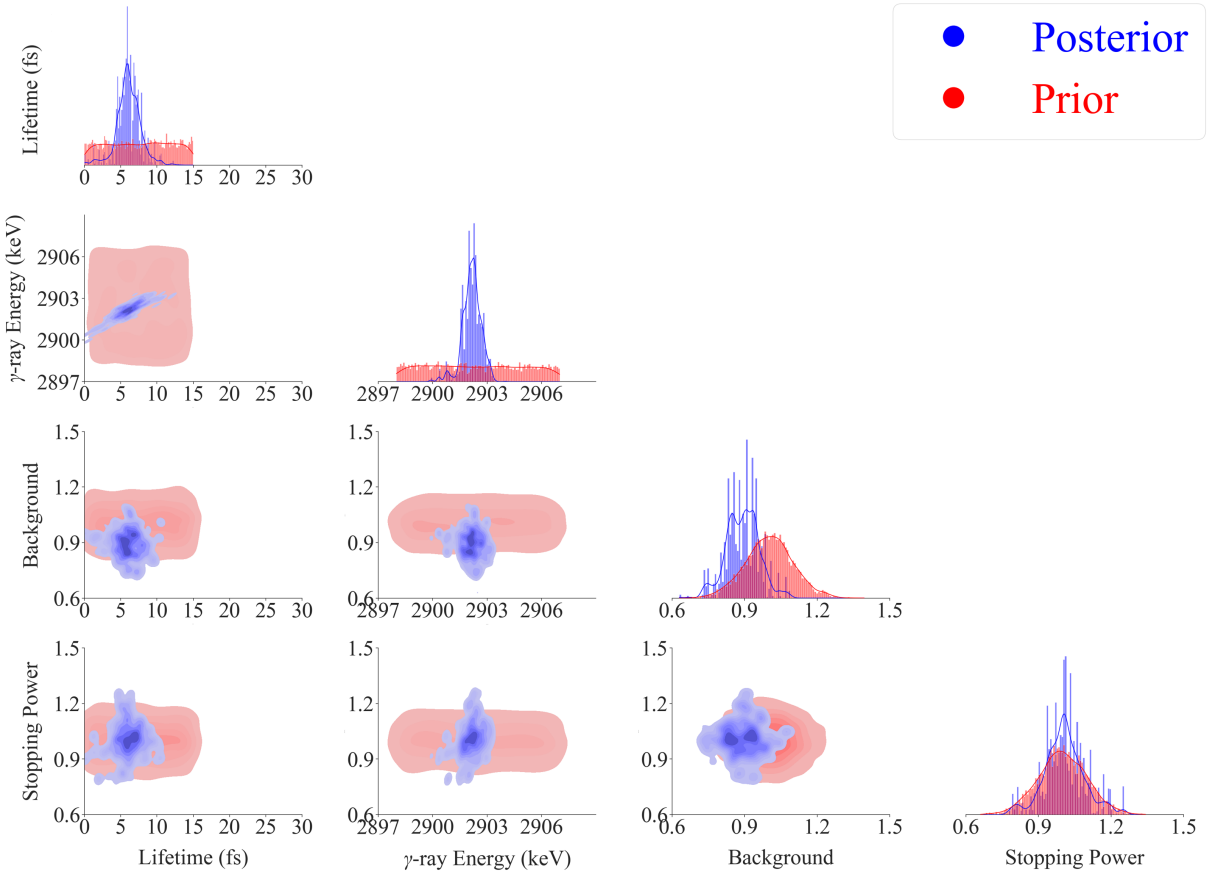

Figure 5.5 Corner plot output from the MCMC Bayesian analysis for the 6th excited state in ^{23}Mg.

when producing the final results. Future analysis could verify these results using a frequentist fit.

The lifetime determined for this state is $6.0^{+1.5}_{-1.4}$ fs and the gamma ray energy is $2902.2^{+0.5}_{-0.5}$ keV, corresponding to an excitation energy of $2902.4^{+0.5}_{-0.5}$ keV. The literature value of 2905.2(7) keV [13] for the excitation energy is higher than the value determined in this experiment, though that is in part due to one measurement which reported an excitation energy of 2908(3) keV [114]. All previous measurements of the excitation energy of the state as well as this result are plotted in Figure 5.6. The literature value for the gamma ray energy of 2906.4(11) keV comes entirely from the DSL1 experiment [57]. The Bayesian analytical tools used in this analysis allow for the correlation between the lifetime and gamma ray energy to be taken into more rigorous account, supporting the accuracy of the value determined in this work. The lifetime determined in this work is noticeably shorter than the present literature value of 15.0(30) [13]. More discussion on this will

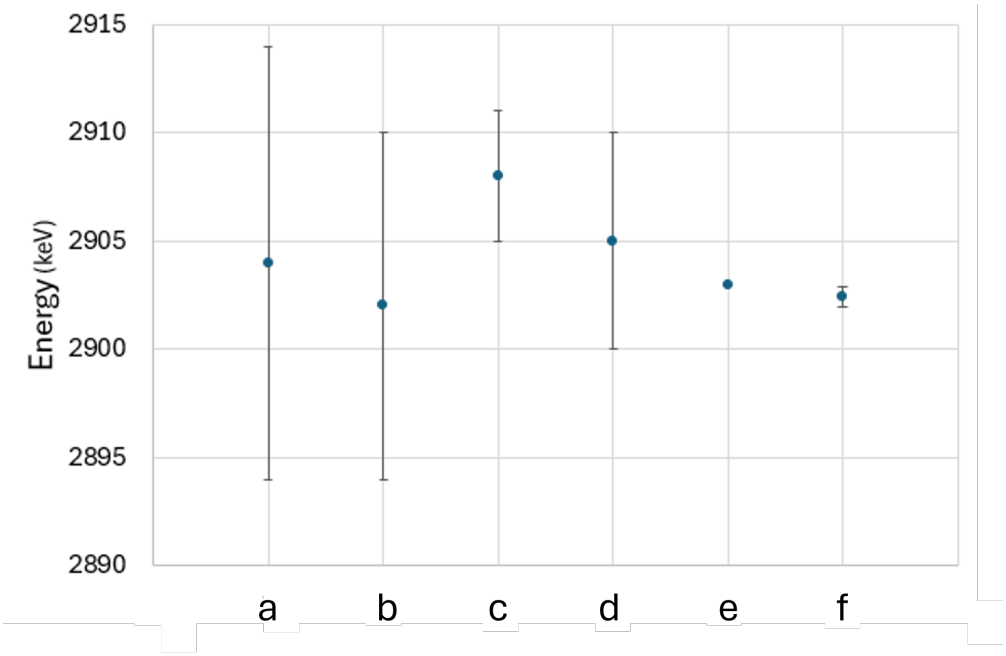

Figure 5.6 All published measurements of the excitation energy of the 6th excited state in ^{23}Mg. a) From [112]. b) From [113]. c) From [114]. d) From [115]. e) From [47]. f) This work.

be provided in section 5.6.

The strongest gamma ray from the 6th excited state in ^{23}Mg is from the decay directly to the ground state. There is a second gamma ray from this state, with a relative intensity of about 59% [13], emitted in the transition from the 6th excited state to the 1st excited state. This peak in the spectrum from this dataset is shown in Figure 5.7. Looking forward, this peak could also be used to confirm the lifetime and excitation energy determined using the other peak.

5.3 Astrophysical State of Interest

The astrophysical state of interest at a literature excitation energy of 7784.7(8) keV [13] was investigated for two spin cases; $5/2^+$ and $7/2^+$. $3/2^+$ is also possible, but is covered by the $5/2^+$ case in this work due to the nearly identical alpha emission angle distributions produced using FRESCOX for the two cases. The experimental peak of interest as well as a sample fit of the model to the data is shown in Figure 5.8. The gamma spectrum shown was produced by gating on the alpha particles in groups 1-3 of the ΔE detector, with the energy gates used for each group given in Table 5.3.

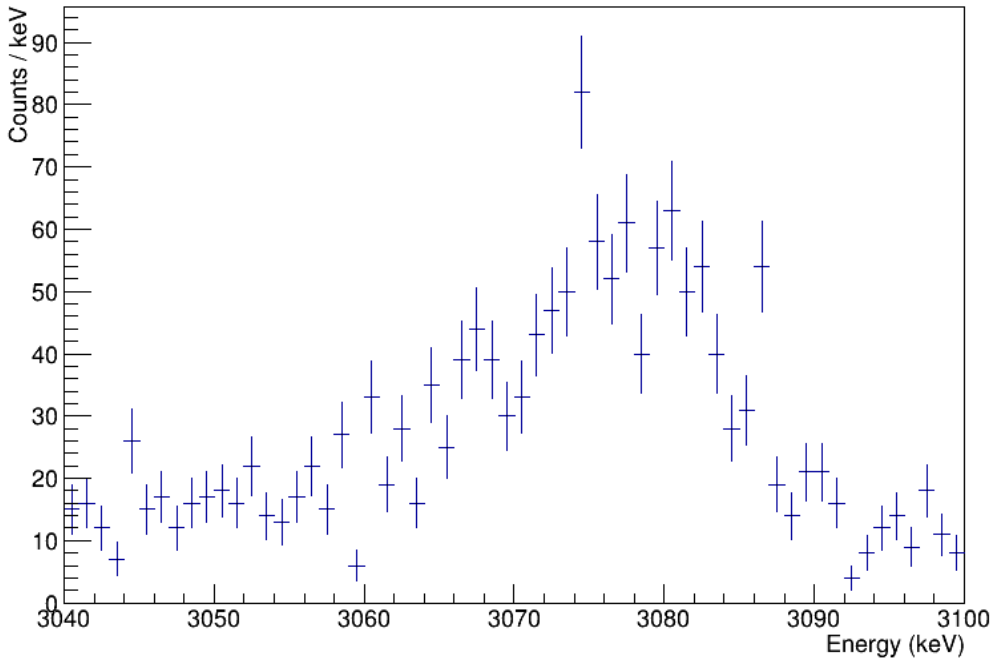

Figure 5.7 Gamma peak from the weaker transition from the 6th excited state in ^{23}Mg.

Group	Low Energy Bound (MeV)	High Energy Bound (MeV)
1	17.90	20.80
2	7.0	19.20
3	4.0	15.17

Table 5.3 High and low energy bounds of the gates applied to the total deposited energy of alpha particles corresponding to each group to produce the experimental spectrum for the state of astrophysical interest in ^{23}Mg.

The corner plot from the analysis assuming a spin and parity of $7/2^+$ is shown in Figure 5.9. Though the statistics were not good enough in this experiment to determine a finite value for the lifetime of the state, upper limits were able to be set. The 90% confidence level upper limit on the lifetime is < 18 fs, and the 95% confidence level upper limit is < 20 fs. The gamma ray energy determined in this case is $7331.4^{+4.2}_{-3.8}$ keV, corresponding to an excitation energy of $7783.4^{+4.2}_{-3.8}$ keV.

The analysis was also carried out assuming a spin and parity of $5/2^+$. As can be seen in Figure 5.10, the posterior distribution for the lifetime goes to 0 at lower lifetime value than in the $7/2^+$ case. However, upper limits were still set on the lifetime in this case. The 90% confidence level upper limit is < 13 fs, and the 95% confidence level upper limit is < 17 fs. The gamma ray energy

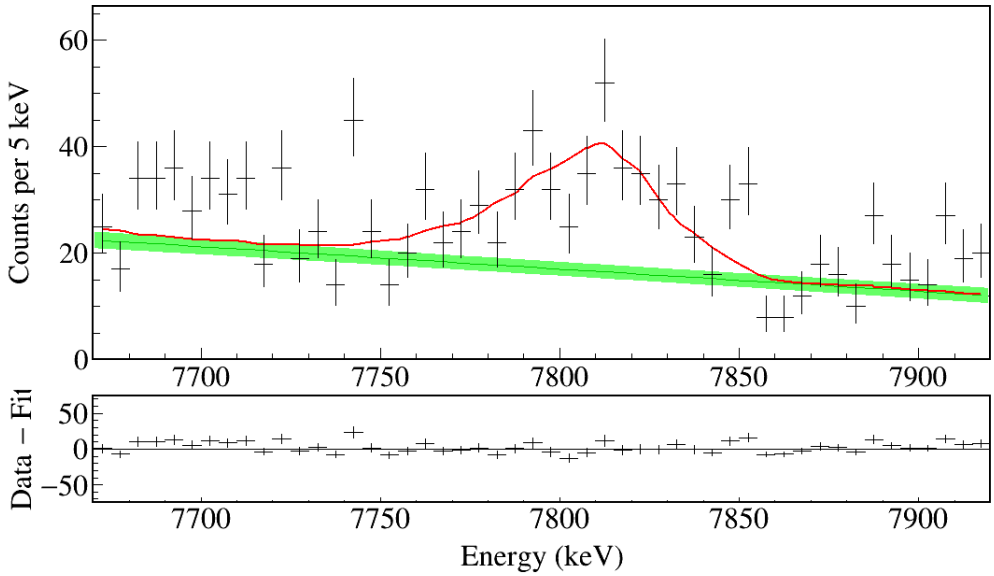

Figure 5.8 Scaled simulation plus sloped linear background fit to the experimental data for the gamma peak from the state of astrophysical interest in ^{23}Mg. The simulation assumes a lifetime of 5 fs, a gamma ray energy of 7334 keV, a spin and parity of $5/2^+$, and uses the default stopping power provided in GEANT4.

determined in this case is $7333.3^{+4.0}_{-2.3}$ keV, corresponding to an excitation energy of $7785.2^{+4.0}_{-2.3}$ keV.

Due to the limited statistics of the experiment, finite lifetime values were not able to be determined in either case, nor were the spin and parity cases distinguished by comparing angular distributions of alpha particles to FRESCOX outputs. The discrepancies between the two direct measurements of the resonance strength of the proton capture reaction, and between previous indirect and direct measurements still stand. Using the upper limits on the lifetime set in this work and the proton branching ratio to determine a resonance strength will result in a lower limit that is not discrepant with the direct measurements. However, further investigation into the lifetime with higher statistics to probe these limits is desirable. Redoing this experiment with full beam in the future could lend more sensitivity to the lifetime, gamma and excitation energies, and the spin of the state. The discrepant lifetimes measured for the 2nd and 6th excited states in ^{23}Mg also motivate another experiment with higher statistics.

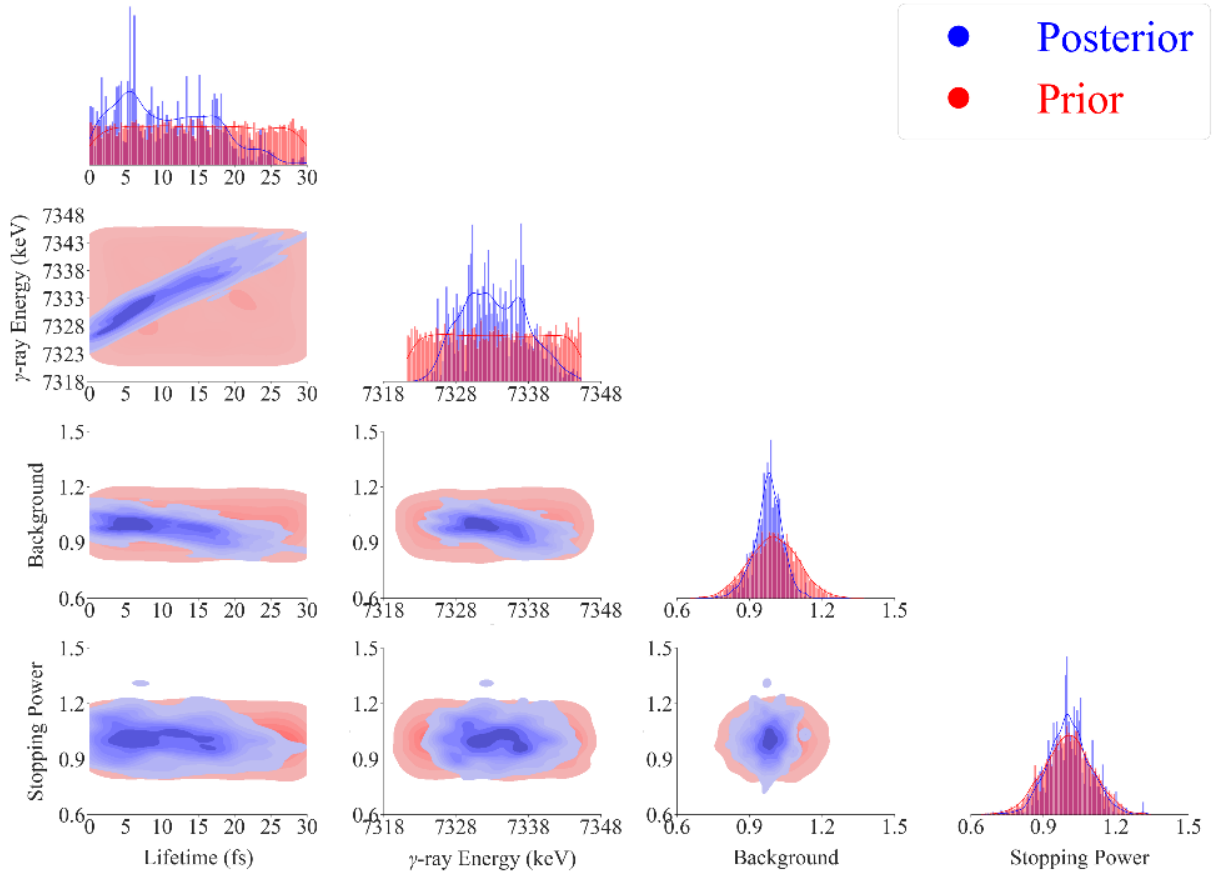

Figure 5.9 Corner plot output from the MCMC Bayesian analysis for the state of astrophysical interest in ^{23}Mg, assuming a spin and parity of $7/2^{+}$.

5.4 Table of Results

The results of this work are summarized and compared to literature values for the excitation energy E_x, gamma ray energy E_γ, and the lifetime τ, in Table 5.4.

5.5 Performance of DSL2

The experiment that used DSL1 to constrain the lifetime of the 7787 keV excited state to < 12 fs reported typical beam intensities of 1-2 $\times 10^{10}$ ions/s over an integrated beam time of 5 days [57]. This corresponds to a total number of incident ^{24}Mg ions of approximately 6.48 $\times 10^{15}$ ions. Integration of the beam current throughout the duration of experiment S2193 using DSL2, when taking into account the 5+ charge state of the ^{24}Mg, indicates a total number of ^{24}Mg delivered to the setup of approximately 2.49 $\times 10^{15}$ ions. When taking into account the fact that the analysis

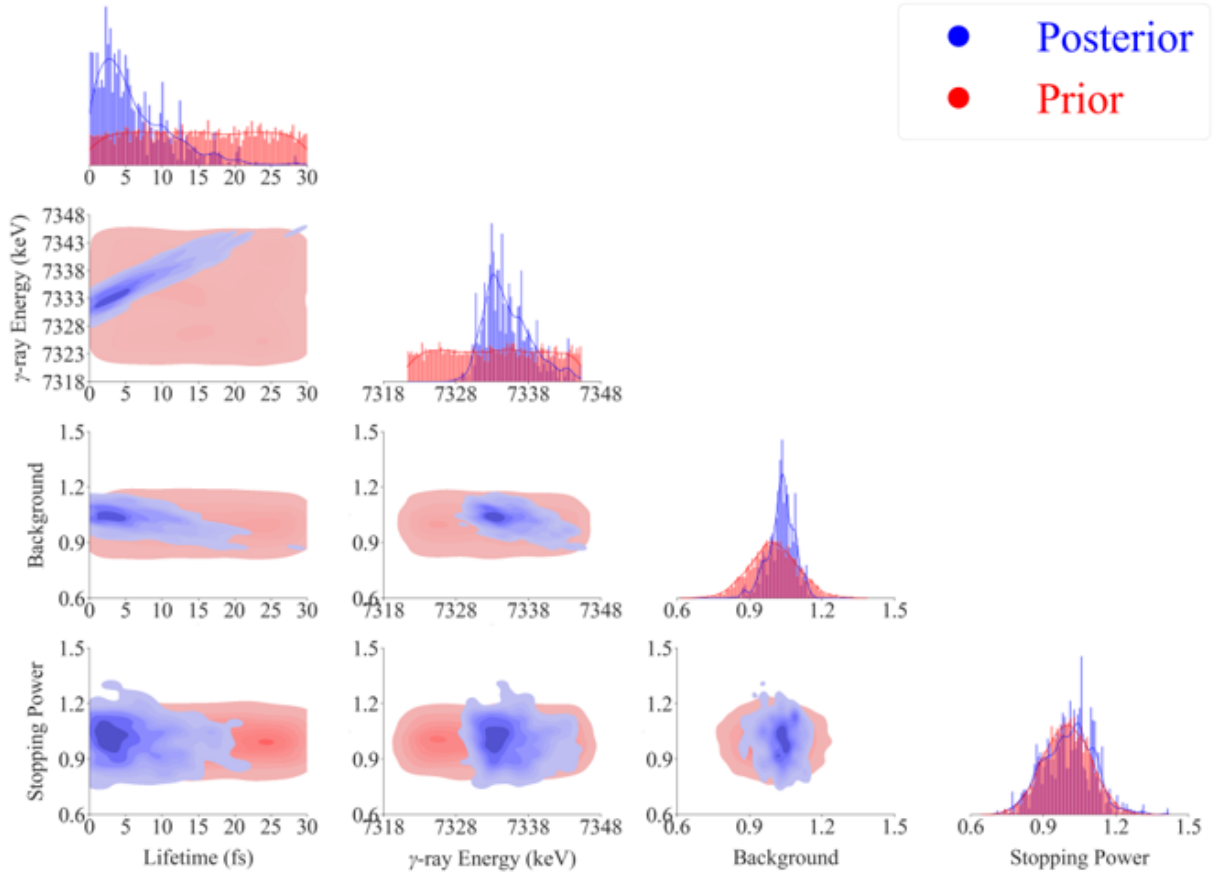

Figure 5.10 Corner plot output from the MCMC Bayesian analysis for the state of astrophysical interest in ^{23}Mg, assuming a spin and parity of $5/2^{+}$.

was performed on only the data taken on the target produced at TRIUMF, the effective amount of beam on target is reduced to approximately 9.57 $\times 10^{14}$ ions of ^{24}Mg.

Despite receiving around an order of magnitude less beam on target than the previous measurement of lifetimes of states in ^{23}Mg using the DSL1 iteration of the DSL setup, the sensitivities achieved by DSL2 are similar to that experiment. The wider acceptance of the Si detectors paired with the pixelation of the ΔE detector to account for kinematic broadening allows for the most to be made of the beam delivered. In the case of the state of astrophysical interest, the Si detector telescope is wide enough that it can accept every alpha particle produced associated with ^{23}Mg nuclei excited to the 7785 keV state.

Given the full beam intended for this experiment, the DSL2 setup would be able to set an upper

Literature [13]			Ref. [111]		This Work		
E_x (keV)	E_γ (keV)	τ (fs)	E_γ (keV)	τ (fs)	E_x (keV)	E_γ (keV)	τ (fs)
2051.6(4)	1601.4(13)	94(17)	1601.8(11), $1601.2^{+0.3}_{-0.5}$	78(19), 85(15)	$2048.2^{+0.8}_{-0.7}$	$1597.4^{+0.8}_{-0.7}$	52^{+14}_{-12}
2905.2(7)	2906.4(11)	15.0(30)	–	14^{+5}_{-6}, 12(5)	$2902.4^{+0.5}_{-0.5}$	$2902.2^{+0.5}_{-0.5}$	$6.0^{+1.5}_{-1.4}$
7784.7(8)	7333.2(11)	10.0(3.0)	$7333.0^{+0.5}_{-0.2}$ [38]	11^{+7}_{-5} [38]	$7785.2^{+4.0}_{-2.3}$ $(5/2^+)$ $7783.4^{+4.2}_{-3.8}$ $(7/2^+)$	$7333.3^{+4.0}_{-2.3}$ $7331.4^{+4.2}_{-3.8}$	< 13 < 18

Table 5.4 Compilation of the literature value and results from this work for the excitation energy, gamma ray energy, and lifetime of several states in ^{23}Mg. The limits on the lifetime of the astrophysical state of interest from this work presented in this table are 90% confidence level results. The results from a recently published thesis that have not been included in the literature evaluations are also included. For the 2nd and 6th excited states, the first value listed from this thesis was determined using DSAM, and the second value listed was determined using the emitter velocity method described in [111, 38] and section 1.8.2.3. The values from this thesis for the astrophysical state of interest were updated in a later paper, and these most recent results are presented in this table.

limit on the lifetime of the state of interest of < 4 fs, should the lifetime be that short. Otherwise, a finite determination of the lifetime is possible. The sensitivity to the angular distribution of the alpha particles would also lend itself to a deeper investigation into the spin of the state of interest, which could shed some light on the lingering discrepancies.

5.6 Mirror Asymmetries

Mirror nuclei are isobars that have mirrored numbers of nucleons. In the case of ^{23}Mg, which has 12 protons and 11 neutrons, its mirror nucleus ^{23}Na has 11 protons and 12 neutrons. Both share a total nucleon number of $A = 23$, but $Z_{^{23}\mathrm{Mg}} = N_{^{23}\mathrm{Na}}$ and $N_{^{23}\mathrm{Mg}} = Z_{^{23}\mathrm{Na}}$. Because the strong interaction is largely charge-independent, mirror nuclei should have a set of states that is nearly identical [116].

The transitions from low-lying bound nuclear states are dominated by electromagnetic decay. Assuming one type of decay, the lifetime of the state can be determined from the energy of the transition and the transition strength. The decay constant can be calculated following

$$\lambda(\overline{\omega}L) = \frac{8\pi(L+1)}{\hbar L[(2L+1)!!]^2}\left(\frac{E_\gamma}{\hbar c}\right)^{2L+1} B(\overline{\omega}L) \tag{5.1}$$

where $\overline{\omega}$ denotes either electric or magnetic radiation, L is the multipolarity of the radiation, E_γ is the energy of the gamma radiation, and $B(\overline{\omega}L)$ is the reduced transition probability, which contains the wave functions of the states involved [1]. The relationship between lifetime and the decay constant is defined as

$$\tau = \frac{1}{\lambda} \tag{5.2}$$

where τ is the lifetime. In reality, the transitions aren't always of one type, and can instead be mixed transitions. This complicates the relationship between the decay constant, the gamma ray energy, and the reduced transition probability.

Since states in mirror nuclei have the same wave functions to first order, the first several states in each nucleus should have similar transition strengths, leading to similar lifetimes. This also means similar half-lives, since half-life is simply the lifetime scaled by $ln(2)$. The first several states in ^{23}Mg and ^{23}Na exhibit fairly good mirror symmetry in their half-lives, as shown in Table 5.5. However, the literature values for the half-lives of the 2nd and 6th excited states are different by almost a factor of 3. The half-lives determined for these states in this experiment, also given in Table 5.5, resolve this asymmetry.

The literature values for these two states in ^{23}Mg come from only a small handful of measurements, and are thus not as well-established as those for ^{23}Na. The sensitivity to both excitation energy and lifetime provided by the MCMC-based Bayesian analysis used in this work suggests more accurate results for both values, thus resolving the asymmetry. In the future, these results could be used to determine the electromagnetic transition strengths for these states.

^{23}Mg					^{23}Na		
E_x (keV) [13]	J^π [13]	$t_{1/2}$ (fs) [13]	$t_{1/2}$ (fs) [111]	$t_{1/2}$ (fs) (this work)	E_x (keV) [13]	J^π [13]	$t_{1/2}$ (fs) [13]
450.7(15)	$\frac{5}{2}^+$	1150(800)	1123(243), 1109(76)		440.2(4)	$\frac{5}{2}^+$	1140(700)
2051.6(4)	$\frac{7}{2}^+$	65(12)	54(13), 59(10)	$36.3^{+10.0}_{-8.4}$	2076.2(4)	$\frac{7}{2}^+$	27(3)
2357.0(7)	$\frac{1}{2}^+$	575(118)			2390.0(3)	$\frac{1}{2}^+$	600(140)
2714.5(5)	$\frac{9}{2}^+$	65(8)			2640.5(6)	$\frac{1}{2}^-$	76(9)
2771.2(7)	$\frac{1}{2}^-$	75(10)			2703.8(5)	$\frac{9}{2}^+$	88(7)
2905.2(7)	$\frac{3}{2}^+$	10.4(21)	10(3), 8(3)	$4.2^{+1.0}_{-1.0}$	2982.0(5)	$\frac{3}{2}^+$	3.3(4)
3794.1(4)	$\frac{3}{2}^-$	28.4(42)	<30, 28^{+4}_{-5}		3677.9(5)	$\frac{3}{2}^-$	21(3)

Table 5.5 Excitation energy, spin and parity, and half-live for the first seven excited states in ^{23}Mg and ^{23}Na. The grey-shaded boxes indicate the asymmetric half-lives. The results from a recently published thesis that have not been included in the literature evaluations are also included. The first value listed from this thesis was determined using DSAM, and the second value listed was determined using the emitter velocity method described in [111, 38] and section 1.8.2.3.

CHAPTER 6

SUMMARY AND OUTLOOK

The decay of ^{22}Na produced in novae is of particular interest in contemporary nuclear astrophysics. The 2.6 year half life on its beta decay to the first excited state in ^{22}Ne and the subsequent emission of a 1275 keV gamma ray lends itself to association with the site that produced it, were it to be detected. Previous missions have searched for this gamma ray, but save for one questionable potential detection, have only been able to set limits on the amount of ^{22}Na that could be ejected from a nova due to non-detection.

The next generation of space-based gamma ray telescopes project an increased sensitivity of at least an order of magnitude for the 1275 keV gamma line. As COSI begins taking data in the next few years, and as other future missions like e-ASTROGAM join, the detection of evidence of ^{22}Na decay may occur. Even if these missions set more limits on the amount of ^{22}Na that is ejected from a nova due to non-detection, these limits should be more constraining and will improve understanding of nova nucleosynthesis.

The reactions that produce ^{22}Na during the thermonuclear runaway of a nova are well constrained, but there is uncertainty in the rate of the proton capture reaction that dominates the destruction of ^{22}Na in these conditions. This leads to uncertainty in model predictions of how much ^{22}Na will be ejected. Previous experiments have determined that this reaction is dominated by a single resonance at peak nova temperatures, corresponding to a proton energy of 213 keV and the 7787 keV excited state in the ^{23}Mg produced. Direct measurements of the strength of this resonance, which are needed to calculate the reaction rate, are discrepant. Indirect measurements, which use the spin, lifetime, and excitation energy of the associated state in ^{23}Mg as well as the proton branching ratio to calculate the resonance strength, are further discrepant from the direct measurements.

The DSL setup was recently upgraded from DSL1 to DSL2. The main upgrade involved replacing the 150 mm^2 active area Si detector telescope with a new Si detector telescope utilizing detectors each with an active area of 2450 mm^2 and associated front-end electronics. The ΔE

detector, which consisted of only a single channel in DSL1, is a 16×16 strip pixilated detector in the DSL2 setup. The first experiment using the DSL2 setup ran at TRIUMF in December of 2022, and aimed to do a new lifetime measurement of the state of astrophysical interest in ^{23}Mg using DSAM. This work

Despite not receiving the full beam expected for the experiment, the DSL2 setup performed well. This experiment received less beam than the previous ^{23}Mg lifetime measurement done with the DSL1 setup, and one of the ^{3}He-implanted Au foil targets used had a large amount of surface contamination. Despite these factors, the analysis of the data taken in this experiment resulted in limits on the lifetime of the state of interest on par with the sensitivity of the results from the previous measurement using DSL1. This experiment also resulted in a potential resolution of a mirror asymmetry in the half-lives of two low lying states in ^{23}Mg and ^{23}Na. This is of interest to nuclear structure studies, and may be relevant to resolving some of the nuclear data discrepancies associated with the state of astrophysical interest.

There is still a discrepancy between the direct and indirect measurements of the strength of the key resonance that dominates the ^{22}Na$(p,\gamma)^{23}$Mg reaction at peak nova temperatures when the finite determinations of the lifetime of the state of interest are used in the indirect calculations. The upper limits on the lifetime determined in this work and in [57] result in lower limits on the resonance strength, which resolves the discrepancy with all direct measurements. A rerun of the experiment outlined in this work with full beam could provide more information on the lifetime of the state of interest, further constraining the resonance strength. The overall uncertainty in the resonance strength leads to uncertainty in the amount of ^{22}Na that is ejected from a nova.

Looking forward, DSL2's sensitivity to the angular distribution of alpha particles emitted in the ^{3}He(^{24}Mg,α)^{23}Mg reaction investigating the aforementioned resonance strength can be used to further investigate the spin of the state of astrophysical interest. Were the experiment discussed in this work to be completed with the full beam expected sometime in the future, it is possible that a distinction could be made between the $3/2^{+}$ and $5/2^{+}$, and $7/2^{+}$ potential spins, as well as potential population of the nearby $11/2^{+}$ state by comparison with model calculations such as those done

with FRESCO in this work. Increased statistics would also lead to more sensitivity in the lifetime and excitation/gamma energy values determined, which could also provide more information on the state populated. Given high enough statistics, the weaker gamma-ray transition from the state of interest could be investigated to confirm the values determined using the stronger transition.

Additionally, another direct measurement of the resonance strength using a setup other than DSL could provide valuable insight about the ^{22}Na$(p,\gamma)^{23}$Mg reaction. A measurement could be done in inverse kinematics using a recoil separator, as opposed to another measurement with a radioactive ^{22}Na target. Considering there are only two direct measurements, and one determined the resonance strength relative to other resonances rather than absolutely, an additional measurement may improve model estimates of nova yields of ^{22}Na and could help resolve the standing discrepancy.

As for the future of DSL2, a second experiment using the setup has been approved at TRIUMF. Experiment S2373 will use the 140 μm ΔE detector to measure lifetimes in ^{31}S, including the lifetime of the key resonance in the ^{30}P$(p,\gamma)^{31}$S reaction, which acts as a bottleneck to nucleosynthetic flow to higher masses. DSL1 was previously used to investigate this reaction, but results were limited by the sensitivity of the setup [68]. The MCMC-based Bayesian analytical tools developed by the DSL collaboration for analysis of DSAM data will continue to be refined for future experiments and their analyses.

BIBLIOGRAPHY

[1] Christian Iliadis. *Nuclear Physics of Stars [electronic resource]*. John Wiley Sons Incorporated, 2015. URL: https://ezproxy.msu.edu/login?url=https://onlinelibrary.wiley.com/doi/book/10.1002/9783527692668.

[2] *Overview - NASA Science — science.nasa.gov*. https://science.nasa.gov/universe/overview/. [Accessed 04-05-2026].

[3] Taotao Fang and Renyue Cen. "The Transition from Population III to Population II Stars". In: *The Astrophysical Journal* 616.2 (Nov. 2004), p. L87. DOI: 10.1086/426786.

[4] Ralf S. Klessen and Simon C. O. Glover. "The First Stars: Formation, Properties, and Impact". In: 61 (Aug. 2023), pp. 65–130. DOI: 10.1146/annurev-astro-071221-053453. arXiv: 2303.12500 [astro-ph.CO].

[5] Meng Wang et al. "The AME 2020 atomic mass evaluation (II). Tables, graphs and references*". In: *Chinese Physics C* 45.3 (Mar. 2021), p. 030003. DOI: 10.1088/1674-1137/abddaf.

[6] Laura Chomiuk, Brian D. Metzger, and Ken J. Shen. "New Insights into Classical Novae". In: *Annual Review of Astronomy and Astrophysics* 59.Volume 59, 2021 (2021), pp. 391–444. ISSN: 1545-4282. DOI: https://doi.org/10.1146/annurev-astro-112420-114502.

[7] Sidney van den Bergh and Gustav A. Tammann. "Galactic and extragalactic supernova rates." In: 29 (Jan. 1991), pp. 363–407. DOI: 10.1146/annurev.aa.29.090191.002051.

[8] D Koester and G Chanmugam. "Physics of white dwarf stars". In: *Reports on Progress in Physics* 53.7 (July 1990), p. 837. DOI: 10.1088/0034-4885/53/7/001.

[9] S. Starrfield, C. Iliadis, and W. R. Hix. "The Thermonuclear Runaway and the Classical Nova Outburst". In: 128.963 (May 2016), p. 051001. DOI: 10.1088/1538-3873/128/963/051001. arXiv: 1605.04294 [astro-ph.SR].

[10] Jordi José et al. "Classical and Recurrent Nova Models". In: *Binary Paths to Type Ia Supernovae Explosions*. Ed. by Rosanne Di Stefano, Marina Orio, and Maxwell Moe. Vol. 281. IAU Symposium. Jan. 2013, pp. 80–87. DOI: 10.1017/S1743921312014743.

[11] R.B. Firestone. "Nuclear Data Sheets for A = 21". In: *Nuclear Data Sheets* 127 (2015), pp. 1–68. ISSN: 0090-3752. DOI: https://doi.org/10.1016/j.nds.2015.07.001.

[12] M. Shamsuzzoha Basunia. "Nuclear Data Sheets for A = 22". In: *Nuclear Data Sheets* 127 (2015), pp. 69–190. ISSN: 0090-3752. DOI: https://doi.org/10.1016/j.nds.2015.07.002.

[13] M. Shamsuzzoha Basunia and A. Chakraborty. "Nuclear Data Sheets for A=23". In: *Nuclear Data Sheets* 171 (2021), pp. 1–252. ISSN: 0090-3752. DOI: https://doi.org/10.1016/j.nds.2020.12.001.

[14] Jordi José, Alain Coc, and Margarita Hernanz. "Nuclear Uncertainties in the NeNa-MgAl Cycles and Production of 22Na and 26Al during Nova Outbursts". In: *The Astrophysical Journal* 520.1 (July 1999), p. 347. DOI: 10.1086/307445.

[15] Stan Woosley and Thomas Janka. "The physics of core-collapse supernovae". In: *Nature Physics* 1.3 (2005), pp. 147–154.

[16] S E Woosley and T A Weaver. *The evolution and explosion of massive Stars II: Explosive hydrodynamics and nucleosynthesis*. Tech. rep. Lawrence Livermore National Lab., CA (United States), Aug. 1995. DOI: 10.2172/115557.

[17] Marco Pignatari et al. "Production of Radioactive 22Na in Core-collapse Supernovae: The Ne-E(L) Component in Presolar Grains and Its Possible Consequences on Supernova Observations". In: *The Astrophysical Journal* 990.1 (Aug. 2025), p. 19. DOI: 10.3847/1538-4357/adef4c.

[18] Sachiko Amari. "SODIUM-22 FROM SUPERNOVAE: A METEORITE CONNECTION". in: *The Astrophysical Journal* 690.2 (Dec. 2008), p. 1424. DOI: 10.1088/0004-637X/690/2/1424.

[19] Falk Herwig. "Evolution of Asymptotic Giant Branch Stars". In: *Annual Review of Astronomy and Astrophysics* 43.Volume 43, 2005 (2005), pp. 435–479. ISSN: 1545-4282. DOI: https://doi.org/10.1146/annurev.astro.43.072103.150600.

[20] Smithsonian National Museum of Natural History. *Mineral Sciences Collections Search*. http://n2t.net/ark:/65665/3571c4d5f-375f-4cc1-b8d1-406ad2fe49ac. [Accessed 20-05-2026].

[21] V.S. Heber, R.C. Wiens, and D.B. et al. Reisenfeld. "The Genesis Solar Wind Concentrator Target: Mass Fractionation Characterised by Neon Isotopes". In: *Space Sci. Rev* 130 (2007), pp. 309–316. DOI: https://doi.org/10.1007/s11214-007-9179-1.

[22] Reika Yokochi and Bernard Marty. "A determination of the neon isotopic composition of the deep mantle". In: *Earth and Planetary Science Letters* 225.1 (2004), pp. 77–88. ISSN: 0012-821X. DOI: https://doi.org/10.1016/j.epsl.2004.06.010.

[23] C.D. Williams and S. Mukhopadhyay. "Capture of nebular gases during Earth's accretion is preserved in deep-mantle neon". In: *Nature* 565 (2019), pp. 78–81. DOI: https://doi.org/10.1038/s41586-018-0771-1.

[24] P. Eberhardt et al. "A neon-E rich phase in Orgueil: results obtained on density separates".

In: *Geochimica et Cosmochimica Acta* 45.9 (1981), pp. 1515–1528. ISSN: 0016-7037. DOI: https://doi.org/10.1016/0016-7037(81)90282-9.

[25] W. A. Mahoney et al. "The HEAO 3 gamma-ray spectrometer." In: *Nuclear Instruments and Methods* 178 (Jan. 1980), pp. 363–381. DOI: 10.1016/0029-554X(80)90815-0.

[26] W. A. Mahoney et al. "Diffuse galactic gamma-ray line emission from nucleosynthetic Fe-60, Al-26, and Na-22 - Preliminary limits from HEAO 3." In: 262 (Nov. 1982), pp. 742–748. DOI: 10.1086/160469.

[27] W. A. Mahoney et al. "HEAO 3 discovery of Al-26 in the interstellar medium". In: 286 (Nov. 1984), pp. 578–585. DOI: 10.1086/162632.

[28] M.S. Basunia and A.M. Hurst. "Nuclear Data Sheets for A = 26". In: *Nuclear Data Sheets* 134 (2016), pp. 1–148. ISSN: 0090-3752. DOI: https://doi.org/10.1016/j.nds.2016.04.001.

[29] Nikos Prantzos and Roland Diehl. "Radioactive 26Al in the galaxy: observations versus theory". In: *Physics Reports* 267.1 (1996), pp. 1–69. ISSN: 0370-1573. DOI: https://doi.org/10.1016/0370-1573(95)00055-0.

[30] Jordi José and Margarita Hernanz. "Nucleosynthesis in classical nova explosions". In: *Journal of Physics G: Nuclear and Particle Physics* 34.12 (Oct. 2007), R431. DOI: 10.1088/0954-3899/34/12/R01.

[31] A. F. Iyudin et al. "Study of nova-produced 22Na with COMPTEL". in: *AIP Conference Proceedings* 510.1 (Apr. 2000), pp. 92–96. ISSN: 0094-243X. DOI: 10.1063/1.1303181.

[32] A. F. Iyudin et al. "Study of the nova-produced ^{22}Na with COMPTEL". in: *Exploring the Gamma-Ray Universe*. Ed. by A. Gimenez, V. Reglero, and C. Winkler. Vol. 459. ESA Special Publication. Sept. 2001, pp. 41–46.

[33] AF Iyudin. "Observation of line emission of the isotope 22Na from a classical nova". In: *Astronomy reports* 54.7 (2010), pp. 611–619.

[34] G. Vedrenne et al. "SPI: The spectrometer aboard INTEGRAL". in: 411 (Nov. 2003), pp. L63–L70. DOI: 10.1051/0004-6361:20031482.

[35] Siegert, Thomas et al. "Nucleosynthesis constraints through -ray line measurements from classical novae - Hierarchical model for the ejecta of 22Na and 7Be". In: *AA* 650 (2021), A187. DOI: 10.1051/0004-6361/202140300.

[36] John A. Tomsick et al. *The Compton Spectrometer and Imager*. 2023. arXiv: 2308.12362 [astro-ph.HE]. URL: https://arxiv.org/abs/2308.12362.

[37] A. De Angelis et al. "Science with e-ASTROGAM". in: *Journal of High Energy Astrophysics* 19 (Aug. 2018), pp. 1–106. ISSN: 2214-4048. DOI: 10.1016/j.jheap.2018.07.001.

[38] Chloé Fougères et al. "Search for 22Na in novae supported by a novel method for measuring femtosecond nuclear lifetimes". In: *Nature communications* 14.1 (2023), p. 4536.

[39] S. Seuthe et al. "Resonances in the 22Na(p,)23Mg reaction". In: *Nuclear Physics A* 514.3 (1990), pp. 471–502. ISSN: 0375-9474. DOI: https://doi.org/10.1016/0375-9474(90)90153-D.

[40] Michael Wiescher and K Langanke. "The proton capture reactions on21Na and22Na under hydrogen burning conditions". In: *Zeitschrift für Physik A Atomic Nuclei* 325.3 (1986), pp. 309–315.

[41] J. Görres et al. "Search for resonances in the ^{22}Na(p,γ)^{23}Mg reaction". In: *Phys. Rev. C* 39 (1 Jan. 1989), pp. 8–13. DOI: 10.1103/PhysRevC.39.8.

[42] F. Stegmüller et al. "22Na(p,)23Mg resonant reaction at low energies". In: *Nuclear Physics A* 601.2 (1996), pp. 168–180. ISSN: 0375-9474. DOI: https://doi.org/10.1016/0375-9474(96)00084-X.

[43] A. L. Sallaska et al. "Direct Measurements of ^{22}Na$(p,\gamma)^{23}$Mg Resonances and Consequences for ^{22}Na Production in Classical Novae". In: *Phys. Rev. Lett.* 105 (15 Oct. 2010), p. 152501. DOI: 10.1103/PhysRevLett.105.152501.

[44] A. L. Sallaska et al. "Absolute determination of the ^{22}Na$(p,\gamma)^{23}$Mg reaction rate in novae". In: *Phys. Rev. C* 83 (3 Mar. 2011), p. 034611. DOI: 10.1103/PhysRevC.83.034611.

[45] S. Schmidt et al. "22Na(3He,d)23Mg reaction studies of states near the proton threshold and hydrogen burning of 22Na". In: *Nuclear Physics A* 591.2 (1995), pp. 227–243. ISSN: 0375-9474. DOI: https://doi.org/10.1016/0375-9474(95)00164-V.

[46] D. G. Jenkins et al. "Reevaluation of the ^{22}Na(p,γ) Reaction Rate: Implications for the Detection of ^{22}Na Gamma Rays from Novae". In: *Phys. Rev. Lett.* 92 (3 Jan. 2004), p. 031101. DOI: 10.1103/PhysRevLett.92.031101.

[47] D. G. Jenkins et al. "γ-ray spectroscopy of the $A = 23$, $T = 1/2$ nuclei ^{23}Na and ^{23}Mg: High-spin states, mirror symmetry, and applications to nuclear astrophysical reaction rates". In: *Phys. Rev. C* 87 (6 June 2013), p. 064301. DOI: 10.1103/PhysRevC.87.064301.

[48] A. Saastamoinen et al. "Experimental study of β-delayed proton decay of ^{23}Al for nucleosynthesis in novae". In: *Phys. Rev. C* 83 (4 Apr. 2011), p. 045808. DOI: 10.1103/PhysRevC.83.045808.

[49] Vandana Tripathi et al. "Split Isobaric Analog State in ^{55}Ni: Case of Strong Isospin Mixing". In: *Phys. Rev. Lett.* 111 (26 Dec. 2013), p. 262501. DOI: 10.1103/PhysRevLett.111.262501.

[50] V. E. Iacob et al. "β decay of proton-rich nucleus ^{23}Al and astrophysical consequences". In: *Phys. Rev. C* 74 (4 Oct. 2006), p. 045810. DOI: 10.1103/PhysRevC.74.045810.

[51] Yongjun Zhai. "The structure of 23Al and astrophysical consequences". PhD thesis. Texas A-M, 2009.

[52] MS Kwag et al. "Spin assignments for 23 Mg levels and the astrophysical 22 Na (p, γ) 23 Mg reaction". In: *The European Physical Journal A* 56.4 (2020), p. 108.

[53] Fougères, C. et al. "Understanding the cosmic abundance of 22Na: Lifetime measurements in 23Mg". In: *EPJ Web Conf.* 279 (2023), p. 09001. DOI: 10.1051/epjconf/202327909001.

[54] R. J. Tighe et al. "Observation of strong isospin mixing in proton emission from the astrophysically interesting isobaric analog state in ^{23}Mg". In: *Phys. Rev. C* 52 (5 Nov. 1995), R2298(R)–R2301(R). DOI: 10.1103/PhysRevC.52.R2298.

[55] M. Friedman et al. "Low-energy ^{23}Al β-delayed proton decay and ^{22}Na destruction in novae". In: *Phys. Rev. C* 101 (5 May 2020), 052802(R). DOI: 10.1103/PhysRevC.101.052802.

[56] K. Peräjärvi et al. "Measurement of the IAS resonance strength in 23Mg". In: *Physics Letters B* 492.1 (2000), pp. 1–7. ISSN: 0370-2693. DOI: https://doi.org/10.1016/S0370-2693(00)01074-1.

[57] O. S. Kirsebom et al. "Measurement of lifetimes in ^{23}Mg". In: *Phys. Rev. C* 93 (2 Feb. 2016), p. 025802. DOI: 10.1103/PhysRevC.93.025802.

[58] D.B. Fossan and E.K. Warburton. "VII.H - Lifetime Measurements". In: *Nuclear Spectroscopy and Reactions, Part C*. ed. by JOSEPH CERNY. Vol. 40. Pure and Applied Physics. Elsevier, 1974, pp. 307–374. DOI: https://doi.org/10.1016/B978-0-12-165203-6.50013-1.

[59] J. C. Hardy et al. "Nuclear Lifetimes in the Region of 10^{-16} sec Measured by a New Technique". In: *Phys. Rev. Lett.* 37 (3 July 1976), pp. 133–136. DOI: 10.1103/PhysRevLett.37.133.

[60] L. J. Sun et al. "Extension of the particle x-ray coincidence technique: The lifetimes and branching ratios apparatus". In: *Phys. Rev. C* 111 (5 May 2025), p. 055806. DOI: 10.1103/PhysRevC.111.055806.

[61] D. Branford and I.F. Wright. "A doppler shift attenuation method for measuring lifetimes in the range 10131015S using heavy-ion induced reactions". In: *Nuclear Instruments and Methods* 106.3 (1973), pp. 437–443. ISSN: 0029-554X. DOI: https://doi.org/10.1016/0029-554X(73)90304-2.

[62] Glenn F. Knoll. *Radiation Detection and Measurement, 3rd ed.* 3rd edition. New York: John Wiley and Sons, 2000. ISBN: 978-0-471-07338-3, 978-0-471-07338-3.

[63] B. Davids. "The doppler shift lifetimes facility." In: *Hyperfine Interact* 225 (2014), pp. 215–218.

[64] B. Davids. "Outstanding problems in nuclear astrophysics: recent progress at TRIUMF". in: *AIP Advances* 4.4 (Jan. 2014), p. 041003. ISSN: 2158-3226. DOI: 10.1063/1.4864061.

[65] R. Kanungo et al. "Lifetime of ^{19}Ne*(4.03 MeV)". in: *Phys. Rev. C* 74 (4 Oct. 2006), p. 045803. DOI: 10.1103/PhysRevC.74.045803.

[66] S. Mythili et al. "Lifetimes of states in ^{19}Ne above the ^{15}O+α breakup threshold". In: *Phys. Rev. C* 77 (3 Mar. 2008), p. 035803. DOI: 10.1103/PhysRevC.77.035803.

[67] N. Galinski et al. "Lifetime measurements of states in ^{15}O". In: *Phys. Rev. C* 90 (3 Sept. 2014), p. 035803. DOI: 10.1103/PhysRevC.90.035803.

[68] L.J. Sun et al. "First application of Markov chain Monte Carlo-based Bayesian data analysis to the Doppler-shift attenuation method". In: *Physics Letters B* 839 (2023), p. 137801. ISSN: 0370-2693. DOI: https://doi.org/10.1016/j.physletb.2023.137801.

[69] Cathleen Fry. "Experimental constraints on nucleosynthesis in Oxygen-Neon novae". PhD thesis. Michigan State University, 2018.

[70] A.B. Garnsworthy et al. "The GRIFFIN facility for Decay-Spectroscopy studies at TRIUMF-ISAC". in: *Nuclear Instruments and Methods in Physics Research Section A: Accelerators, Spectrometers, Detectors and Associated Equipment* 918 (2019), pp. 9–29. ISSN: 0168-9002. DOI: https://doi.org/10.1016/j.nima.2018.11.115.

[71] F. Pászti et al. "Investigations on blistering and exfoliation in gold by 3.52 MeV helium ions". In: *Journal of Nuclear Materials* 98.1 (1981), pp. 11–17. ISSN: 0022-3115. DOI: https://doi.org/10.1016/0022-3115(81)90382-2.

[72] *GRIFFIN Collaboration - DAQ — griffin.triumf.ca*. https://griffin.triumf.ca/daq.html. [Accessed 08-06-2026].

[73] *Introduction - MidasWiki — daq00.triumf.ca*. https://daq00.triumf.ca/{M}idas{W}iki/index.php/{I}ntroduction. [Accessed 08-06-2026]. 2023.

[74] K. Jayamanna et al. "Off-line ion source terminal for ISAC at TRIUMFa)". In: *The Review of scientific instruments* 79 (Mar. 2008), p. 02C711. DOI: 10.1063/1.2816928.

[75] S. Koscielniak et al. "Beam dynamics studies on the ISAC RFQ at TRIUMF". in: *Proceedings of the 1997 Particle Accelerator Conference (Cat. No.97CH36167)*. Vol. 1. 1997, 1102–1104 vol.1. DOI: 10.1109/PAC.1997.749942.

[76] RE Laxdal. "ISAC-I and ISAC-II at TRIUMF: Achieved performance and new construction". In: *Proceedings of LINAC*. 2002, p. 296.

[77] K Jayamanna. "Off line ion source terminal". In: *Hyperfine Interactions* 225.1 (2014), pp. 51–62.

[78] *ISAC (Isotope Separator and ACcelerator) - Delivery Wiki — delivery.wiki.triumf.ca*. https://delivery.wiki.triumf.ca/w/index.php?title={I}{S}{A}{C}_({I}sotope_{S}eparator_and_{A}{C}celerator). [Accessed 08-06-2026]. 2021.

[79] *File:Test-isacii-06segment.jpg - Delivery Wiki — delivery.wiki.triumf.ca*. https://delivery.wiki.triumf.ca/w/index.php?title={F}ile:{T}est-isacii-06segment.jpg#filelinks. [Accessed 08-06-2026]. 2007.

[80] E. Browne and J.K. Tuli. "Nuclear Data Sheets for A = 235". In: *Nuclear Data Sheets* 122 (2014), pp. 205–292. ISSN: 0090-3752. DOI: https://doi.org/10.1016/j.nds.2014.11.002.

[81] M.S. Basunia. "Nuclear Data Sheets for A = 237". In: *Nuclear Data Sheets* 107.8 (2006), pp. 2323–2422. ISSN: 0090-3752. DOI: https://doi.org/10.1016/j.nds.2006.07.001.

[82] C. Morse. "Nuclear Structure and Decay Data for A=240". In: *Nuclear Data Sheets* 206 (2025), pp. 359–467. ISSN: 0090-3752. DOI: https://doi.org/10.1016/j.nds.2025.11.002.

[83] Y.A. Akovali. "Review of Alpha–Decay Data from Doubly–Even Nuclei". In: *Nuclear Data Sheets* 84.1 (1998), pp. 1–114. ISSN: 0090-3752. DOI: https://doi.org/10.1006/ndsh.1998.0009.

[84] Y.A. AKOVALI. "Nuclear Data Sheets for A = 226". In: *Nuclear Data Sheets* 77.2 (1996), pp. 433–470. ISSN: 0090-3752. DOI: https://doi.org/10.1006/ndsh.1996.0005.

[85] D.R. Tilley, H.R. Weller, and C.M. Cheves. "Energy levels of light nuclei A = 16–17". In: *Nuclear Physics A* 564.1 (1993), pp. 1–183. ISSN: 0375-9474. DOI: https://doi.org/10.1016/0375-9474(93)90073-7.

[86] Xiaolong Huang and Chunmei Zhou. "Nuclear Data Sheets for A=197". In: *Nuclear Data*

Sheets 104.2 (2005), pp. 283–426. ISSN: 0090-3752. DOI: https://doi.org/10.1016/j.nds.2005.01.001.

[87] John Cameron et al. "Nuclear Data Sheets for A = 37". In: *Nuclear Data Sheets* 113.2 (2012), pp. 365–514. ISSN: 0090-3752. DOI: https://doi.org/10.1016/j.nds.2012.02.001.

[88] Jun Chen, John Cameron, and Balraj Singh. "Nuclear Data Sheets for A = 35". In: *Nuclear Data Sheets* 112.11 (2011), pp. 2715–2850. ISSN: 0090-3752. DOI: https://doi.org/10.1016/j.nds.2011.10.001.

[89] M. Shamsuzzoha Basunia. "Nuclear Data Sheets for A = 28". In: *Nuclear Data Sheets* 114.10 (2013), pp. 1189–1291. ISSN: 0090-3752. DOI: https://doi.org/10.1016/j.nds.2013.10.001.

[90] O.B. Tarasov and D. Bazin. "LISE++: Radioactive beam production with in-flight separators". In: *Nuclear Instruments and Methods in Physics Research Section B: Beam Interactions with Materials and Atoms* 266.19 (2008). Proceedings of the XVth International Conference on Electromagnetic Isotope Separators and Techniques Related to their Applications, pp. 4657–4664. ISSN: 0168-583X. DOI: https://doi.org/10.1016/j.nimb.2008.05.110.

[91] A. Gavron. "Statistical model calculations in heavy ion reactions". In: *Phys. Rev. C* 21 (1 Jan. 1980), pp. 230–236. DOI: 10.1103/PhysRevC.21.230.

[92] LISE++ Team. *LISE++*. URL: https://lise.frib.msu.edu/lise.html.

[93] S. Agostinelli et al. "Geant4—a simulation toolkit". In: *Nuclear Instruments and Methods in Physics Research Section A: Accelerators, Spectrometers, Detectors and Associated Equipment* 506.3 (2003), pp. 250–303. ISSN: 0168-9002. DOI: https://doi.org/10.1016/S0168-9002(03)01368-8.

[94] J. Allison et al. "Recent developments in Geant4". In: *Nuclear Instruments and Methods in Physics Research Section A: Accelerators, Spectrometers, Detectors and Associated Equipment* 835 (2016), pp. 186–225. ISSN: 0168-9002. DOI: https://doi.org/10.1016/j.nima.2016.06.125.

[95] James F. Ziegler, M.D. Ziegler, and J.P. Biersack. "SRIM – The stopping and range of ions in matter (2010)". In: *Nuclear Instruments and Methods in Physics Research Section B: Beam Interactions with Materials and Atoms* 268.11 (2010). 19th International Conference on Ion Beam Analysis, pp. 1818–1823. ISSN: 0168-583X. DOI: https://doi.org/10.1016/j.nimb.2010.02.091.

[96] ICRU Report 73. "Stopping of Ions Heavier than Helium". In: *Journal of the ICRU* 5.1 (2005), pp. 1–1. DOI: 10.1093/jicru_ndi001.

[97] W.J. Huang et al. "The AME 2020 atomic mass evaluation (I). Evaluation of input data, and adjustment procedures*". In: *Chinese Physics C* 45.3 (Mar. 2021), p. 030002. DOI: 10.1088/1674-1137/abddb0.

[98] Ian Thompson. *Fresco — fresco.org.uk*. https://www.fresco.org.uk/index.htm. [Accessed 19-05-2026]. 2025.

[99] R.W. Zurmühle and C.M. Fou. "Optical-potential parameters for 3He". In: *Nuclear Physics A* 129.3 (1969), pp. 502–512. ISSN: 0375-9474. DOI: https://doi.org/10.1016/0375-9474(69)90697-6.

[100] N. Olsson et al. "Microscopic and conventional optical model analysis of neutron elastic scattering at 21.6 MeV over a wide mass range". In: *Nuclear Physics A* 472.2 (1987), pp. 237–268. ISSN: 0375-9474. DOI: https://doi.org/10.1016/0375-9474(87)90209-0.

[101] Thomas Bayes. "LII. An essay towards solving a problem in the doctrine of chances. By the late Rev. Mr. Bayes, F. R. S. communicated by Mr. Price, in a letter to John Canton, A. M. F. R. S". in: *Philosophical Transactions* 53 (Dec. 1763), pp. 370–418. ISSN: 0260-7085. DOI: 10.1098/rstl.1763.0053.

[102] Cade R. Rodgers and Christian Iliadis. "On the analysis of signal peaks in pulse-height spectra". In: *Nuclear Instruments and Methods in Physics Research Section A: Accelerators, Spectrometers, Detectors and Associated Equipment* 998 (2021), p. 165172. ISSN: 0168-9002. DOI: https://doi.org/10.1016/j.nima.2021.165172.

[103] James R Norris. *Markov chains*. 2. Cambridge university press, 1998.

[104] Nicholas Metropolis et al. "Equation of State Calculations by Fast Computing Machines". In: *The Journal of Chemical Physics* 21.6 (June 1953), pp. 1087–1092. ISSN: 0021-9606. DOI: 10.1063/1.1699114.

[105] W. K. Hastings. "Monte Carlo sampling methods using Markov chains and their applications". In: *Biometrika* 57.1 (Apr. 1970), pp. 97–109. ISSN: 0006-3444. DOI: 10.1093/biomet/57.1.97.

[106] Michael E. Tipping and Christopher M. Bishop. "Mixtures of Probabilistic Principal Component Analyzers". In: *Neural Computation* 11.2 (Feb. 1999), pp. 443–482. ISSN: 0899-7667. DOI: 10.1162/089976699300016728.

[107] Christopher KI Williams and Carl Edward Rasmussen. *Gaussian processes for machine learning*. Vol. 2. 3. MIT press Cambridge, MA, 2006.

[108] Ö. Sürer et al. "Uncertainty quantification in breakup reactions". In: *Phys. Rev. C* 106 (2 Aug. 2022), p. 024607. DOI: 10.1103/PhysRevC.106.024607.

[109] Matthew Plumlee et al. *surmise 0.4.0 Users Manual*. Tech. rep. Version 0.4.0. NAISE, 2025. URL: https://surmise.readthedocs.io.

[110] Kyle Beyer et al. *BANDFramework: An Open-Source Framework for Bayesian Analysis of Nuclear Dynamics*. Tech. rep. Version 0.3.0. 2023. URL: https://github.com/bandframework/bandframework.

[111] Chloe Fougeres. "Understanding the cosmic abundance of ^{22}Na : lifetime measurements in ^{23}Mg." PhD thesis. Narmandie Université, 2022.

[112] S Hinds and R Middleton. "The Energy Levels of 15O, 23Mg and 27Si". In: *Proceedings of the Physical Society* 73.5 (May 1959), p. 727. DOI: 10.1088/0370-1328/73/5/305.

[113] L.C. Haun, N.R. Roberson, and D.R. Tilley. "A study of the low-lying states of 23Mg". In: *Nuclear Physics A* 140.2 (1970), pp. 333–358. ISSN: 0375-9474. DOI: https://doi.org/10.1016/0375-9474(70)90330-1.

[114] R. EngMann, F. Brandolini, and I. Mauritzson. "Lifetime measurements in sd shell nuclei: (VI). Mean lives of 23Mg levels". In: *Nuclear Physics A* 171.2 (1971), pp. 418–424. ISSN: 0375-9474. DOI: https://doi.org/10.1016/0375-9474(71)90031-5.

[115] H. Nann, A. Saha, and B. H. Wildenthal. "Energy levels in ^{23}Mg from the ^{25}Mg$(p,t)^{23}$Mg reaction". In: *Phys. Rev. C* 23 (2 Feb. 1981), pp. 606–615. DOI: 10.1103/PhysRevC.23.606.

[116] DD Warner, MA Bentley, and P Van Isacker. "The role of isospin symmetry in collective nuclear structure". In: *Nature Physics* 2.5 (2006), pp. 311–318.